DICHALCOGEN SEMICONDUCTORS FOR OPTOELECTRONIC AND SPINTRONIC APPLICATIONS

Thesis by

Bhagyashri Devaru Bhat
Registration ID : 20163486

In partial fulfillment of the requirements
for the degree of
Doctor of Philosophy

Under the supervision of

Dr. Mukul Kabir
Department of Physics

Indian Institute of Science Education and Research
Pune, India

January 2023

CERTIFICATE

This is to certify that the work incorporated in the thesis entitled *"Dichalcogen semiconductors for optoelectronic and spintronic applications"* submitted by Bhagyashri Devaru Bhat was carried out by the candidate under my supervision. To the best of my knowledge, the work presented here or any part of it has not been included in any other thesis submitted previously for the award of any degree or diploma from any other university or institution.

Signature of Thesis Supervisor

Dr. Mukul Kabir

Associate Professor

Department of Physics

IISER Pune-411008

DECLARATION

I, *Bhagyashri Devaru Bhat*, declare that this Ph.D. thesis entitled *"Dichalcogen semiconductors for optoelectronic and spintronic applications"* represents my ideas in my own words and where others ideas have been included, I have adequately cited and referenced the original sources. I also declare that I have adhered to all principles of academic honesty and integrity and have not misrepresented or fabricated or falsified any idea/data/fact/source in my submission. I understand that violation of the above will be cause for disciplinary action by the institute and can also evoke penal action from the sources which have thus not been properly cited or from whom proper permission has not been taken when needed.

Bhagyashri Devaru Bhat

ID: 20163486

To my beloved grandmother

Smt. Vishalakshi Parameshvar Hegde

A constant inspiration to my life

ACKNOWLEDGEMENTS

This research work was successful due to the tremendous contribution of the scientists who built fundamental laws of physics and Density Functional Theory. The computational modeling of materials was only possible with their prior hard work. I sincerely express my gratitude to all of them. Numerous people have supported me scientifically and personally in fulfilling this work. Through this opportunity, I greatly appreciate their help.

Every student needs good guidance to conduct research. I have gained it from my supervisor Dr. Mukul Kabir. He provided me with enough freedom to work. He inspired me to conduct research independently. His precise way of writing research articles directed me toward scientific writing and helped me get research exposure. It is the most excellent support a student can get in their Ph.D. tenure. He taught me advanced condensed matter physics in my coursework, which was outstanding teaching. In a way, he empowered me to think independently about the research projects. I have got the publications due to the knowledge and innovative ideas gained by my supervisor. This thesis was impossible without my supervisor's support.

This thesis would not have been possible without the financial support of the DST INSPIRE fellowship. Thanks to our campus, the Indian Institute of Science Education and Research Pune, for providing the best environment to proceed with the research. I gratefully acknowledge the funding provided by the Department of Science and Technology, Government of India, under the Nano Mission project SR/NM/TP-13/2016. I also gratefully acknowledge the Centre for Development of Advanced Computing, Pune; Center for Computational Materials Science, Institute of Materials Research, Tohoku University, Japan; PARAM Brahma Facility at IISER Pune, under the National Supercomputing Mission of Government of In-

dia and S. N. Bose National Centre for Basic Sciences, Kolkata, for providing an enormous computational facility. I want to thank my thesis committee: Dr. Atikur Rahman and Dr. Bhalchandra Pujari, for their encouragement and valuable suggestions during the research advisory community meetings, which motivated me to have more exposure to research. My special thanks to Prof. Satishchandra Ogale for helpful discussions during the research work.

I thank my past and present labmates, Dr. Rohit Babar and Dr. Srilatha Arra, Dr. Tilak Das, Dr. Ramya, Chandan Kumar Singh, Anju Chandran, Deepak Kumar Roy, Dr. Amareen, Basavaraj G, Anupama, Ashutosh, and Dr. Ashish.

I would like to thank IISER staff, Mr. Tushar Kurulkar, Mr. Prabhakar Anagare, Mr's Dhanashree, Mr's Nisha Kurkure, and Mr's Saylee for helping with technical and academic issues. I thank every person at IISER, Pune.

With immense pleasure and love, I want to thank my husband and my best friend, Dr. Hariprasad M Hegde, for enhancing my research interest through his excellent support, encouragement, discussions, and motivation.

I could pursue research because of the inspiration from my teachers. So at this time, I would like to sincerely say thank you to all my teachers: Mr's Sharada, Mr. Manjunath M Ambig, Mr's Annapoorna, Mr's Mangalagowri Shet, Mr's Mangala, Mr. K. G. Bhat, Mr. G. N. Hegde, Mr's Srikala Bhat, Mr. M. G. Bhat, Mr. Pramod Basgode, Mr. Ramesh, Mr. Hunasikatti, Mr. Rajesh, and Mr's Divyajyothi Shetty. I sincerely thank my professors, Prof. K. B. Vijaykumar and Prof. Gopalakrishna K Naik, for directing me toward research.

My most enormous thanks to my grandparents Sri Parameshvar Hegde, Smt. Vishalakshi Parameshvar Hegde, Sri Ganesh Bhat, and Smt Parvati Ganesh Bhat, who instilled confidence in me and made me enjoy life right from my childhood; without their blessings, my effort was not successful. Their blessings are my strength. I sincerely thank my parents and in-laws: Mr. Devaru Bhat, Mr's Ganga Bhat, Mr.

Manjunath Hegde, and Mr's Malathi Hegde, for their continuous support and inspiration throughout my journey. I am thankful to Mr. Manjunath Shivram Hegde and his family for their support during the COVID-19 pandemic. Also, I am grateful to my second parents, Mr. Ramachandra V Hegde and Mr's Nagarathna R Hegde, for their tremendous support and excellent research atmosphere. I thank my beloved brothers and sisters: Mr. Shriganesh Bhat, Mr's Rashmi Thriguna, Mr. Thriguna Mutuguppe, Mr. Shriprasad Hegde, and Mr. Gaurish Hegde, for their motivation. I thank all my friends: Manasa Hegde, Meghana Shivanna, Krithika, Dibyata, Anjusha, Hridya, Ajith, Shathruhan, Vijaya, and Shridhar Hegde for making me happy with fun, enjoyable, and fruitful discussions. I would like to thank my wellwishers, Mr's Shanti R Hegde, Mr. Shridhar Bhat, and Mr. Vinayaka Bhat, for their moral support and help.

SYNOPSIS

Semiconductors are the building blocks of electronic, optoelectronic, and spintronic technologies. Irrespective of unique electronic and optical attributes, the zero band gap of graphene stimulated the search for layered materials with semiconducting characteristics. Layered metal dichalcogenides have gained immense interest in this regard due to the sizeable band gap and their easy tunability. Tin disulfide (SnS_2) is a layered metal dichalcogenide semiconductor that exhibits a wide electronic band gap.

Here we investigate the transition metal doped SnS_2 and its optoelectronic properties. However, predicting a true band gap accurately with theoretical methods is a complex problem. In this contemplation, we use dielectric-dependent hybrid functionals (DDHF), and band gaps are calculated self-consistently. Self-consistent DDHF provides the range of band gap values within which the experimental band gap is expected. In a way, it predicts the upper and lower bound for the actual value of the band gap. Further, we discuss the optical properties of all the doped systems. Absorption spectra, optical constants, and exciton binding energies are well studied in this part. The absorption spectra reveal the enhanced absorption and red shift in the energy of all the doped systems. Here we discovered the direct band gap semiconductors with small exciton binding energies. These findings confide that the transition metal-doped SnS_2 systems are viable candidates for optoelectronic applications.

Next, we discuss the magnetic properties of the doped systems. Here we discuss the origin of magnetic moment and magnetic interaction between the two magnetic impurities with electronic properties. Ferromagnetic metals, half-metals, and ferromagnetic semiconductors investigated in this study are suitable candidates for spin injection, the spin-polarized current generation, and other spintronic

applications.

Due to the unvanished polarity between the two unidentical chalcogen atoms, Janus metal dichalcogenide monolayers are expected to exhibit the Rashba effect. In this context, we study the Rashba spin splitting in Janus SnXY and WXY (X, Y = S, Se, Te with X $\neq$ Y) monolayers along with their vertical heterostructures. The SnSSe/WSSe semiconducting heterostructure exhibits room temperature Rashba spin-splitting energy of about 43 meV and shows enhancement in the Rashba parameter up to 1 eVÅ with the vertical compressive strain. These results indicate that the heterostructure is productive for spintronic applications.

TABLE OF CONTENTS

Acknowledgments ii

Synopsis v

Chapter 1: Introduction 9

1.1 Layered Metal Dichalcogenides 9

1.2 Tin Disulfide (SnS_2): A wide band gap semiconductor 11

1.2.1 Optoelectronic applications 16

1.2.2 Spintronic applications 17

1.3 Rashba effect in 2D materials 18

Chapter 2: Computational Methods 21

2.1 Many-body problem 21

2.1.1 Born-Oppenheimer approximation 22

2.1.2 Hartree and Hartree-Fock Approximations 23

2.2 Density Functional Theory 25

2.2.1 Exchange-correlation energy 28

2.2.2 Local Density Approximation (LDA) 29

2.2.3 Generalized gradient approximation (GGA) 29

2.2.4 Hybrid Functionals 30

2.3 Dielectric-dependent hybrid functionals 31

Chapter 3: Electronic and optical properties of 3d transition metal-doped SnS_2 33

3.1 Introduction 34

3.2 Computational Details 40

3.3 Results and Discussion 42

3.3.1 Structural stability 42

3.3.2 Dielectric response of a proper 2D-material 44

3.3.3 Electronic properties 47

3.3.4 Importance of DDHF calculation 50

3.3.5 DDHF calculations on bulk and monolayer doped systems . . 54

3.4 Optical properties 63

3.4.1 Exciton binding energy 67

3.5 Conclusion 75

Chapter 4: Tuning the magnetic properties of monolayer SnS_2 by 3*d* transition metal doping 77

4.1 Introduction 78

4.2 Computational Details 80

4.3 Results and discussion 81

4.3.1 Formation energy of single TM doped ML-SnS_2 81

4.3.2 Binding energy of double TM doped ML-SnS_2 83

4.3.3 Electronic property 84

4.3.4 Magnetism in single TM atom doped ML-SnS_2 87

4.3.5 Magnetism in double TM atom doped ML-SnS_2 93

4.4 Conclusion 98

Chapter 5: Rashba spin-splitting in Janus SnXY/WXY (X, Y = S, Se, Te with X $\neq$ Y) heterostructures 101

5.1 Introduction 102

5.2 Computational Details 106

5.3 Results and discussion 107

5.3.1 Janus-SnXY and WXY monolayers 107

5.3.2 Rashba spin splitting in J-SnXY and J-WXY monolayers 108

5.3.3 Spin splitting in SnXY/WXY heterostructures 114

5.3.4 Effect of vertical strain on SnSSe/WSSe HS 124

5.4 Conclusion 127

Chapter 6: Summary and future outlook 129

Bibliography 132

List of Publications 174

CHAPTER 1

INTRODUCTION

1.1 Layered Metal Dichalcogenides

The research of two-dimensional (2D) materials has obtained particular interest after the discovery of single-layer graphene [1]. The unique electronic properties of graphene are contributed by the linear dispersion at K-point in its band structure. Additionally, this results in novel phenomena like the anomalous room-temperature quantum Hall effect [2]. Graphene is a superb thermal conductor and an excellent electronic conductor. There are numerous applications for graphene-based materials, including high-speed electronics devices such as a flexible graphene terahertz detector [3, 4], optical devices such as optical sensors [5, 6], solar cells [7, 8], modulators [9], high-speed optical switch [10] and photonic devices [11]. Graphene-based energy storage devices such as batteries [12, 13] and supercapacitors [14] are fabricated. Graphene-based systems are useful for hydrogen evolution reaction [15] and visible light photocatalysis [16]. Apart from this, it also has applications in the field of spintronics. It is a good material for spin channels due to the flexible spin injection and transport at room temperature on the graphene surface, which enhances the spin lifetime [17, 18]. Despite all these interesting properties, the zero band gap nature of graphene makes explosive interest to think about other layered materials with a finite band gap. Layered metal dichalcogenides (LMDs) have gotten greater attention due to their fascinating electrical and optical properties.

LMDs are indicated by a chemical formula MX_2, where M is the metal atom,

M = Mo, W, Hf, Nb, Sn, and so on, and X is the chalcogen atom X = S, Se, Te. LMDs naturally exist in the bulk form with atomically thin layers stacked by Van der Waals interaction. The individual layers can be extracted with the extremely small thickness possible for nanoscale research. The sizeable band gap spans their applications related to the electronic structure in place of graphene. This made them considerably necessary in 2D materials research and significantly attracted the design of novel electronic and optoelectronic devices. As graphene shows novel properties in the nanoscale rather than in the bulk counterpart, LMDs can also access the unique physics when they are thinned down to the atomic scale. This is the most outstanding contribution of LMDs to 2D materials research.

MoS_2 [19] is the first layered material studied extensively after the graphene discovery. It is one of the transition metal dichalcogenides (TMDs). Out of sixty TMDs, forty are of layered nature. These layered TMDs exhibit strong covalent intralayer bonding between the metal and chalcogen atoms. Each individual layer is weekly interacted by the Van der Waals force. The detailed structure of MoS_2 was first determined by Linus Pauling in 1923 [20]. Among the two common structural phases 1T (octahedral) and 2H (trigonal prismatic), 2H is the thermodynamically stable phase for all the TMDs except WTe_2, which exhibits an orthorhombic phase. In the 2H phase, M-atom is sandwiched between two chalcogen atoms. TMDs such as MoS_2, WS_2, $MoSe_2$, and WSe_2 [21, 19] turn into direct band gap semiconductors when they are transformed from bulk to monolayer environment. The band gap lies in the visible light region in all the TMDs from bulk to monolayer limit. This is the remarkable electronic property of TMDs over graphene. The direct electronic transition leads the TMDs to use in various optoelectronic devices. When a bulk MoS_2 is thinned down to a monolayer, its band gap increases from 1.3 to 1.8 eV [19] and turns into a direct band gap semiconductor. The possibility of band gap tuning with the number of layers makes TMDs a perfect candidate

for device applications. Based on these properties 2D-TMDs are utilised in many electronic and nanoelectronic devices [22, 23] such as Esaki diodes [24], resonant tunneling diodes(RTDs) [25], logic and RF transistors [26, 27, 28], tunneling field-effect transistors (TFETs) [29, 30, 31, 32], bipolar junction transistors [33, 34], static random access memories (SRAMs) [35], dynamic RAM (DRAMs) [36], flash memory [37, 38] and ferroelectric memories [39, 40] etc. TMDs-based optoelectronic and photonic devices [41] are photodetectors [42, 43], photovoltaic cells [44, 45] and light-emitting devices [46] etc.

Most of the layered TMDs are non-magnetic semiconductors. Many attempts have been done to induce magnetism using disorder[47], vacancies [48], strain [49, 50, 51], non-metal absorbates [52, 53] and doping magnetic impurities [54, 47]. The loss of inversion symmetry in monolayer TMDs results in the spin splitting of energy bands, and a maximum spin splitting energy of 456 meV is calculated in WSe_2 monolayer at valence band maxima at K-point [55]. On top of this, the lack of inversion symmetry with spin-orbit coupling causes coupled spin and valley physics in monolayer MoS_2 and other group-4 dichalcogenides [56]. Consequently, in both electron and hole-doped TMDs, the valley and spin Hall effects coexist; hence, the charge carriers will have longer spin and valley lifetime. This is because the spin and valley-dependent optical selection rules restrict the easy recombination of photoinduced charge carriers in spin-split bands. These outcomes indicate the potential for applications that blend spintronic and valleytronic technologies.

1.2 Tin Disulfide (SnS_2): A wide band gap semiconductor

Tin disulfide (SnS_2) is a member of the LMDs family. Various polytypes of SnS_2 crystal are studied using a variation of conductivity with temperature [57]. The

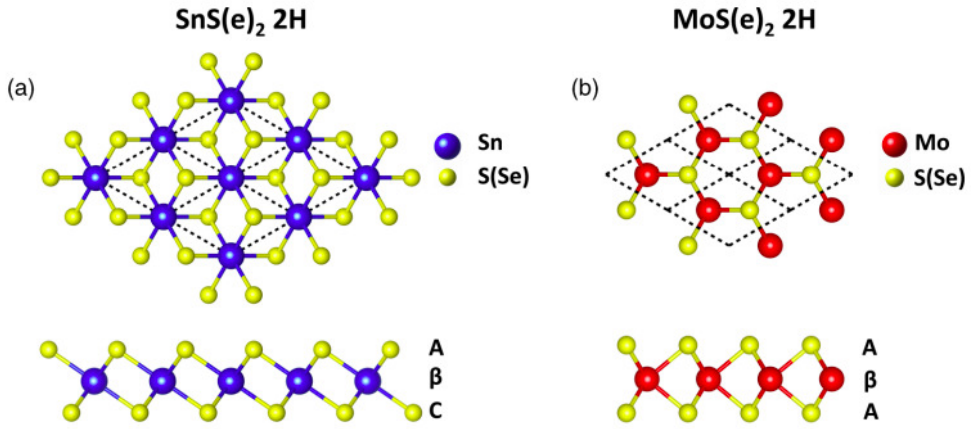

Figure 1.1: Crystal structure for a monolayer of (a) SnS_2 ($SnSe_2$) and (b) MoS_2 ($MoSe_2$), taken showing the different metal and chalcogen coordination in both the crystals. Figure reprinted from [59] is taken from the permission of APS.

stable form of the crystal is found in 2H-polytype [58, 59]. The confusion regarding the nomenclature of the crystal phases of the TMDs and SnS_2 are clearly removed by Figure 1.1 Unlike the TMDs, it belongs to the $P\bar{3}m1$ space group with octahedral coordination of the Sn atom surrounded by six S atoms. It is a wide band gap semiconductor with a band gap of 2.2-2.43 eV from bulk to monolayer limit. The chemical stability of SnS_2 crystal makes it a nontoxic, nonflammable, and affordable material that can resist water and air. The layered structure of SnS_2 allows one to synthesize it in a single layer. Several experimental techniques have been devised to manufacture SnS_2 nanostructures of various sizes (from 10 to 100 nm) and morphologies such as nanoparticles, nanorods, nanobelts, nanotubes, and nanosheets [60, 61, 62, 63, 64, 65, 66]. For extensive commercial applications, bulk and nanoform SnS_2 have significant advantages due to the abundance of both Sn and S on Earth and the environmentally genial, low-cost production technique. All these advantages attracted the crystal to study extensively by researchers. The electronic and optical properties of SnS_2 crystal are well studied to date. Due to its indirect band gap behavior, it is restricted to applications in light harvesting or

detecting devices. Hence numerous efforts are made to convert the bulk crystal into a direct band gap semiconductor. It is predicted that applying biaxial tensile strain of 2.98% bulk SnS_2 undergoes indirect-to-direct band-gap transition [67] and results in a quasiparticle direct band gap of 2.17 eV. A biaxial tensile strain of 9.75% causes semiconductor-to-metal transition. The transition is caused by the strain-induced weakening of the interaction of the in-plane orbitals, which changes the dispersion and characteristics of the valence and conduction band edges. To study the effect of band gap with the number of layers, layer dependence of the SnS_2 crystal is well researched. In this approach, electronic and optical properties are well explained by considering the monolayer to few-layer to bulk crystal. The screening of electrostatic interactions effectively reduces in a few-layer system surrounded by vacuum [68, 69, 70] also the quantum confinement effect [21] plays a vital role in monolayer systems. The combined effect causes an increase in the band gap of monolayer semiconductors than in their bulk counterpart, as revealed in TMDs [71] and phosphorene [72, 73]. A slight increase (2.2 to 2.43 eV) in the band gap from bulk to monolayer limit shows that the SnS_2 crystal is insensitive to the number of layers. In contrast to TMDs monolayers, it remains an indirect band gap semiconductor in a monolayer environment.

Excitons are the bound form of electrons and holes. Exciton physics is crucial for understanding the importance of a system's optical properties. In this regard, the layer-dependent study of excitons in SnS_2 crystal is very well explained by Ivan I. Oleynik and Joseph M. Gonzalez [59]. The bulk system is thoroughly surrounded by a dielectric medium from all three directions; hence the Coulomb interaction between electron and hole is well screened by the dielectric medium. In the case of a 2D-system, the screening effect is reduced and confined only to the 2D-plane. On top of this, quantum confinement also adds to dielectric confinement. Finally, these two confinement effects make the excitons tightly bound on a 2D-plane rather than

in the bulk environment of the system. This fact leads to higher binding energy in monolayer systems. The layer-dependent study reveals that strong excitonic effects are observed as the number of layers decreases in the stack of the bulk crystal. The 2D exciton binding energy of 0.912 eV is substantially decreased to 0.137 eV for the 3D-SnS_2 [59].

As a layered semiconductor, 2D-SnS_2 sheets provide a large surface area for solar energy absorption and active sites for chemical reactions. Due to the cheap and clean elemental components monolayer SnS_2 is an excellent semiconducting material in photocatalytic water-splitting reactions. Aron Walsh *et al.* [74] demonstrated that a single crystal of SnS_2 is an earth-abundant disulfide photocatalyst.

Carbon anodes cannot supply the large capacity batteries that will be required in the future(with a theoretical capacity of 372 $mAhg^{-1}$) [75]. Considering their transformation into lithium-metal alloys, different metal composites, metal oxides, and metal sulfides have recently undergone substantial research as potential substitutes for carbonaceous anode materials due to their greater capabilities [76, 77, 78, 79, 80]. In this regard, SnS_2 nanosheets are a suitable replacement for the anode material in Li-ion batteries [81]. With an average discharge capacity of 583 $mAhg^{-1}$ which is 90% of the maximum theoretical reversible value and 1.6 times higher than that of a commercialized carbon electrode [82], the 2D-SnS_2 nanoplates are excellent alternative electrode materials for Li-ion batteries. According to room temperature gas sensing measurements, the 3D-SnS_2 nanostructures are capable of NH_3 molecule sensors [83].

A good optoelectronic device needs a direct band gap semiconductor, with small exciton binding energy and high carrier mobility. A direct band gap material absorbs/emits sun light efficiently. A small exciton binding energy of carriers helps in the easy separation of electron and hole. With high carrier mobility the carriers move fast and takes less time to travel the device. The higher carrier mo-

bility increases the operation speed of the device. In this context many attempts are made to though SnS_2 is an indirect band gap semiconductor,

The SnS_2 nanosheets synthesized with a simple biomolecule-assisted method have proven to be ideal candidates for photoelectric applications, such as those found in Li-ion batteries, and exhibit photocatalytic, field emission, and photoconductive capabilities [84]. The study showed the rapid response of SnS_2 device to UV light and exceptional photosensitivity and stability. Further investigations into the field emission characteristics of SnS_2 nanosheets revealed a turn-on field of 6.9 $V/\mu m$, which is lower than previously reported values [84]. Thus based on the field emitters made by SnS_2 nanosheets, one can assure that it is a promising material for future optoelectronic applications. In addition to this, electronic devices such as field effect transistors implemented by using exfoliated nano-membranes of a layered 2D-SnS_2 semiconductors showed high on/off ratio exceeding 2×10^6 and carrier mobility of 1 $cm^2V^{-1}s^{-1}$ [85]. The improved electronic and photoelectric characteristics were expected from graphene-like structures. The findings show that SnS_2, a layered semiconductor with a finite band gap, has enormous potential as the foundation for upcoming photoelectric and nanoelectronic applications that complement graphene-based materials with zero or narrow band gaps. High-performance top-gated field-effect transistors and related logic gates are fabricated using monolayer SnS_2 with carrier mobility of 50 $cm^2V^{-1}s^{-1}$ which is higher than the back-gated value 1 $cm^2V^{-1}s^{-1}$ [86]. In addition, the wide band gap SnS_2 shows n-type electrical conductivity with a maximum dark value of 1.3×10^{-2} cm^{-1} and activation energy of 0.14 eV. As a result, an entire solar cell was created using SnS_2 crystal. These findings show that SnS_2 has a broad area of applications in the field of (Opto) electronics, nanoelectronic, energy storage, and photocatalysis. Apart from this, the 2D-SnS_2 based tunneling transistors with 2D-WS_2 are fabricated [87], which exhibits superior on-state current and steeper

subthreshold slope than conventional FET. It shows the highest on-off ratio over 106 among the value of 2D-2D tunneling transistors.

Motivated by the exciting electronic and magnetic properties induced in TMDs by transition metal doping [54, 47], in this work, bulk and monolayer SnS_2 crystals are doped by 3*d* series transition metal atoms. Band gap is a crucial metric for deciding the potential applications of a semiconductor. Accurately measuring the true band gap of a semiconducting system is an enormous challenge for theoretical methods. Theoretical predictions need to match the experimental values better. In this regard, Chapter 3 discusses the dielectric-dependent hybrid functionals calculations and applies them to all the bulk and monolayer doped systems. This computation provides the upper and lower bound for a system's true band gap within which the experimental gap is expected.

1.2.1 Optoelectronic applications

A suitable optoelectronic device needs a direct band gap semiconductor with small exciton binding energy and high carrier mobility. A direct band gap material absorbs/emits sunlight efficiently (high absoprtion coefficient). The small exciton binding energy of carriers helps to easily separate electrons and holes. With high carrier mobility, the carriers move fast and take less time to travel the device. The high carrier mobility increases the operation speed of the device. These characteristics are essential for the efficient generation of photocurrent in the device. In this context, many attempts are made for the indirect-to-direct band gap transition in SnS_2 as explained previously using strain engineering. This study carried the transition metal doping on SnS_2, and we observed indirect-direct-band gap transition with small exciton binding energy in bulk-doped systems. This chapter also explains the optical properties of all the doped systems in bulk and monolayer environments. Finally, we conclude that the transition metal doped SnS_2 systems are

viable candidates for electronic and optoelectronic devices.

1.2.2 Spintronic applications

Spintronic devices use spin-polarized current instead of charge current in electronic devices. Hence it is essential to get the spin currents in semiconducting materials. Due to low power consumption, less heat dissipation, massive data storage, high-speed operation, and non-volatile magnetic storage, spintronic technology gains superiority over electronic technology. As the electron's spin participates in transport, a suitable channel that supports and smoothens the spin transport is essential. Along with this, it is also necessary that the spins should have a long lifetime for long-lived current production, and more extended spin propagation is required for spins to transport long distances. Achieving all these requirements in a single material is a challenge in the spintronic field. With these transport requirements, obtaining spin and generating one-spin orientation is difficult. A ferromagnetic material is a suitable candidate to produce one-spin polarization, but having Curie temperature in the room temperature range and controlling the T_c is another trouble in getting the spin-polarized current. Substitutional doping by magnetic species excites studying the formation of magnetic moment and possible magnetic interactions, which leads to determining the spintronic and related applications. Though the SnS_2 crystal is well studied in optoelectronic fields, further studies are required in the perspectives of spintronic applications. In Chapter 4, we discuss the transition metal doping on monolayer SnS_2 crystal. Here we study the origin of magnetic moment formation and the interaction between the two magnetic species. We will eventually understand the importance of transition metal doped SnS_2 for potential applications in the spintronic field.

1.3 Rashba effect in 2D materials

The generation of spin-polarized current in a non-magnetic material is possible when the degenerate spin states are well separated. The spin splitting within the same band in a dispersion relation is possible by lifting the spin degeneracy. The electric field and magnetic field applications can lift the spin degeneracy in some semiconducting materials. Symmetry breaking induces new physics in condensed matter systems. As we have seen in TMD monolayers, the lack of in-plane symmetry and the existence of spin-orbit coupling together generates Zeeman-type of spin and valley coupling physics [56]. Further, with the strong spin-orbit coupling and in-plane inversion symmetry breaking, what happens to the system if the out-of-plane mirror symmetry is also broken? This leads to a new kind of spin splitting, which is entirely momentum-dependent. The out-of-plane symmetry breaking leads to a potential gradient and creates an internal electric field ($\vec{E}_{int}$) along the out-of-plane direction. The moving electron in a 2D-plane then experiences a crossed effective magnetic field perpendicular to both electron momentum and electric field. This magnetic field quantizes the spins, and the spins orient according to momentum as the effective magnetic field directs according to the electron's momentum. Hence the spin splitting caused by the electric field takes place along the in-plane momentum direction in the energy dispersion relation. This type of spin splitting is known as Rashba spin splitting [88], and it is expected in monolayers, surfaces, and interfaces that exhibit a loss of inversion symmetry perpendicular to the 2D-plane.

Rashba spin splitting is not observed in 2D-TMDs due to out-of-plane mirror symmetry. As a result, tremendous attempts such as making Van der Waals heterostructures with TMDs, combining MOS_2 with graphene [89], bismuth (111) [90], and ferromagnetic CoFeB [91], also electric field is applied to break the vertical

mirror symmetry [92, 93, 94]. Due to the polar nature, the trimerized MoS_2 have shown the Rashba effect [95]. In 2017 ternary MoSSe (Janus MoSSe) layers are synthesised [96]. In the MoS_2 monolayer, out of two S atom layers, one of the layers is entirely replaced by Se atoms. Now the two different electronegative atoms cause nonzero net polarity, which induces an internal electric field perpendicular to the 2D-plane. The breaking of out-of-plane mirror symmetry in the polar MoSSe monolayer produces Rashba spin splitting. The Rashba Hamiltonian is given by [88]

$$H_R = \alpha_R |\vec{E}_{int}| (\vec{\sigma} \times \vec{k}).\hat{z} \tag{1.1}$$

Here α_R is the Rashba parameter, $\vec{\sigma}$ is the spin polarization vector, $\vec{E}_{int}$ is the internal electric field, and $\hat{z}$ is the unit vector perpendicular to 2D-plane. The corresponding band dispersion relation for the spin split bands is given by

$$E \pm (k) = \frac{\hbar^2}{2m^*} \pm \alpha_R |\Delta k| \tag{1.2}$$

Where m^* is the effective mass of the electron. The E_+k and E_-k represent energy eigenstates for the opposite in-plane spin polarization. The energy bands with eigenstates E_+k and E_-k are perpendicular to the $\vec{k}$ direction and are shifted by Δk. By keeping the one parabolic band fixed, the other band will either shift by $+\Delta k$ or by $-\Delta k$. Here α_R dictates the strength of Rashba spin splitting. This is given by

$$\alpha_R = \frac{2 * E_R}{k_R} \tag{1.3}$$

Where E_R is the spin splitting energy, and k_R is the wavenumber difference in the spin split bands. The Rashba spin splitting in Janus-TMD systems with M = Mo, W are well studied[97], a highest α_R of 524 meVÅ is calculated in Janus WSeTe monolayer. A few layer Bi_2Se_3/2L $PtSe_2$ heterostructure shows a giant Rashba splitting energy of 275-278 meV and α_R = 16.66 to 16.84 eVÅ [98], which is the highest value

reported till date. The $MoTe_2/PtS_2$ heterostructure has a room temperature spin splitting energy ($\geq$ 25 meV) E_R = 94 meV, enough momentum shift k_R = 0.182 $Å^{-1}$ to get a short device channel length of about 0.87 nm and α_R = 1.03 eVÅ [99]. As well as, the band dispersion has only Rashba bands at the Fermi level. This heterostructure meets all the requirements to be a good Rashba material. Monolayer tin dichalcogenides such as SnS_2, $SnSe_2$, and $SnTe_2$ don't show the Rashba effect due to the presence of out-of-plane mirror symmetry. Hence one needs to study them by replacing one of the chalcogen atoms with a different one. Chapter 5 discusses the Rashba effect in Janus SnXY and WXY (X, Y = S, Se, Te with X $\neq$ Y) monolayers and their heterostructures. In addition, the chapter also explains the effect of vertical strain on the Rashba spin splitting energy and Rashba parameter in SnSSe/WSSe heterostructure.

CHAPTER 2

COMPUTATIONAL METHODS

This chapter explains the computational methods used to study the properties of bulk and monolayer crystals using density functional theory (DFT). The fundamental ideas that underpin the DFT computations are presented in this chapter. It begins with the difficulties in solving the quantum mechanical many-body problem. Every crystal is subjected to relaxation using several DFT approximations to get its minimal energy state. Material's electronic properties significantly impact the applications of electrical, optoelectronic, and spintronic devices. Thus computationally expensive but accurate hybrid DFT functionals are used to study the electronic properties. The band gap dependency on the dielectric constant is studied very well. Spin-polarized calculations describe spin splitting in the electronic band structure.

2.1 Many-body problem

A condensed matter system has positively charged nuclei and negatively charged electrons. Thus the system involves various interactions, namely ion-ion, electron-electron, and electron-ion interactions. Hydrogen molecule, including all these interactions, can be solved exactly using the Schrödinger equation. A condensed matter system's total number of electrons becomes wN when it contains N atoms and w electrons. This system is now referred to as a many-body system. One can

exactly set up the many-body Hamiltonian as

$$\mathscr{H} = -\sum_I \frac{\hbar^2}{2M_I}\nabla_I^2 + \sum_i \frac{\hbar^2}{2m_i}\nabla_i^2 + \frac{1}{2}\sum_{I\neq J}\frac{Z_I Z_J e^2}{|R_I - R_J|} + \frac{1}{2}\sum_{i\neq j}\frac{e^2}{|r_i - r_j|} - \sum_{i,I}\frac{e^2 Z_I}{|R_I - r_i|} \tag{2.1}$$

where $I(i)$ represents an ion (electron), $M(m)$ is the ion (electron) mass, $R(r)$ is the position of ion (electron). The Hamiltonian containing the terms ∇_I^2 and ∇_i^2 represent the kinetic energy of ions and electrons, respectively. The ion-ion and electron-electron Coulomb interaction energy are represented by the third and fourth terms of the Hamiltonian. The last term in the expression represents the electron-ion interaction. The solution is given by the Schrödinger equation

$$\mathscr{H}\Psi(r_i, R_I) = E\Psi(r_i, R_I), \tag{2.2}$$

where Ψ is the many-body wave function, and E is the eigenvalue of the system. Except for systems like Hydrogen molecule, it is nearly hard to obtain the analytical solution for this many-body wavefunction. Hence approximation methods are applied for the possible interactions in the above Hamiltonian.

2.1.1 Born-Oppenheimer approximation

It is known that the ion is heavier than the electron. Its mass is 10^3 to 10^5 times greater than that of electron mass ($M_I \gg m_i$). Due to heavy mass, the characteristic time (τ) scale associated with ions is much larger than that of the electrons ($\tau_I \gg \tau_i$). Thus, the ions remain unchanged in the short period T, during which electrons change states. Hence one can separate the motion of the electrons from the motion of the ions. Therefore the total wavefunction in equation can be divided into ionic

and electronic wavefunctions.

$$\Psi(r_i, R_I) = \psi(R_I)\Phi(r_i)$$

where $\Phi(r_i)$ and $\psi(R_I)$ are the electronic and ionic wavefunctions respectively. This is called as Born-Oppenheimer or Adiabatic approximation [100, 101]. This indicates that the moving electrons feel the static potential produced by the static ions. The Schrödinger equation for the electronic part is given by

$$\left[\sum_i \frac{\hbar^2}{2m_i}\nabla_i^2 + \frac{1}{2}\sum_{i\neq j}\frac{e^2}{|r_i - r_j|} - \sum_{i,I}\frac{e^2 Z_I}{|R_I - r_i|}\right]\Phi(r_i) = E(r_i)\Phi(r_i) \tag{2.3}$$

where $E(r_i)$ represents the electronic eigenvalue. The electronic part calculates the electronic structure of the system. Then the effective Hamiltonian is expressed as

$$\mathscr{H} = \sum_i \frac{\hbar^2}{2m_i}\nabla_i^2 + \frac{1}{2}\sum_{i\neq j}\frac{e^2}{|r_i - r_j|} - \sum_{i,I}\frac{e^2 Z_I}{|R_I - r_i|} + V_{\text{ion}} \tag{2.4}$$

Due to the many-body electron-electron interactions, this Hamiltonian has to be simplified further using mean-field theory.

2.1.2 Hartree and Hartree-Fock Approximations

One needs to solve the electron-electron interaction part to simplify the electronic part of the many-body Hamiltonian. A many-body system of N atoms will have 3N variables when it couples with the coordinates of all N atoms in the system. Now it is impossible to solve the electron-electron interactions for 3N variables in the electronic part of the many-body Hamiltonian. To simplify the electronic part, several approximation methods have arisen. Hartree suggested that the many-body electronic wave function $\Phi(r_i)$ is the product of single electronic wave func-

tions [102].

$$\Phi(r_1, r_2, ...r_i, r_j.....r_{N-1}, r_N) = \phi_1(r_1)\phi_2(r_2)....\phi_i(r_i)\phi_j(r_j).....\phi_{N-1}(r_{N-1})\phi_N(r_N) \tag{2.5}$$

Each $\phi_i(r_i)$ is orthonormal and satisfies the one-electron Schrödinger equation. It indicates that each electron moves independently of the other. Electron only feels the average electrostatic potential created by the ions and all other electrons. This potential is termed as Hartree potential. Now substitute Eq. 2.5 into the electronic part of the Schrödinger equation $\mathscr{H}\Phi = E\Phi$

$$\left[-\frac{\hbar^2}{2m}\nabla_i^2 + V_{ion}(r_i) + e^2\sum_{j(\neq i)}\int\frac{|\phi_j(r')|^2}{|r-r'|}dr'\right]\phi_i(r) = E_i\varphi_i(r), \tag{2.6}$$

This single particle Schrödinger equation is called as Hartree equation. By applying the variational principle, the total energy is given by

$$E = \sum_i E_i - \frac{e^2}{2}\int\int\frac{\rho_i(r)\rho_j(r')}{|r-r'|}drdr'. \tag{2.7}$$

Here the second term is known as the Hartree energy, and $\rho(r) = |\phi(r)|^2$ represents the electron density. Though one can get the best fit for the electronic wave function, the Hartree approach lacks information that significantly affects the properties of the many-body system. It doesn't consider Pauli's exclusion principle; it only considers symmetric wavefunctions Eq. 2.5 that holds only for bosons. In other words, it totally neglects the Fermi-Dirac statistics. As the approach assumes that the electrons are moving independently in the average potential of all other electrons and ions, it doesn't take the exchange and correlation effects.

Electrons are indistinguishable and obey Pauli's exclusion principle. These two natures together make their wavefunction antisymmetric, which is not included in the Hartree approach. To overcome the inconsistency caused by the Hartree ap-

proach, Hartree and Vladimir Fock together address the antisymmetric wavefunction,

$$\Phi(r_1, r_2, ...r_i, r_j.....r_{N-1}, r_N) = -\Phi(r_1, r_2, ...r_j, r_i.....r_{N-1}, r_N) \tag{2.8}$$

Hartree-Fock's approach uses the Slater determinant [103] to express the antisymmetric wavefunction $\Phi(r)$ for electrons. Now the two anti-parallel electrons will have the exchange interaction that reduces the electron-electron repulsion. Hence the Coulomb energy of the entire system reduces. This energy gain is known as exchange energy. The Schrödinger equation corresponding to the Hartree-Fock approximation is given by [104]

$$\begin{aligned}\left[-\frac{\hbar^2}{2m}\nabla_i^2 + V(r) + e^2\sum_j \int \frac{|\phi_j(r')|^2}{|r-r'|}dr'\right]\phi_i(r) \quad &- \quad e^2\sum_j \int \frac{\phi_j^*(r')\phi_i(r')}{|r-r'|}dr'\phi_j(r) \\ &= \quad E_i\phi_i(r)\end{aligned} \tag{2.9}$$

Except for the exchange interaction term $e^2\sum_j \int \frac{\phi_j^*(r')\phi_i(r')}{|r-r'|}dr'\phi_j(r)$ which includes Pauli's exclusion principle, the other terms are precisely same as the Hartree equation Eq 2.6. Like-spin electrons are avoided by the exchange interaction, creating an exchange hole all around them. Despite adhering to the conventional single-electron understanding of the electronic structure, the Hartree-Fock approximation ignores electron correlation and assumes a single determinant form for the wave function. As a result, it underestimates the bond strengths and overestimates the band gaps. Hartree-Fock's theory needs to be revised to make precise quantitative predictions.

2.2 Density Functional Theory

Density-functional theory (DFT) is a quantum mechanical computational modeling method used to investigate the ground state properties of many-body sys-

tems. Here the word functional refers to the function of electron density which is a function of spatial coordinates. In DFT, all the properties are studied using the functional of electron density. Theoretically, Walter Kohn and Pierre Hohenberg first established density functional theory (DFT) within the context of the two Hohenberg-Kohn theorems. But it was initially involved in the Thomas-Fermi model [105, 106] for the electrical structure of materials. Even though the Hartree-Fock approach using the Slater determinant method provides a single-particle picture, the Slater determinant method of solving many-body electronic wavefunction needs vast computational costs. Again it was impossible to apply for 3N variables. In this sense, Thomas-Fermi (TF) theory provided a very rudimentary idea regarding the electron density. [105, 106]. Although it helped to define atoms' total energies, it did not result in chemical bonding. The intriguing aspect of the TF theory is that it established an implied one-to-one relationship between the density distribution $\rho(r)$ and interacting electrons traveling in an external potential $V(r)$.

$$\frac{1}{2}(3\pi^2)^{2/3}\rho(r)^{2/3} + V(r) + \int \frac{\rho(r')}{|r-r'|}dr' - \mu = 0, \tag{2.10}$$

, where μ is the chemical potential. Only systems with slowly fluctuating densities are most suited for the TF theory's use, which entirely disregards gradients of the effective potential.

The density $\rho(r)$ is referred to as the fundamental variable in the Hohenberg-Kohn theorem. This theorem states that the ground-state density $\rho(r)$ of a bound system of interacting electrons in an external potential $V(r)$ determines this potential uniquely. The term uniquely means here: up to an uninteresting additive constant. The lemma refers to any ground-state density $\rho(r)$ for a degenerate ground state. The theorem concluded that $\rho(r)$ implicitly defines all attributes that can be derived from Hamiltonians by solving the Schrödinger equation. As a result, the

ground state electronic density contains all the information necessary to understand the system's physical observables. In other words, the electronic properties are a functional of the electron density. However, the theorem does not explain how to get the ground-state energy from the ground-state electron density without first determining the wave function.

Kohn-Sham theory introduces a noninteracting kinetic energy functional T_s into the energy expression. KS theory introduces a term $\Delta T[n]$ defining the difference between the kinetic energy of real and reference system of noninteracting electrons with a density equal to the density of the real system.

$$\Delta T[\rho] = T[\rho] - T_s[\rho] \tag{2.11}$$

In other words, it maps the interacting many-body system onto a noninteracting system of the same electron density. Similarly by defining

$$\Delta U[\rho] = U[\rho] - \frac{1}{2}\int\int \frac{\rho(r_1)\rho(r_2)}{|r_1 - r_2|} dr_1 dr_2) \tag{2.12}$$

The energy functional has the form

$$E_v[\rho] = \int \rho(r)v(r)dr + T_s[\rho] + \frac{1}{2}\int\int \frac{\rho(r_1)\rho(r_2)}{|r_1 - r_2|} dr_1 dr_2 + \Delta T[\rho] + \Delta U[\rho] \tag{2.13}$$

Then the exchange-correlation energy is defined as

$$E_{xc}[\rho] = \Delta T[\rho] + \Delta U[\rho] \tag{2.14}$$

Where $\Delta T[\rho]$ and $\Delta U[\rho]$ are unknown functionals of density. Substituting $E_{xc}[\rho]$ in Eq 2.13

$$E_0 = E_v[\rho] = \int \rho(r)v(r)d(r) + T_s[\rho] + \frac{1}{2}\int\int \frac{\rho(r_1)\rho(r_2)}{|r_1 - r_2|} dr_1 dr_2 + E_{xc}[\rho] \tag{2.15}$$

According to Hohenberg-Kohn variational principle [107]

$$\int \rho(r)dr = N \tag{2.16}$$

Here N is the number of electrons in the many-body system. Kohn and Sham introduced orbitals φ_i into DFT as a collection of auxiliary variables that had no physical significance and were only used for computing the overall energy and charge density. Then by putting the KS orbital φ_i instead of ρ, the kinetic energy term T_s reduced to the form

$$T_s[\rho] = \sum_{i=1}^{N} \left\langle \varphi_i \mid -\frac{\hbar^2}{2m}\nabla_i{}^2 \mid \varphi_i \right\rangle \tag{2.17}$$

By substituting Eq 2.16 and Eq 2.17, Eq 2.15 reduces to

$$\left[-\frac{\hbar^2}{2m}\nabla^2 + v(r) + \int \frac{\rho(r')}{|r-r'|}dr' + v_{xc} \right] \varphi_i = \varepsilon_i \varphi_i \tag{2.18}$$

This is the Kohn-Sham equation. Then the Kohn-Sham functional is given by

$$E_{KS}[\rho] = -\sum_{1=1}^{N} \frac{\hbar^2}{2m}\nabla_i{}^2 + v(r) + \frac{1}{2}\int\int \frac{\rho(r_1)\rho(r_2)}{|r_1 - r_2|}dr_1 dr_2 + E_{xc}[\rho] \tag{2.19}$$

2.2.1 Exchange-correlation energy

The exchange-correlation functional still needs to be discovered in the Kohn-Sham functional Eq 2.19. The E_{xc} is defened in Eq 2.14. According to the expression defined in Eq 2.14, E_{xc} contains [108] (1) Kinetic correlation energy, is the difference in the kinetic energy functional between the real and the noninteracting reference system (2) The exchange energy, which arises from the antisymmetric requirement (3) Coulombic correlation energy arises from the inter-electronic repulsion, and (4) A self-interaction correction. The exchange-correlation energy is the real dif-

ficulty in DFT. The results of DFT without exchange-correlation energy will not match those of experiments. Hence several approximation methods are proposed for exchange-correlation energy.

2.2.2 Local Density Approximation (LDA)

The Local density approximation (LDA)[107] considers electron density at each point in space. It assumes that the fluctuations of density are very slow. The LDA functional is expressed as

$$E_{xc}^{LDA}[\rho] = \int \rho(r)\mathscr{E}_{xc}^{LDA}(\rho(r))dr. \tag{2.20}$$

Here $\mathscr{E}_{xc}^{LDA}(\rho(r))$ is the exchange plus correlation energy per electron in a uniform electron gas with electron density ρ. The exchange-correlation energy is written as a sum of exchange and correlation terms linearly,

$$E_{xc} = E_x + E_c \tag{2.21}$$

LDA functionals apply only for slowly fluctuating systems or uniform electron gas and do not involve electron density gradients.

2.2.3 Generalized gradient approximation (GGA)

The Generalized gradient approximation (GGA) functionals overcome the LDA functionals by considering the gradient of electron density along with the density. These are expressed as

$$E_{xc}^{GGA}[\rho] = \int \rho(r)\mathscr{E}_{xc}^{GGA}((\rho(r)), |\nabla\rho(r)|)dr. \tag{2.22}$$

In all the computations, we have used GGA functionals proposed by Perdew, Burke, and Ernzerhof (PBE) [109].

2.2.4 Hybrid Functionals

Hybrid functionals are refined approximations of the exchange-correlation energy functional. In these hybrid approximations, part of the exact exchange is derived using the Hartree-Fock theory, and the rest by density functional approximations (DFA) like LDA or GGA (PBE). The correlation energy is entirely taken from DFA. In our calculation, DFA refers to PBE functional. The parameter that mixes the portion of HF exact exchange and the semilocal DFA exchange is known as the mixing parameter. The HF exact exchange is divided into short-range, long-range, and full-range potentials. The exchange-correlation energy for hybrid functionals is given by

$$E_{xc}^{HSE}(r) = \alpha E_x^{HF}(r, r'; \omega) + (1 - \alpha) E_x^{PBE}(r; \omega) + E_x^{PBE}(r; \omega) + E_c(r) \tag{2.23}$$

Here α and ω are the mixing and range separation parameters, respectively. In exchange-correlation energy, if the short-range part is replaced by α times the HF exact exchange and (1-α) times the PBE exchange and a long-range part with the correlation are fully taken by the PBE functionals, then the hybrid functionals are called short-range hybrid functionals. HSE06 [110, 111, 112] is one of the short-range hybrid functionals. Here the range separation parameter ω = 0.11 bohr^{-1}.

$$E_{xc}^{HSE}(r) = \alpha E_x^{SR-HF}(r, r'; \omega) + (1 - \alpha) E_x^{SR-PBE}(r; \omega) + E_x^{LR-PBE}(r; \omega) + E_c(r) \tag{2.24}$$

For the full-range hybrid functionals like PBE0 [113], corresponding exchange-correlation energy is given by

$$E_{xc}^{PBE0}(r) = \alpha E_x^{HF}(r, r') + (1 - \alpha) E_x^{PBE}(r) + E_c(r). \tag{2.25}$$

These hybrid functionals are known for their remarkable accuracy in predicting the band gap of bulk and 2D materials comparable with experimental values.

2.3 Dielectric-dependent hybrid functionals

In DFT, hybrid functionals are a prevalent and accurate method for predicting the electronic properties of a material. As shown in 2.2.4, the Hybrid functionals rely on the mixing parameter α. Apart from the success of hybrid functionals, the major problem in their computation arises based on the usage of α. One needs to understand the physical meaning of mixing parameters. In the hybrid functional, the mixing parameter α adds the portion of exact exchange from HF theory to the semilocal exchange functional of the DFT (LDA, GGA) and adds it with a semilocal correlation functional. In the screened exchange term of self-energy, the dielectric constant is taken as the screening term, and it is replaced by α^{-1} [114, 115]. By changing the α from 0 to 1, Hartree-Fock and semilocal KS exchange will continuously change. Hence by changing the α value, one can reproduce the experimental band gap. In HSE06 functional α is replaced by ϵ_∞^{-1}, ϵ_∞ is the static dielectric constant of a material and examined [116, 117]. These hybrid functionals with the mixing parameter termed screening parameter replaced by the inverse of the static dielectric constant are known as dielectric-dependent hybrid functionals(DDHF). These results in good band gap values with the experimental values [115, 118, 119, 120, 121, 122, 123]. In this work, band gap and static dielectric constant are calculated using the hybrid functionals, HSE06 and PBE0, by taking

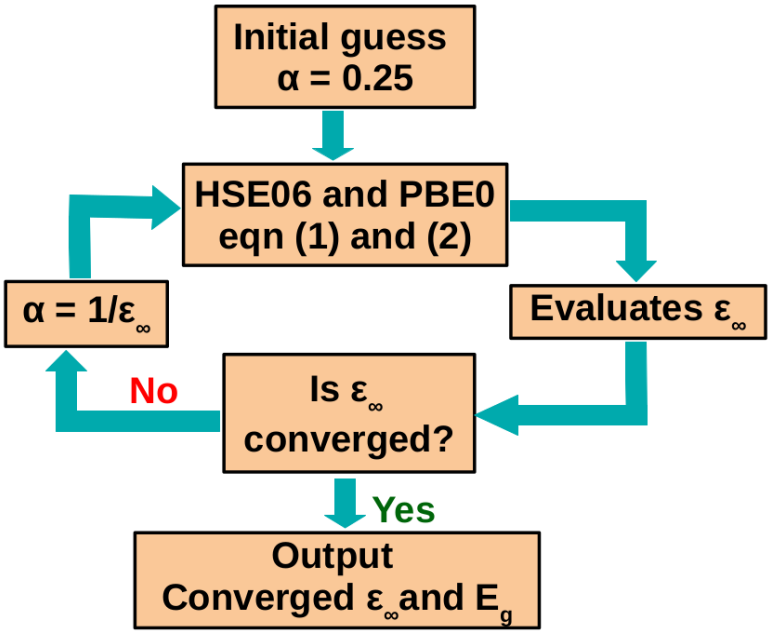

Figure 2.1: Self-consistent loop showing the DDHF calculations performed using HSE06 and PBE0 functionals.

α = 25% as an initial guess. In the next iteration, α is taken as the inverse of the dielectric constant calculated in the previous step and proceeded until the dielectric constant and band gap converge. The self-consistent DDHF calculations are proceeded as shown in Figure 2.1. The band gap reaches a constant value when the difference between the two consecutive dielectric constants is less than 0.01. Therefore the convergence criteria we followed in this work is $\epsilon_\infty < 0.01$. Further details of DDHF will be discussed in Chapter 3.

CHAPTER 3

ELECTRONIC AND OPTICAL PROPERTIES OF 3D TRANSITION METAL-DOPED SNS_2

In this chapter, we discuss the electronic bandgap and optical properties of SnS_2 and 3d-series transition metal-doped SnS_2 systems. The SnS_2 crystal is a non-magnetic indirect bandgap semiconductor both in bulk and in the monolayer limit. The transition metal substitution at Sn-site induces magnetism inside the crystal. Therefore studying its doping by 3d-series transition metals is essential from an application perspective. We use the dielectric-dependent hybrid functionals of ab initio calculations for computing the electronic bandgap. The dielectric-dependent hybrid computations rely on the electronic static dielectric constant. In these calculations, we iteratively update the dielectric constant and exchange parameter from one another until the convergence. As a result, we present a range of possible bandgap values. Specifically, we determine the lower and upper bounds of possible experimental bandgap values for all these doped systems. Further, we explore the optical properties of each doped system in the monolayer and bulk forms. We discuss the absorption spectra, optical constants, and exciton binding energy of all the doped systems. We conclude that the transition metal doped SnS_2 is a good candidate for optoelectronic device applications. The reuslts are published in Physical Review B 105, 195205 (2022) [291].

3.1 Introduction

Layered metal dichalcogenides (LMDs) are found in nature as bulk crystals with Van der Waals interactions connecting the layers. These are promising materials for field effect devices, memory devices, and energy storage e.t.c. Monolayers of them can be extracted via experimental techniques. The first monolayer to be produced experimentally is graphene [125]. Other layered materials of the form MX_2, where M = Ti, Hf, Zr and X= S, Se, Te [126, 127, 128, 129, 130, 131, 132, 133, 134, 135] as well as the transition metal(TM) dichalcogenides MoS_2 [136, 137, 138, 139], WS_2 [140, 141], WSe_2 [142, 143], and NbS_2 [144], are exceedingly promising materials due to their applications in electrical, optical, and magnetic fields.

As a metal dichalcogenide, SnS_2 originates from the MX_2 or CdI_2 crystal type [145]. The chemical stability of SnS_2 crystal makes it a non-toxic, non-flammable, affordable, and earth-abundant material that can resist water and air. The layered structure of SnS_2 allows one to synthesize it in a single layer. The single-layer provides a large surface area for solar energy absorption and active sites for chemical reactions. The optical properties of the SnS_2 crystal are well studied. Also SnS_2 is an earth-abundant visible-light photocatalyst [74], making it a good candidate for Li-ion battery electrode [81, 82], gas sensors [83], and field emitters [84]. The exfoliated nano-membranes of SnS_2 exhibit a high FET on/off ratio exceeding 2×10^6 and a carrier mobility of 1 $cm^2V^{-1}s^{-1}$ [85]. High-performance top-gated field-effect transistor along with the integrated logic circuits have been fabricated [86] in 2013, using monolayer SnS_2 crystals. Thus, SnS_2 will be a top candidate for next-generation electronic gadgets.

SnS_2 crystal shows n-type electrical conductivity with a maximum dark value of 1.3×10^{-2} cm^{-1}, and activation energy of 0.14 eV with a wide bandgap of 2.3 eV [146]. Thus a complete solar cell structure is built using SnS_2 crystal [146]. These

findings imply that SnS_2, a layered semiconductor with a wide bandgap, will be a nanoelectronic basis material, particularly as a supplement to graphene-based materials with very small or no bandgap. SnS_2 is an indirect gap semiconductor in bulk and the monolayer limit, with a wide bandgap of 2.2-2.43 eV. Therefore, a bandgap narrowing process is required for applications like solar cells. Narrowing it to nearly 1.5 eV and then maintaining the higher absorption coefficient is essential [147, 148, 149]. Attempts are made using defect engineering [150, 151, 152, 153] and impurity doping [71, 154] for reducing the bandgap. Transition metal doping of the SnS_2 crystal in monolayer or bulk environments make its bandgap fall below the bandgap of pristine SnS_2 crystal.

Electronic properties of materials profoundly influence electronic, optoelectronic, and spintronic device applications. However, predicting electronic properties accurately with theoretical methods is a complex problem. Theoretical predictions do not match the experimental values very well. Thus computational methods play a major role. In this regard, density functional theory [155] (DFT) is one of the popular methodologies that provides a good balance between accuracy and computation efficiency. The electronic bandgap calculations using DFT involve exchange-correlation functionals such as local density approximation (LDA) [156], semi-local generalized gradient approximation (GGA) [109] and hybrid functionals [157, 158, 159]. Among these functionals, hybrid functionals are highly accurate [160, 161]. They are the refined approximations to the exchange-correlation energy functional. In these hybrid approximations, part of the exact exchange is derived using the Hartree-Fock theory, and the rest by density functional approximations (DFA). Hybrid functionals are classified using the Hartree-Fock exchange admixtures. They are short-range, long-range, or full-range separation. The effective non-local potential in the generalized Kohn-Sham formalism [162, 163, 164] is

determined by

$$v_{GKS} = v_H(r) + v_{xc}(r, r') + v_{ext}(r), \tag{3.1}$$

where v_H is the Hartree potential, v_{xc} is the exchange-correlation potential and v_{ext} is the external potential of the nuclei. Also v_{xc} can be expressed as

$$v_{xc} = v_x^{HF} + v_x^{DFA} + v_c(r), \tag{3.2}$$

Where v_x^{HF} and v_x^{DFA} represent the exact exchange potentials corresponding to the Hartree-Fock and density functional approximations respectively. $v_c(r)$ is the correlation potential.

$$v_x^{HF} = v_x^{SR-HF} + v_x^{LR-HF}, \tag{3.3}$$

$$v_x^{DFA} = v_x^{SR-DFA} + v_x^{LR-DFA}. \tag{3.4}$$

The terms represent the short-range and long-range part of the exact exchange potentials corresponding to the Hartree-Fock and the density functional approximations.

$$\begin{aligned} v_{xc} = {} & \alpha v_x^{SR-HF}(r, r'; \omega) + (1 - \alpha) v_x^{SR-DFA}(r; \omega) \\ & + \beta v_x^{LR-HF}(r, r'; \omega) + (1 - \beta) v_x^{LR-DFA}(r; \omega) \\ & + v_c(r), \end{aligned} \tag{3.5}$$

where α and β are mixing parameters for short-range and long-range exchange potentials. ω is the range separation parameter that separates the short-range and the long-range Hartree-Fock exchange potentials. Hartree-Fock exchange poten-

tials are expressed as [165, 121]

$$v_x^{LR-HF}(r,r';\omega) = -\sum_{i=1}^{N_{occ}} \phi_i(r)\phi_i^*(r')\frac{erf(\omega|r-r'|)}{|r-r'|}, \tag{3.6}$$

$$v_x^{SR-HF}(r,r';\omega) = -\sum_{i=1}^{N_{occ}} \phi_i(r)\phi_i^*(r')\frac{erfc(\omega|r-r'|)}{|r-r'|}. \tag{3.7}$$

Here ϕ_i are single-particale occupied electronic orbitals, erf and $erfc$ are error function and complimentary error functions respectively. The Coulomb potential [157] is expressed as

$$\frac{1}{|r-r'|} = \frac{erfc(\omega|r-r'|)}{|r-r'|} + \frac{erf(\omega|r-r'|)}{|r-r'|}. \tag{3.8}$$

With a fixed mixing parameter, α and β the hybrids are called global-hybrid functionals. The hybrid functionals where the mixing parameter changes with material-dependent properties are known as local hybrid functionals. When $\beta = 0$, the equation (3.5) becomes

$$\begin{aligned} v_{xc}(r) = \alpha v_x^{SR-HF}(r,r';\omega) + (1-\alpha)v_x^{SR-DFA}(r;\omega) \\ + v_x^{LR-DFA}(r;\omega) + v_c(r) \end{aligned}. \tag{3.9}$$

These are the short-range hybrid functionals e.g HSE06 [110, 111, 112], here α = 0.25 and ω = 0.11 bohr^{-1}. When $\beta \neq 0$, then these are the long-range hybrid functionals e.g CAM-B3LYP functionals [166, 167] where β = 0.65, α = 0.19, ω = 0.33 bohr^{-1}. The full-range hybrid functionals are with $\alpha = \beta$. For full range hybrid functionals we have,

$$\begin{aligned} v_{xc}(r) = \alpha v_x^{SR-HF}(r,r';\omega) + (1-\alpha)v_x^{SR-DFA}(r;\omega) \\ + \alpha v_x^{LR-HF}(r,r';\omega) + (1-\alpha)v_x^{LR-DFA}(r;\omega) \\ + v_c(r) \end{aligned} \tag{3.10}$$

$$\begin{aligned} v_{xc}(r) &= \alpha(v_x^{SR-HF}(r,r';\omega) + v_x^{LR-HF}(r,r';\omega)) \\ &\quad + (1-\alpha)(v_x^{SR-DFA}(r;\omega) + v_x^{LR-DFA}(r;\omega)), \\ &\quad + v_c(r) \end{aligned} \tag{3.11}$$

$$v_{xc}(r) = \alpha v_x^{HF}(r,r') + (1-\alpha)v_x^{DFA}(r) + v_c(r). \tag{3.12}$$

In our calculation, DFA refers to PBE functional. For the full-range hybrid functionals like PBE0 [113] we have α = 0.25. These hybrid functionals are known for their remarkable accuracy in predicting the bandgap of bulk and 2D materials comparable with experimental values. However, they are computationally expensive. The electronic dielectric constant, ϵ_s is known to be a reliable screening parameter for understanding the exact exchange potential in non-metallic systems. Miguel A.L. Marques et al [115], T. Shimazaki and Y. Asai [168, 169, 120, 121] and Sivan Refacly-Abramson [122] reported that the electronic static dielectric constant of a non-metallic system represents the effective screening of the exact-exchange potential, $v_x^{screened}$. T. Shimazaki and Y. Asai calculated the band structure of Diamond using the screened Fock exchange method [170] in which they have utilized the Bechstedt model [171] for dielectric function and simplified it in the form of screened Fock exchange,

$$v_x^{screened} = \left(1 - \frac{1}{\epsilon_s}\right)[v_{SR-X}^{erfc}] + \frac{1}{\epsilon_s}v_x^{Fock}. \tag{3.13}$$

They have calculated the bandgap of Diamond using the self-consistent screened Hartree-Fock exact exchange potential, which is in agreement with the experiment. Nevertheless, exactly how much exchange rate was involved in their calculation is not specified.

In a semiconductor system, the static dielectric constant, ϵ_∞ facilitates effective

screening. Miguel A.L. [115] et al. reported that the static dielectric constant calculated using the PBE functional, ϵ_{∞}^{PBE} could be related to the mixing parameter of the full-range hybrid functional as

$$\alpha = \frac{1}{\epsilon_{\infty}^{PBE}}. \tag{3.14}$$

On the other hand using self-consistent scheme, T. Shimazaki and Y. Asai [116, 172] evaluated the relation

$$\alpha = \frac{1}{\epsilon_{\infty}}, \tag{3.15}$$

for both short-range and full-range screened hybrid functionals. Koller et al [173] reported that, in self-consistent short-range hybrid functionals the mixing parameter is inversely proportional to the static dielectric constant of the system. In recent publications, several authors have proposed introducing α as an adjustable parameter into solids to reproduce the experimental bandgap [174, 175, 176, 177, 178].

In our computations, initially, the self-consistency loop is triggered by a guess for α, which ranges between 0 and 1; the estimate determines the exact amount of exchange included in the exchange-correlation potential expression. In this dielectric-dependent hybrid functional (DDHF) calculation, the static dielectric constant is calculated with HSE06 and PBE0 functionals based on the initial guess of α as 25%. In the first iteration of HSE06 and PBE0 calculation, exchange parameter is α = 25%. The inverse of the static dielectric constant calculated in the first iteration is taken as the exchange parameter for the next iteration. These steps are repeated until the static dielectric constant, and hence the bandgap converges. Convergence is reached when the consecutive difference between the calculated static dielectric constant, $\epsilon_{\infty} < 0.01$. When the static dielectric constant converges, the bandgap also converges. These self-consistent HSE06 and PBE0 calculations are performed to find the bandgap of bulk and monolayer SnS_2 and all the transi-

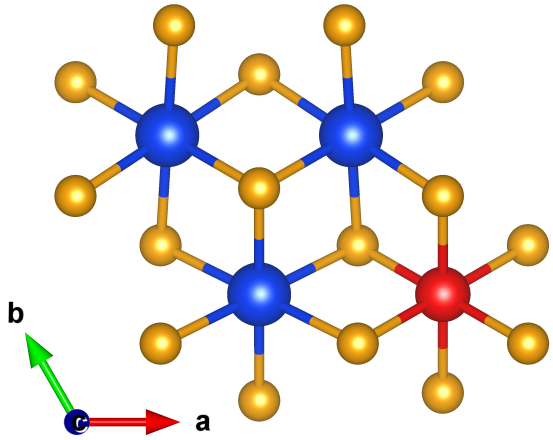

Figure 3.1: Top view of SnS_2 crystal doped with transition metal atom. Blue, yellow and red balls represent Sn, S and transition metal atom respectively.

tion metal-doped systems. We also use the inverse of the static dielectric constant obtained by the PBE functional to do a one-run hybrid functional computation to estimate the bandgap.

3.2 Computational Details

First principle calculations [179] are performed by using Vienna *ab initio* Simulation Package(VASP) [180, 181]. The electron-ion interactions in these calculations were carried by projector augmented wave (PAW) [182, 183] pseudopotentials. Since SnS_2 is a layered Van der Waals material, the Van der Waals interaction is involved in the DFT calculation. The bulk and ML-SnS_2 crystals are relaxed using Perdew, Burke, and Enzerhof (PBE) Generalized Gradient Approximation (GGA) [109] with *D*3 [184], optB86b [185] vdw-functions to calculate the ground state lattice parameters respectively. While doing the calculations, atomic positions are optimized using the conjugate-gradient method with a force convergence criterion of 10^{-3} eV/Å and a tight energy convergence criterion of 1×10^{-8} eV. Cutoff energy of 400

eV is used. The Brillouin zone sampling of bulk and ML-SnS_2 was employed by Monkhorst-Pack [186] k-grid of size 21×21×13 and 21×21×1 respectively. The electronic bandgap values are estimated using the short-range i.e Heyd-Scuseria-Ernzerhof (HSE06) [110, 111, 112] and full-range i.e PBE0 [187] screened hybrid functionals with 25% exchange for the initial guess. A supercell of size 2×2×1 is considered. One of the Sn atoms is replaced by each transition metal atom. The top view of the supercell doped with the transition metal atom is shown in Figure 3.1. A self-consistent hybrid scheme is used for calculating the electronic part of the static dielectric constant. Each time, a fraction of the exact exchange of screened hybrid functional is calculated by the inverse of ϵ_∞. In this calculation, the LOPTICS tag in VASP employs the Kramers-Kronig transformation to separate the real part of the frequency-dependent dielectric function. The static dielectric constant is calculated using this code, and the local field effects are neglected to reduce the computational cost. For bulk systems, the average of the dielectric constants along the x, y, and z axes is considered. For monolayers the dielectric constant is calculated using the relation

$$\varepsilon_{2D} = \frac{1}{3}\left(2\varepsilon_{2D,\parallel} + \varepsilon_{2D,\perp}\right) \tag{3.16}$$

by eliminating the vacuum contribution. Where $\varepsilon_{2D,\parallel}$ and $\varepsilon_{2D,\perp}$ are the in-plane and out of plane dielectric constants of the proper 2D material. It is taken from the simple capacitor combinations of series and parallel connections of the slab-vacuum model proposed in [188].

3.3 Results and Discussion

3.3.1 Structural stability

It is important to calculate the formation energy of each transition metal-doped SnS_2 both in the bulk and monolayer form to explore the stability of the systems. The formation energy of the TM-doped systems are calculated using the relation [189, 190],

$$E_{form} = E_{doped} - E_{pristine} - n\mu_{TM} + n\mu_{Sn}. \tag{3.17}$$

Here E_{doped} and $E_{pristine}$ are the energies of transition metal-doped and pristine systems respectively. n is the number of Sn atoms replaced with transition metal atom. μ_{TM} and μ_{Sn} are the chemical potentials of the transition metal and Sn-atom, respectively. For the pristine SnS_2 crystal the chemical potentials of Sn and S should satisfy [191]

$$\mu_{Sn} + 2\mu_S = \Delta E_f(SnS_2) \tag{3.18}$$

where $\Delta\ E_f(SnS_2)$ is the enthalpy of formation of SnS_2. Formation energy of such reaction is given by [192],

$$E_{form}(SnS_2) = \mu_{SnS_2} - \mu_{Sn,bulk} - 2\mu_{S,bulk} \tag{3.19}$$

Where $\mu_(SnS_2)$ is the energy per unit cell of the SnS_2 crystal. $\mu_{Sn,bulk}$ and $\mu_{S,bulk}$ are the energy per atom of the bulk Sn and bulk S crystal structure. The formation energy of bulk and ML SnS_2 are calculated as -1.48 and -0.95 eV/atom, respectively. Several thermodynamic constraints are applied to the chemical potentials to avoid the formation of elemental phases (Sn, S and TM-atom) and the secondary phases by TM-atom with S-atom [191]. The constraints applied to the chemical potentials

are [191],

$$\mu_{Sn} < 0, \mu_S < 0, \mu_{TM} < 0, \tag{3.20}$$

$$n\mu_{TM} + m\mu_S \leq \Delta E_f(TM_nS_m). \tag{3.21}$$

where $\Delta E_f(TM_nS_m)$ is the enthalpy of formation for the secondary phase TM_nS_m. The chemical potentials of TM-atoms are calculated using the equations (3.20) and (3.21). Since SnS_2 has two-type of atoms Sn and S, we need to find the formation energies both in Sn-rich (S-poor) and Sn-poor (S-rich) experimental growth conditions. These conditions are based on the chemical potentials of the individual atoms. In Sn-rich and Sn-poor conditions μ_{Sn} is given by [192],

$$\mu_{Sn}^{Sn-rich} = \mu_{Sn,bulk}, \tag{3.22}$$

$$\mu_{Sn}^{Sn-poor} = \mu_{\mathrm{Sn,\,bulk}} + \Delta E_f(\mathrm{SnS_2}). \tag{3.23}$$

The maximum allowed chemical potential of TM-atom is considered to calculate the formation energy of each doped system in Sn-rich and Sn-poor conditions [191]. All the potential secondary phases of TM-atoms and bulk phases of Sn and S-atoms are taken from Materials Project [193], and their energies are calculated using VASP.

Figure 3.2 shows the formation energy of transition metal-doped bulk and ML-SnS_2 in the Sn-rich and Sn-poor conditions. Here the green line (Sn-poor) falls below the red (Sn-rich) line. This indicates the lower formation energy in the Sn-poor (S-rich) condition than in Sn-rich (S-poor) condition in all the transition metal-doped systems. Hence Sn-poor (S-rich) condition is the favourable condition to incorporate the transition metal atoms into SnS_2-crystal. As a result, the impurities Ti, V, Cr, Mn, Fe, Co, Ni, Cu, and Zn are comparatively easy to inte-

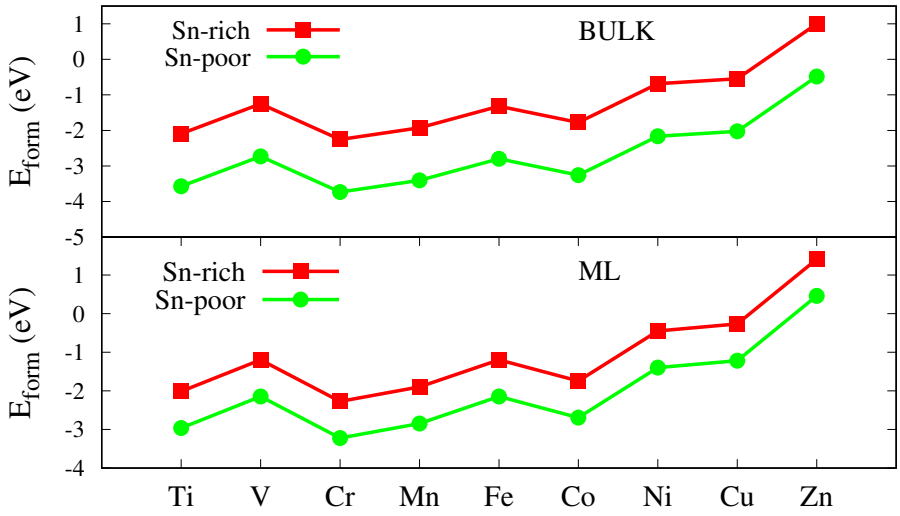

Figure 3.2: Formation energy of transition metal-doped bulk and ML-SnS_2.

grate into the SnS_2 crystal at the Sn-site in Sn-poor(S-rich) condition. Therefore, further calculations are performed based on substitutional doping at the Sn-site by the transition metal atom.

3.3.2 Dielectric response of a proper 2D-material

In a 2D material, the electrons are bound to the two-dimensional plane. Consequently, a 3D system can be converted to a quasi-2D system by filling a vacuum in one direction. However, the dielectric response will be strongly affected by the vacuum known as vacuum effect. Due to the periodicity of the two-dimensional environment, neither VASP nor any comparable computational tool can calculate the dielectric constant of a proper two-dimensional system. Thus it is necessary to eliminate the vacuum contribution to the dielectric response calculated by VASP. For this purpose we use the simple capacitor combinations of series and parallel connections for the slab-vacuum model proposed in [188]. We have calculated the dielectric constant of a monolayer SnS_2 and TM-doped monolayer SnS_2 systems using dielectric dependent hybrid functionals.

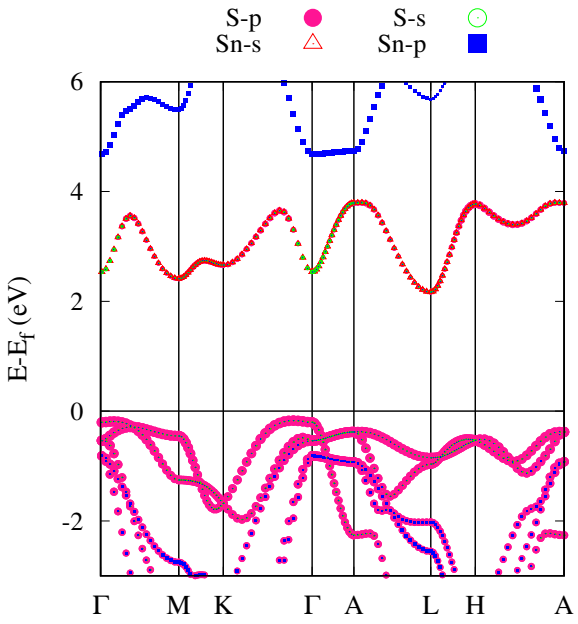

Figure 3.3: Orbital projected band structure of bulk SnS_2 calculated using HSE06 functional with 25% exchange.

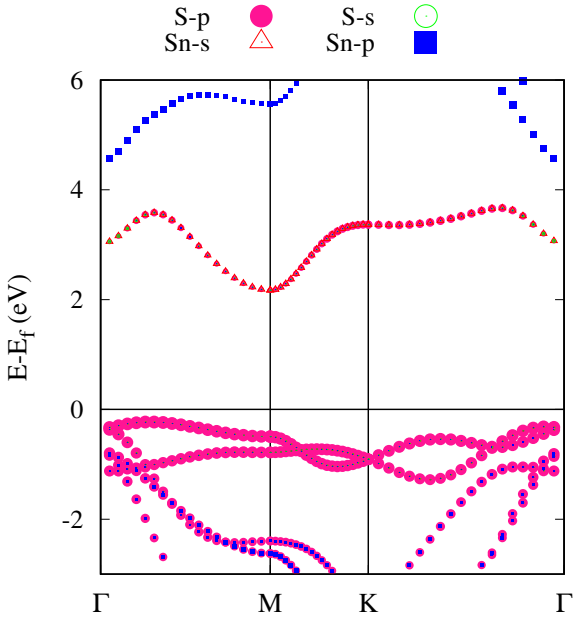

Figure 3.4: Orbital projected band structure of monolayer SnS_2 calculated using HSE06 functional with 25% exchange.

Table 3.1: Relaxed lattice parameters (a,b and c), Sn-S bond length d_{Sn-S}, direct E_g^{dir} and indirect bandgap E_g^{in}, values of bulk and monolayer SnS_2 calculated using PBE, PBE-D3 and PBE-optB86b functionals respectively. The HSE06 and PBE0 bandgap values are calculated using PBE (D3 and optB86b) relaxed lattice parameters.

System	PBE a=b (Å)	c (Å)	d_{Sn-S} (Å)	E_g^{in} (eV)	E_g^{dir} (eV)	HSE06 E_g^{in} (eV)	HSE06 E_g^{dir} (eV)	PBE0 E_g^{in} (eV)	PBE0 E_g^{dir} (eV)
BULK-SnS_2	3.64 (3.69) [67] (3.649) [58]	5.98 (5.98) [67] (5.899) [58]	2.60 (2.62) [67]	1.41	1.92 [L]	2.22(D3) 2.35 (optB86b) (2.18) [59] (2.07) [194] (2.28) [74] (2.25) [195]	2.66[L] 2.5[M] (D3) (2.88) [L] [194] (2.56) [M] [74] (2.61) [L] [59]	2.83 (optB86b)	3.36 [M] (optB86b)
ML-SnS_2	3.68 (3.68) [196]	-	2.59 (2.59) [196]	1.45 [M]	1.69	2.43 (2.41) [59]	2.64 [M] (2.68) [M] [59]	3.11	3.41[M]

A 2D material has a two dimensional slab and a vacuum filled in another direction. Hence we can propose it as a slab-vacuum model. Figure 3.5 shows the supercell of a slab-vacuum model. Here the capacitance of a supercell C_{SC} can be expressed as a series and parallel combinations of the capacitance of two dimensional-slab(layer) C_{2D} and the capacitance of vacuum layer C_{Vac}. To eliminate the vacuum contribution in out of plane direction we consider C_{SC} as a series

combination of C_{Vac} and C_{2D}.

$$\frac{1}{C_{SC,\perp}} = \frac{1}{C_{2D,\perp}} + \frac{1}{C_{Vac}}, \tag{3.24}$$

$$\frac{c}{\varepsilon_{SC,\perp}} = \frac{t}{\varepsilon_{2D,\perp}} + \frac{c-t}{\varepsilon_{Vac}}, \tag{3.25}$$

$$\varepsilon_{2D,\perp} = \left[1 + \frac{c}{t}\left(\frac{1}{\varepsilon_{SC,\perp}} - 1\right)\right]^{-1}. \tag{3.26}$$

To eliminate the vacuum contribution along in-plane direction we consider C_{SC} as parallel combination of C_{2D} and C_{Vac}.

$$C_{SC,\parallel} = C_{2D,\parallel} + C_{Vac}, \tag{3.27}$$

$$c\varepsilon_{SC,\parallel} = t\varepsilon_{2D,\parallel} + (c-t)\varepsilon_{Vac}, \tag{3.28}$$

$$\varepsilon_{2D,\parallel} = \left[1 + \frac{c}{t}\left(\varepsilon_{SC,\parallel} - 1\right)\right]. \tag{3.29}$$

where c, t and $c - t$ are the thicknesses of the supercell, 2D-layer and vacuum respectively. Further, $\varepsilon_{SC}, \varepsilon_{2D}$ and $\varepsilon_{Vac} = 1$ are the dielectric constant of the supercell, 2D-layer and vacuum respectively. Using the out of plane and in-plane dielectric constants one can find the dielectric constant of proper 2D-material as

$$\varepsilon_{2D} = \frac{1}{3}\left(2\varepsilon_{2D,\parallel} + \varepsilon_{2D,\perp}\right). \tag{3.30}$$

Using the above relations, the dielectric constant of pristine and transition metal doped monolayer SnS_2 systems are calculated.

3.3.3 Electronic properties

Bulk SnS_2 crystal is a 2H-polytype, it has hexagonal crystal structre with the space group of $P\bar{3}m1$ [59, 197, 58]. The six sulfur ligand field octahedrally surrounds the central Sn-atom with Sn-S bond length of 2.60 Å. The calculated in-plane and

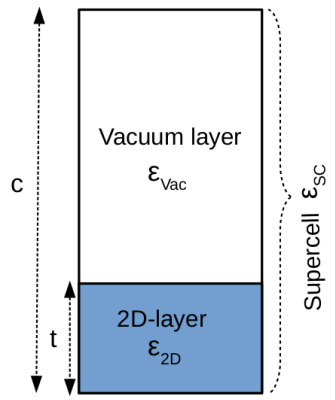

Figure 3.5: Schematic diagram of supercell of a slab-vacuum model.

transverse lattice parameters using vdw-D3 functionals are 3.64 Å and 5.98 Å respectively. These values are in agreement with the other theoretical work [67] where a = 3.69 Å and c = 5.98 Å. Note that the single crystal XRD [58] also has the parameters a = 3.649 Å and c = 5.899 Å . Monolayer SnS_2 crystallizes to the same space group whose top view and side views are same as the bulk SnS_2. The in-plane lattice parameter is found to be 3.68 Å using PBE functional. And the Sn-S bond length is 2.59 Å. The band structure of pristine bulk SnS_2 is shown in Figure 3.3. This shows, bulk-SnS_2 has indirect gap nature like bulk MoS_2. In bulk MoS_2, the indirect gap appears due to the in-plane electronic transition. This transition happens from valence band edge at Γ - point to conduction band edge between Γ and K-point. In bulk-SnS_2, even though it is indirect, the valence band edge is near Γ - point and conduction band edge is out of plane, at L-point.

Valence band edge in bulk MoS_2 emerges from out of plane S-p_z and Mo-d_{z^2} orbitals, whereas conduction band edge is from S-p_x,p_y,p_z and Mo-d_{xy},$d_{x^2-y^2}$,d_{z^2} orbitals [198]. In bulk-SnS_2, valence band edge originates from the S-p_x,p_y,p_z and Sn-p_z orbitals, conduction band edge is from Sn-s and S-p_x,p_y orbitals. Valence bands are mainly composed of S-p_x,p_y,p_z and Sn-s,p_x,p_y,p_z orbitals near the Fermi level. The conduction bands are composed of S-p_x,p_y and Sn-s orbitals very near

to the Fermi level. Sn-p_x,p_y,p_z orbitals influence the conduction band far from the Fermi level. The fundamental (indirect) band-gap calculated using HSE06 functional with D3 and optB86 corrections are 2.22 and 2.35 eV respectively for the exchange fraction of α=25%. They are in agreement with the various research works shown in Table 3.1. An experimental bandgap value is 2.25 eV [195], Greenaway and Nitsche showed the value 2.21 eV [145] and D.C Lokhande gave the value to be 2.35 eV [199]. Our bandgap values are comparable with these experimental values. The direct gap calculated at L and M-points is 2.66 eV and 2.5 eV, respectively. The PBE0+optB86b functional gives the gap of 2.83 eV. This is higher than the calculated theoretical and experimental gaps.

In the case of monolayer MoS_2, both valence band edge and conduction band edge originate at the K-point. This makes it as direct gap semiconductor. In this case, valence band edge is composed of Mo-d_{xy}+d_{x2-y2}, S-p_x+p_y orbitals and conduction band edge is of Mo-d_z^2, S-p_x+p_y orbitals [198]. Similar to MoS_2, indirect to direct gap transition occurs from bulk to monolayer limit in all of the transition metal dichalcogenides. However, this phenomenon does not occur in the case of SnS_2. In monolayer SnS_2, valence band edge originates near Γ-point from the S-p_x and Sn-p_y orbital, whereas conduction band edge originates at M-point from the Sn-s and S-p_x,p_y orbitals. This makes it an indirect gap semiconductor. The band structure is shown in Figure 3.4. The valence bands near Fermi level are due to S-p_x,p_y and Sn-p_x,p_y and s orbitals. The conduction bands are from Sn-s,p_x,p_y and S-p_x,p_y orbitals. The experimental bandgap is 2.29 eV [200]. The HSE06 functionals with α=25% have shown the band-gap of 2.4 eV. This is comparable with the other theoretical works shown in Table 3.1. But the bandgap of 3.11 eV calculated by PBE0 with α=25% overestimates the other theoretical and experimental bandgap values. The direct gap calculated at the M-point using HSE06 is 2.64 eV. Bulk (2.35 eV) and monolayer (2.4 eV) limit show that, SnS_2 has a wider bandgap compared

Table 3.2: Bandgap of bulk SnS_2 and TM-doped semiconductor systems estimated using DDHF calculations. Where $\alpha = \frac{1}{\epsilon^{SC-HSE}}$ and $\frac{1}{\epsilon^{SC-PBE0}}$ use converged dielectric constant calculated using HSE06 and PBE0 under self-consistent scheme. $\alpha = \frac{1}{\epsilon^{PBE}}$ uses the dielectric constant calculated using PBE functionals. Bandgap values are in eV.

	HSE06			PBE0		
System	$\alpha = 25\%$	$\alpha = \frac{1}{\epsilon^{SC-HSE}}$	$\alpha = \frac{1}{\epsilon^{PBE}}$	$\alpha = 25\%$	$\alpha = \frac{1}{\epsilon^{SC-PBE0}}$	$\alpha = \frac{1}{\epsilon^{PBE}}$
Bulk-SnS_2	2.35	1.68	1.7	2.83	2.06	1.83
Ti	1.58	0.61	0.45	2.28	1.13	0.62
V	1.05	0.0	0.0	0.51	0.0	0.0
Mn	1.36	0.51	0.71	2.06	0.93	1.26
Fe	0.9	0	0.5	1.58	0.09	1.09
Ni	0.91	0.47	0.42	1.63	0.77	0.83

to transition metal dichalcogenides. This is in contrast with phosphorene [72, 73], where the layer thickness greatly influences the bandgap.

3.3.4 Importance of DDHF calculation

The dielectric constant is equivalent to effective screening in semiconductor systems, as discussed in the introduction. The mixing parameter is inversely related to the static dielectric constant in hybrid functionals. This fact is investigated for a variety of materials [115, 118, 119, 120, 121, 122, 123]. Instead of randomly choosing the exchange percentage value, the DDHF allows one to manually calculate the value of the exchange parameter based on the inverse static dielectric constant. The self-consistent steps performed by incorporating the exchange parameters into hybrid functionals provide the bandgap values until convergence is reached. Bandgap remains unchanged when the dielectric constant and exchange

Table 3.3: Bandgap of monolayer SnS_2 and TM-doped semiconductor systems estimated using DDHF calculations. Where, $\alpha = \frac{1}{\epsilon^{SC-HSE}}$ and $\frac{1}{\epsilon^{SC-PBE0}}$ use converged dielectric constant calculated using HSE06 and PBE0 under self-consistent scheme. $\alpha = \frac{1}{\epsilon^{PBE}}$ uses the dielectric constant calculated using PBE functionals. Bandgap values are in eV.

	HSE06			PBE0		
System	$\alpha = 25\%$	$\alpha = \frac{1}{\epsilon^{SC-HSE}}$	$\alpha = \frac{1}{\epsilon^{PBE}}$	$\alpha = 25\%$	$\alpha = \frac{1}{\epsilon^{SC-PBE0}}$	$\alpha = \frac{1}{\epsilon^{PBE}}$
ML-SnS_2	2.43	1.89	1.85	3.11	2.23	2.11
Ti	1.80	1.17	1.05	2.48	1.60	1.25
V	1.30	0.0	0.0	1.75	0.0	0.0
Cr	1.72	0.0	0.0	2.44	0.54	0.3
Mn	1.75	1.03	0.93	2.43	1.34	1.1
Fe	1.50	0.31	0.02	2.19	0.63	0.05
Ni	1.50	0.99	0.94	2.22	1.27	1.11
Cu	0.0	0.0	0.0	0.73	0.0	0.0

parameter converges. These iterations highlight how the bandgap values change depending on the dielectric constant of the system and how it depends on the exchange parameter.

In this sense, DDHF is not only important in calculating the range of bandgap values but also provides the converged bandgap value and minimal exchange percentage a system can have. There is no fixed value for the exchange percentage in the hybrid DFT calculations. One can easily understand this by considering the TiS_2 example. Finding the experimentally matchable bandgap of 1T-TiS_2 using theoretical methods was a challenge for DFT calculations. We have first examined the bandgap calculation of a bulk 1T-TiS_2. According to some tests, it has either semiconducting [201] or semimetallic [202] behaviour. Klipstein and Friend [203] found that TiS_2 is a semiconductor with a gap of 0.18 ± 0.06 eV, Greenway and Nische [145] found that it is a semiconductor with a bandgap of 1-1.12 eV by the optical measurement. Using angle-resolved photoemission studies (ARPS)

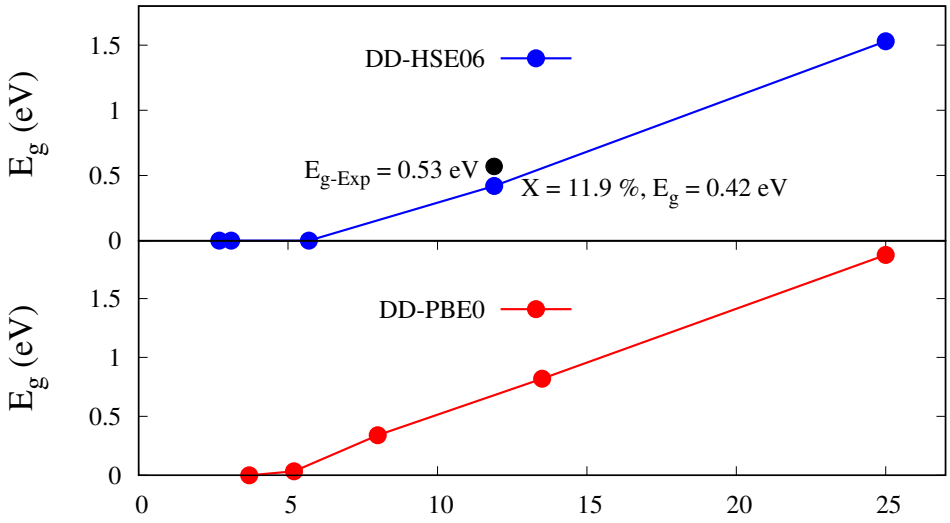

Figure 3.6: Dielectric dependent HSE06 and PBE0 bandgap values of 1T-TiS_2.

Chen et al [201] and Barry et al [204] found a bandgap of about 0.3± 0.2 eV. Using photoemission experiments, Shepherd and Williams [205] determined a bandgap of less than 0.5 eV. A bandgap of 2 eV was estimated using the pseudopotential approach [202]. By employing the linearized augmented plane wave (LAPW) method [206], augmented spherical wave (ASW) method [207], the linear muffin-tin orbital (LMTO) method [208, 209, 210] and the full-potential (FP)-LAPW method [211, 212] have claimed that TiS_2 displays semimetallic behavior. Using resistivity measurements [213, 214], several experiments have concluded that TiS_2 shows metallic behaviour.

The latest experiment on TiS_2 utilising angle-resolved photoelectron spectroscopy (ARPES) [215] verifies the semiconducting nature with a bandgap of 0.53 eV, while the HSE06 calculation with 20% exchange yields a bandgap of 0.4 eV [215]. Our band structure computations utilised LDA, GGA, and meta-GGA (SCAN) functionals and revealed the metallic nature. HSE06 and PBE0 with alpha = 25% yield bandgaps of 1.53 eV and 1.87 eV, respectively, overestimating the ARPES bandgap of 0.53 eV [215]. Finally, our DDHF calculations gave 0.42 eV for the 11.9% exchange and 0.34 eV for the 8% exchange, respectively, after which the TiS_2 system

Table 3.4: Static dielectric constant and bandgap of bulk SnS_2 and TM-doped semiconductor systems estimated using DDHSE06 functionals. Cr, Cu, Co and Zn-doped systems are metals. Bandgap values are in eV.

System		HSE^1	HSE^2	HSE^3	HSE^4	HSE^5	HSE^6	HSE$^{one-run}$
Bulk-SnS_2	ϵ_∞	6.713	8.521	8.721	8.885	8.910	8.90	8.7
	E_g	2.35	1.721	1.673	1.682	1.681	1.680	1.7
Ti	ϵ_∞	6.801	9.121	9.960	9.953	9.952	9.950	11.48
	E_g	1.581	0.811	0.652	0.611	0.610	0.610	0.45
V	ϵ_∞	7.282	16.960	16.960	16.960	16.960	16.960	15.8
	E_g	1.05	0.0	0.0	0.0	0.0	0.0	0.0
Mn	ϵ_∞	6.852	8.812	9.416	9.5	9.86	9.86	8.81
	E_g	1.36	0.711	0.572	0.553	0.512	0.510	0.71
Fe	ϵ_∞	6.541	7.982	8.470	9.771	9.811	9.811	7.7
	E_g	0.981	0.170	0.0	0.0	0.0	0.0	0.5
Ni	ϵ_∞	9.310	12.611	13.419	13.551	13.612	13.610	14.24
	E_g	0.911	0.542	0.474	0.472	0.471	0.471	0.42

reaches a metallic phase which is shown in Figure 3.6. The bandgap of 0.42 eV calculated with the 11.9% exchange of DD-HSE06 now matches the gap of 0.4 eV estimated by other theory work [215], as well as the experimental bandgap of 0.53 eV [215]. This demonstrates that the experimental bandgap value is calculated for the exchange value of 11.9% rather than 25%. DDHF has calculated the experimental matchable bandgap value despite the system gaining the metallic phase. This confirms that a system's fundamental bandgap or experimental bandgap falls within one of the DDHF bandgap values. This also demonstrates that for a given exchange value, every semiconducting system has a genuine bandgap value, and the value of that exchange parameter can be determined using the self-consistent

Table 3.5: Static dielectric constant and bandgap of bulk SnS_2 and TM-doped semiconductor systems estimated using DDPBE0 functionals. Cr, Cu, Co and Zn-doped systems are metals. Bandgap values are in eV.

System		PBE0[1]	PBE0[2]	PBE0[3]	PBE0[4]	PBE0[5]	PBE0[6]	$PBE0^{one-run}$
Bulk-SnS_2	ϵ_∞	6.22	7.22	7.52	7.594	7.592	7.590	8.7
	E_g	2.830	2.052	2.063	2.064	2.060	2.061	1.83
Ti	ϵ_∞	5.24	6.52	7.14	7.41	7.54	7.54	9.84
	E_g	2.281	1.53	1.26	1.18	1.13	1.13	0.62
V	ϵ_∞	5.101	6.4	7.212	7.70	7.961	7.943	7.940
	E_g	0.512	0.0	0.0	0.0	0.0	0.0	0.0
Mn	ϵ_∞	5.811	7.210	7.830	8.201	7.920	7.960	7.12
	E_g	2.063	1.26	1.04	0.98	0.93	0.93	1.26
Fe	ϵ_∞	5.042	6.20	7.04	7.60	7.804	7.903	5.9
	E_g	1.582	0.932	0.642	0.461	0.090	0.090	1.09
Ni	ϵ_∞	6.643	8.832	9.491	10.4	10.601	10.600	12.56
	E_g	1.631	1.081	0.862	0.790	0.770	0.770	0.83

DDHF computation. Because the value of the exchange parameter is unknown, the inverse of the dielectric constant can be substituted for the exchange parameter value. The DDHF provide the ideal exchange value, which would otherwise be unknown.

3.3.5 DDHF calculations on bulk and monolayer doped systems

We began the hybrid functional computation with an initial guess of α=25%. We measured the dielectric constant and bandgap data once it reached self-consistency. In the next iteration, the mixing parameter is determined by $\alpha = \epsilon_\infty^{-1}$. This process is repeated until the dielectric constant and, as a result, the bandgap converges.

Table 3.6: Static dielectric constant and bandgap of monolayer SnS_2 and TM-doped semiconductor systems estimated using DDHSE06 functionals. Cu, Co and Zn-doped systems are metals. Bandgap values are in eV.

System		HSE^1	HSE^2	HSE^3	HSE^4	HSE^5	HSE^6	HSE^7	$HSE^{one-run}$
ML-SnS_2	ϵ_∞	7.21	9.04	9.310	9.421	9.453	9.450	9.450	9.09
	E_g	2.430	1.951	1.892	1.890	1.890	1.890	1.890	1.85
Ti	ϵ_∞	7.201	9.040	9.259	9.422	9.453	9.450	9.450	9.86
	E_g	1.80	1.311	1.191	1.183	1.172	1.170	1.170	1.05
V	ϵ_∞	8.40	13.682	29.60	30.990	31.050	31.050	31.050	30.19
	E_g	1.312	0.310	0.0	0.0	0.0	0.0	0.0	0.0
Cr	ϵ_∞	7.42	10.251	12.542	13.920	14.540	14.620	14.620	15.17
	E_g	1.720	0.661	0.382	0.280	0.0	0.0	0	0.0
Mn	ϵ_∞	8.190	10.420	11.041	11.662	11.770	11.831	11.831	11.38
	E_g	1.75	1.191	1.083	1.050	1.032	1.030	1.030	0.93
Fe	ϵ_∞	8.55	11.931	13.690	14.970	15.681	16.120	16.421	12.88
	E_g	1.50	0.672	0.451	0.380	0.350	0.331	0.311	0.02
Ni	ϵ_∞	9.50	11.730	12.100	12.142	12.181	12.181	12.181	11.37
	E_g	1.50	1.05	0.993	0.992	0.992	0.992	0.992	0.94

The convergence of the dielectric constant was checked with the kpoints and the number of bands. The converged bandgap values calculated using DD-HSE06 and DD-PBE0 are tabulated in Table 3.2 and Table 3.3 for bulk and monolayer systems, respectively. On the other hand, in one run calculations, we have taken $\alpha = \frac{1}{\epsilon_\infty^{PBE}}$.

The symmetry of the system is slightly altered by the doping of the TM-atom. In both the monolayer and bulk forms of the crystal, doping Ti, Cr, Mn, Ni, and Zn causes the system to transform into trigonal prismatic symmetry, with two sets of two-fold degenerate orbitals and one non-degenerate orbital. These orbitals are

named as e_1 ($d_{xy}/d_{x^2-y^2}$), e_2 (d_{yz}/d_{xz}) and a (d_{z^2}). The average values of the relaxed lattice parameters are a = b = 3.64 Å in monolayer, a = b = 3.65 Å and c = 5.48 Å

Table 3.7: Static dielectric constant and bandgap of monolayer SnS_2 and TM-doped semiconductor systems estimated using DDPBE0 functionals. Co and Zn-doped systems are metals. Bandgap values are in eV.

System		PBE0[1]	PBE0[2]	PBE0[3]	PBE0[4]	PBE0[5]	PBE0[6]	PBE0[7]	PBE0[8]	$PBE0^{one-run}$
ML-SnS_2	ϵ_∞	7.290	8.591	8.910	8.930	8.930	8.930	8.930	8.930	8.925
	E_g	3.11	2.38	2.24	2.230	2.230	2.230	2.230	2.230	2.11
Ti	ϵ_∞	6.041	7.421	7.710	7.840	7.881	7.921	7.921	7.921	9.07
	E_g	2.480	1.880	1.651	1.621	1.610	1.601	1.601	1.601	1.25
V	ϵ_∞	7.01	9.772	12.350	28.55	32.55	32.55	32.55	32.55	31.7
	E_g	1.751	0.872	0.483	0	0	0	0	0	0
Cr	ϵ_∞	5.950	7.491	8.632	9.441	9.990	10.280	11.761	11.220	13.09
	E_g	2.440	1.441	1.032	0.834	0.733	0.692	0.650	0.541	0.3
Mn	ϵ_∞	6.82	9.870	10.310	10.102	9.941	9.940	9.940	9.940	10.95
	E_g	2.43	1.301	1.360	1.352	1.344	1.341	1.341	1.341	1.1
Fe	ϵ_∞	7.14	9.620	11.031	11.762	12.710	12.742	12.740	12.740	27.6
	E_g	2.190	1.240	0.860	0.740	0.691	0.630	0.630	0.630	0.05
Ni	ϵ_∞	7.72	9.85	10.57	10.72	10.764	10.762	10.760	10.760	10.52
	E_g	2.220	1.482	1.310	1.282	1.273	1.270	1.270	1.270	1.11
Cu	ϵ_∞	11.17	31.82	32.7	32.7	32.7	32.7	32.7	32.7	32.7
	E_g	0.73	0	0	0	0	0	0	0	0

in bulk systems with impurity doping. The average bond length of the transition metal atom and the S-atom (d_{TM-S}) in transition metal-doped monolayer and bulk systems are 2.42 Å and 2.40 Å respectively. Whereas d_{TM-S} in monolayer and bulk pristine SnS_2 are 2.59 Å and 2.60 Å respectively. The shorter bond length of

the relaxed transition metal-doped systems in comparison with the pristine system is due to the larger difference in the average electronegativity value between the transition metal atom and S-atom (0.85) than the electronegativity difference between Sn atom and S-atom (0.62). V, Cr, Mn, and Fe-doped bulk-SnS_2 systems are (nearly) direct-gap semiconductors that begin at the Γ-point. Valence band edge is fixed at Γ-point in all of these systems, like the pristine bulk-SnS_2. However, the conduction band edge has migrated from L (pristine SnS_2) to Γ-point from pristine to all these doped systems. Because of the doping at the Sn-site, conduction band has higher contribution from the d-orbitals of the transition metal atom and less from the *s*-orbital of the Sn-atom in doped systems. The origin of the conduction band edge shifts from the *s*-orbital of the Sn-atom (pristine SnS_2) to the *d*-orbital of the transition metal atom. As a result, 25% transition metal-doping on SnS_2 crystal causes the switch from indirect to nearly direct gap semiconductor. As the atomic number of the transition metal increases among the semiconductors, the bandgap decreases. We can see the highest bandgap in Ti and least in the Ni-doped systems. This is due to the shifting of the valence band towards the Fermi level. The valence band shifting enhances as the strength of the *p*-*d* hybridization increases. In all these doped systems, the nature of the conduction band changes as the atomic number of transition metal atoms increases, but the band structure at the valence band is almost the same.

TM-doped bulk SnS_2 systems: Our short-range hybrid functional computation estimates an upper bound to the bandgap value of bulk SnS_2 as 2.35 eV. It converges to 1.68 eV. According to various experimental studies, the bandgap of bulk SnS_2 is found as 2.21-2.35 eV [145, 195, 199]. Even though our prediction of the bandgap is 1.68-2.35 eV (Table 3.2), the upper bound is matching with one of the experimental values. The experimental bandgaps of TiS_2 and SnS_2 are found in the range of bandgap values calculated using the DDHF. This ensures that the

DDHF are good enough to produce the bandgap range in which the experimental bandgap exists. This motivated us to perform DDHF calculations on other doped systems.

Both the HSE06 and PBE0 functionals revealed that Ti, V, Mn, Fe, and Ni-doped bulk SnS_2 systems are semiconductors with α=25%. The bandgap ranges estimated using short-range hybrid functionals for Ti, Mn, and Ni-doped systems are 0.61-1.58 eV, 0.51-1.36 eV and 0.47-0.91 eV, respectively, as shown in Table 3.2 which has the bandgap values corresponding to the initial guess of 25% exchange, converged with the dielectric constant and for the one-run calculation where $\alpha = \frac{1}{\epsilon^{PBE}}$. Apart from that, V and Fe-doped systems are semiconducting, with bandgaps of 1.05 eV and 0.9 eV as upper bounds, respectively. However, as we progressed through the self-consistent phases in the HSE06 calculations, V and Fe-doped systems converged towards the half-metallic nature with a magnetic moment of 1 μ_B and 2 μ_B respectively. PBE0 functionals shown in Table 3.2 produce slightly greater bandgap values than HSE06 functionals. Still, the nature of the system remains the same except for Fe-doped SnS_2, which preserves its semiconducting nature with a very tiny gap of 0.09 eV. The bandgap ranges calculated by the PBE0 functionals for Ti, V, Mn, Fe and Ni-doped bulk SnS_2 are 1.13-2.28 eV, 0.0-0.51 eV, 0.93-2.06 eV, 0.09-1.58 eV and 0.77-1.63 eV respectively.

Non-magnetic semiconductors have converged in Ti and Ni-doped systems. Ti-doped SnS_2 is synthesized experimentally [216] and found to be a semiconductor when the Ti concentration is below 30% [217]. Also, the GGA+U study predicts it as a semiconductor [218]. The semiconducting gap of 1.37 eV [219] and the GGA gap of 0.86 eV [219] in V-doped bulk SnS_2 were experimentally synthesized with 25% V concentration. When compared to the GGA gap, our HSE06 gap with 25% exchange gives an indirect bandgap of 1.05 eV, which is a better value. Semiconducting V-doped SnS_2 thin films are made by spray pyrolysis [220] with a 25% V

concentration. Under the DD-HSE06 and DD-PBE0 functionals, Cr-doping results in a half-metallic nature shown in bulk band structure Figure 3.7 (c). However, according to another DFT research, with low Cr content is a semiconductor [221]. Mn-doped SnS_2, converges out as a semiconductor with a magnetic moment of 3 μ_B. Under the HSE06 and PBE0 computations, Fe-doped SnS_2 is a semiconductor with 2 μ_B magnetic moment with 25% exchange. This is consistent with Fe-doped SnS_2 thin films produced experimentally [222]. Other DFT studies employing GGA+U [223, 221, 224] concur with the half-metal nature as we discovered in our inquiry after the system converges using DD-HSE06 which is shown in Table 3.2. Aside from that, Fe-doped SnS_2 polycrystalline samples were produced via a molten salt solid-state process with Fe concentrations of 0, 12.5, 25, and 37.5% for impedance and dielectric analysis, according to [225]. Co, Cu, and Zn-doped systems are metals in the bulk environment regardless of the DFT functionals. For effective oxygen evolution reaction electrocatalyst, Co-doped SnS_2 nanosheet arrays were successfully produced experimentally [226]. The Zn-doped SnS_2 nanostructures were produced, and it was discovered as semiconductors with Zn concentrations below 10% [227]. Figure 3.7 (a) to (i) show the electronic band structure of Ti to Zn-doped bulk SnS_2 systems using HSE06 functionals with 25% exchange. The static dielectric constant and bandgap values of semiconductor doped systems along with the pristine bulk SnS_2, estimated using dielectric dependent HSE06 and PBE0 functionals are listed in the Table 3.4 and 3.5, respectively.

TM-doped monolayer SnS_2 system: The experimental bandgap of monolayer SnS_2 is 2.29 eV [200]. This is in the range of 1.89-2.43 eV calculated by DD-HSE06 and 2.23-3.11 eV by DD-PBE0 (Table 3.3), which is in good agreement with the various theory works (Table 3.1). Our PBE0 functionals with an exchange of 11.6% gives a bandgap of 2.24 eV (Table) which is in good agreement with the experimental value. Also the HSE06 functionals with an exchange of 13.9% estimates a bandgap

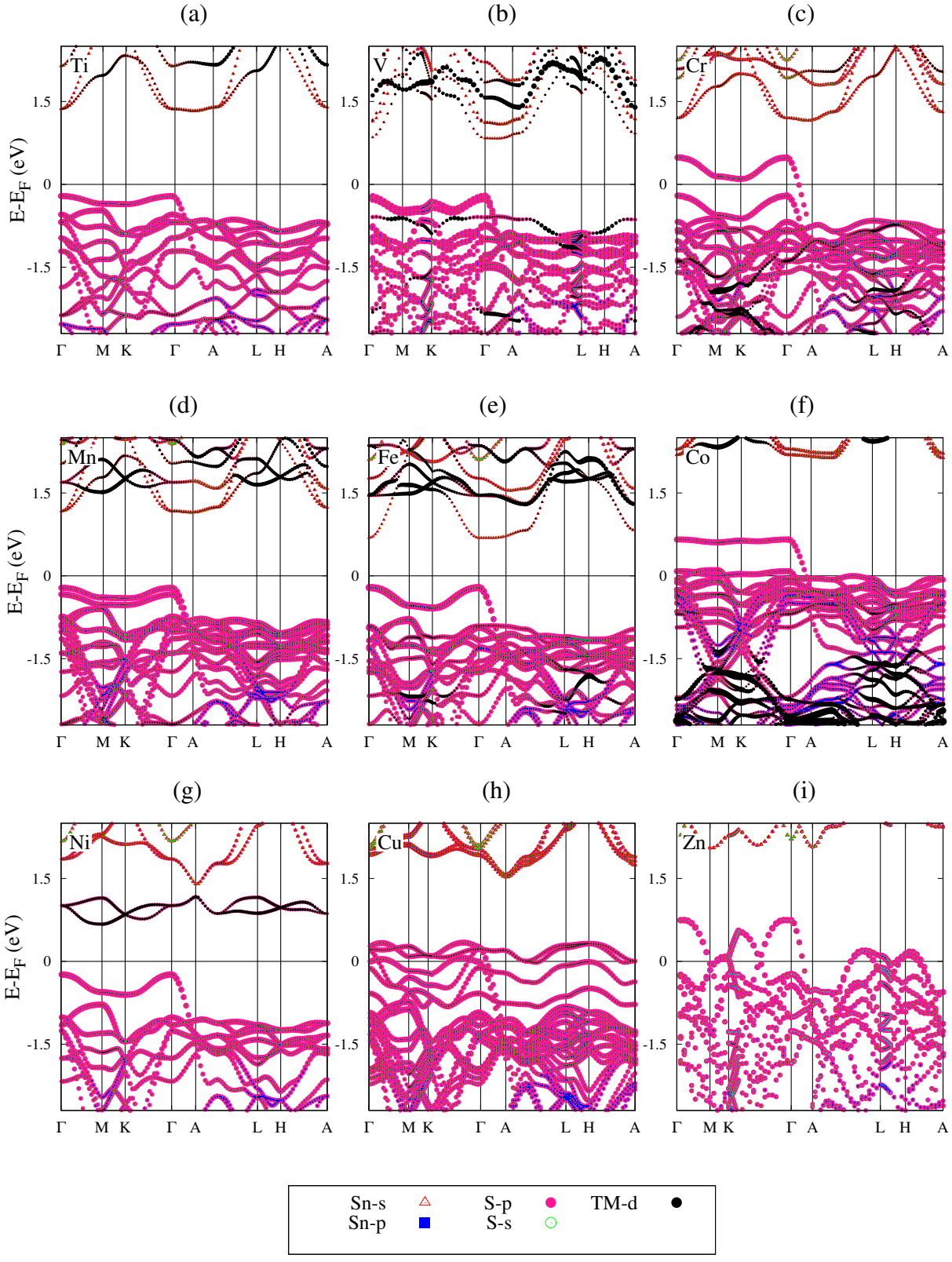

Figure 3.7: Orbital projected band structure of (a) Ti, (b) V, (c) Cr, (d) Mn, (e) Fe, (f) Co, (g) Ni, (h) Cu and (i) Zn-doped bulk SnS_2 calculated using HSE06 functionals with an exchange of 25%. Fermi energy is set to zero.

of 1.951 eV (Table 3.6). As per the dielectric-dependent HSE06 functionals Ti (1.17-1.8 eV, 0 μ_B), Mn (1.03-1.75 eV, 3 μ_B), Fe (0.31-1.50 eV, 2 μ_B) and Ni (0.99-1.50 eV, 0 μ_B)-doped monolayer SnS_2 are semiconductors. V (0.0-1.3 eV, 1 μ_B) and Cr (0.0-1.72 eV, 2 μ_B)-doped systems are semiconductors at the initial guess, and converged to half-metals. These bandgap values are listed in the Table 3.3. The PBE0 functionals reveal that Cr (0.54-2.44 eV, 2 μ_B)-doped system converges to semiconductor and Cu(0.73 eV, 0 μ_B)-doped system initially has a semiconducting nature and converges to half-metal.

Regardless of the DFT functionals used, Ti and Ni-doped systems converged into non-magnetic semiconductors in the bulk and monolayer phases. The same is stated in another DFT study [228]. Even though the V-doped system has a semiconductor nature with α=25%, the DD-HSE06 and DD-PBE0 computations converge to a half-metallic nature (Table 3.6 and 3.3.5). At 6.25% V concentration, a DFT study revealed that the V-doped SnS_2 monolayer is a semiconductor [228]. In a monolayer environment, a Cr-doped system is a semiconductor with α=25%, while it is half-metal in the bulk environment. Experimentally produced Cr-doped SnS_2 nanoflowers were found to be semiconductors [229]. Mn and Fe-doped systems converged during the monolayer phase to form magnetic semiconductors. Single crystals of Mn-doped SnS_2, which are semiconductors, were produced experimentally using the self-flux method [230]. The Fe-doped SnS_2 monolayer produced experimentally is a magnetic semiconductor [231]. Through strain engineering, the DFT investigation of Fe-doped monolayer SnS_2 is a half-metal [232] and Mn-doped monolayer SnS_2 is a semiconductor [233]. We discovered metallic nature in the Co and Zn-doped environment. The intercalated Co-SnS_2 and Cu-SnS_2 monolayers are metal and p-type semiconductors, respectively, according to the experiment [234]. When DD-PBE0 functionals are utilised with α=25% exchange, the Cu-doped system is found to be a semiconductor with a finite gap of 0.73 eV. Once

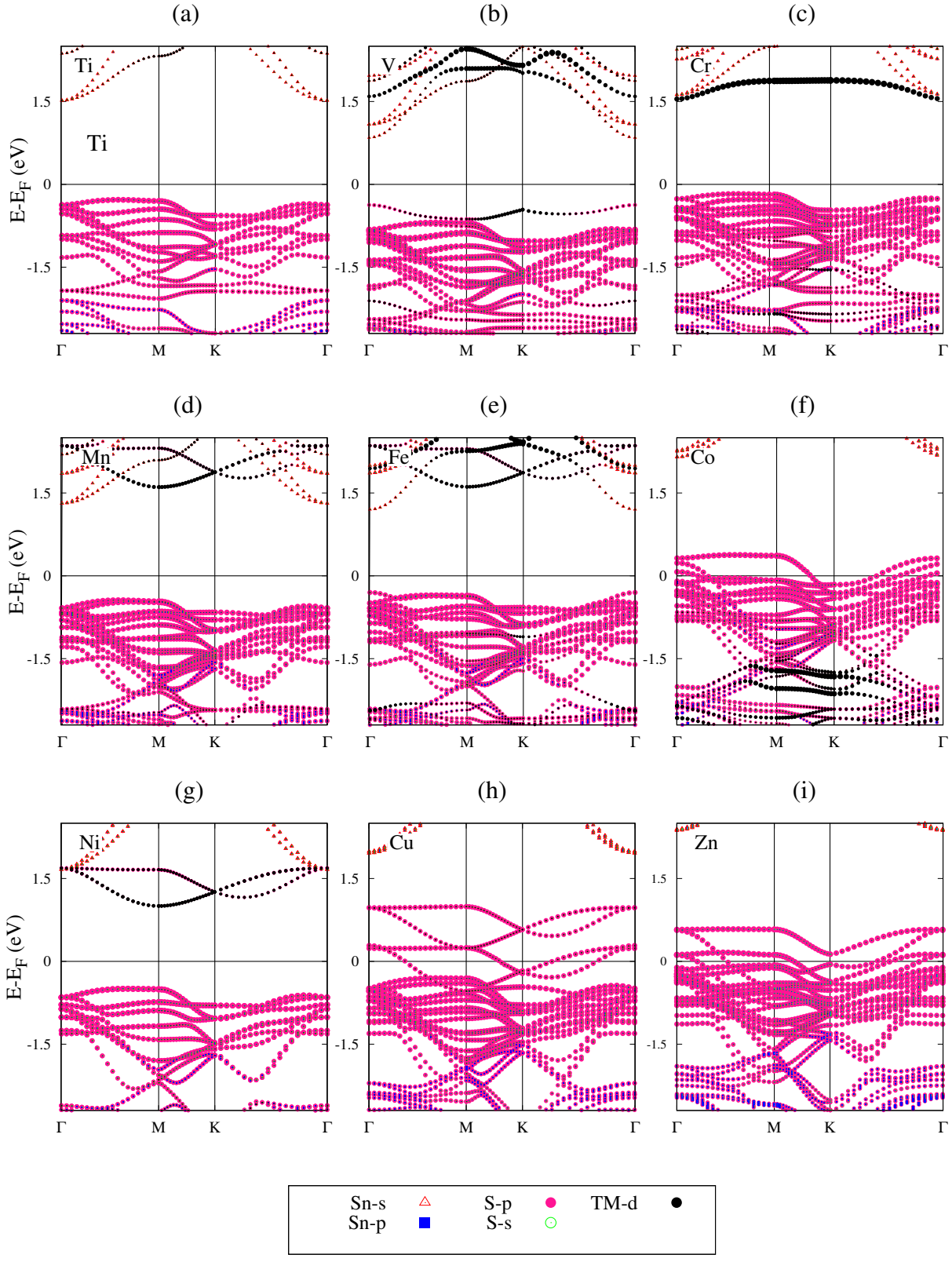

Figure 3.8: Orbital projected band structure of (a) Ti, (b) V, (c) Cr, (d) Mn, (e) Fe, (f) Co, (g) Ni, (h) Cu and (i) Zn-doped monolayer SnS_2 calculated using HSE06 functionals with an exchange of 25%. Fermi energy is set to zero.

the convergence is achieved, the system approaches half-metallic nature. Throughout the DD-HSE06 computation, it is a half-metal. Cu-doped SnS_2 nanoflakes were made using a hydrothermal technique, according to [235]. Zn-doped SnS_2 nanoflakes were synthesized and showed that the system turns semiconductor at very low Zn concentrations [236]. At low Zn concentrations, the DFT work on the Zn-doped SnS_2 monolayer also indicates it to be a semiconductor [190]. Figure 3.8 (a) to (i) show the electronic band structure of Ti to Zn-doped monolayer SnS_2 systems using HSE06 functionals with 25% exchange. The static dielectric constant and bandgap values of semiconductor doped systems along with the pristine monolayer SnS_2, estimated using dielectric dependent HSE06 and PBE0 functionals are listed in the Table 3.6 and 3.3.5, respectively.

3.4 Optical properties

The study of the optical properties of a photovoltaic absorber is important for building optoelectronic devices. Due to impurity, transition metal-doped systems have a smaller bandgap than pure SnS_2 (2.2-2.43 eV). According to the HSE06 band structure calculation with 25% exchange, the bandgap of bulk and monolayer doped systems vary within 0.9-1.58 eV and 1.5-1.8 eV, respectively. In these systems, V, Mn, and Fe-doped systems are nearly direct gap semiconductors in the bulk form. This is shown in the Figure 3.7 (b), (d) and (e). The optical properties we focus on are the absorption coefficient $\alpha(\omega)$, reflectivity R(ω), refractive index n(ω) and exciton binding energy. For the study, we use HSE06 functionals with 25% exchange. Optical constants have a dependence on the dielectric function $\varepsilon(\omega)$, which has a dependence on the frequency of the incident photon. To completely understand the optical properties, we need to calculate its dielectric

function $\varepsilon(\omega)$. The complex dielectric function is given by

$$\varepsilon(\omega) = \varepsilon_1(\omega) + i\varepsilon_2(\omega). \tag{3.31}$$

Here $\varepsilon_1(\omega)$ is the real and $\varepsilon_2(\omega)$ is the imaginary part of the dielectric function. The real part of the dielectric function is obtained by the Kramers Kronig transformation [190]. It is given by

$$\varepsilon_1(\omega) = \frac{2}{\pi} P \int_0^\infty \frac{\omega' \varepsilon_2(\omega') d\omega}{(\omega'^2 - \omega^2)}. \tag{3.32}$$

Where P denotes the principle value. The imaginary part of the dielectric function is determined by summation over empty states using the equation [237]

$$\varepsilon_2(\omega) = \left(\frac{4\pi^2 e^2}{m^2\omega^2}\right) \sum_{i,j} \int \langle i|M|j\rangle^2 f_i(1-f_i)(E_f - E_i - \omega) d^3k. \tag{3.33}$$

Here M is the dipole matrix, i and j are the initial and final states respectively, f_i is the Fermi distribution function for the ith state and E_i is the energy of electron in the ith state. The optical constants such as absorption coefficient $\alpha(\omega)$, reflectivity R(ω) and refractive index n(ω) can be calculated by the real $\varepsilon_1(\omega)$ and imaginary $\varepsilon_2(\omega)$ part of the dielectric functions [238, 239, 240]. They are given by

$$\alpha(\omega) = \sqrt{2}\omega \left[\sqrt{\varepsilon_1^2(\omega) + \varepsilon_2^2(\omega)} - \varepsilon_1(\omega)\right]^{1/2}, \tag{3.34}$$

$$n(\omega) = \frac{1}{\sqrt{2}} \left[\sqrt{\varepsilon_1^2(\omega) + \varepsilon_2^2(\omega)} + \varepsilon_1(\omega)\right]^{1/2}, \tag{3.35}$$

$$\kappa(\omega) = \frac{1}{\sqrt{2}} \left[\sqrt{\varepsilon_1^2(\omega) + \varepsilon_2^2(\omega)} - \varepsilon_1(\omega)\right]^{1/2}. \tag{3.36}$$

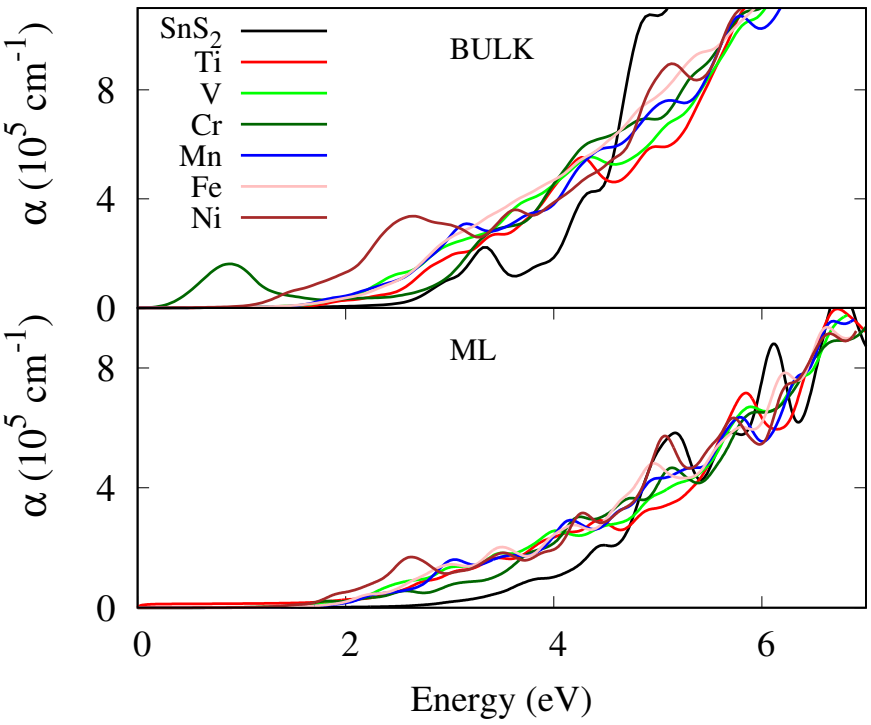

Figure 3.9: Optical absorption spectra of Ti, V, Cr, Mn, Fe and Ni-doped bulk and monolayer SnS_2 systems.

Here $\kappa(\omega)$ is the extinction coefficient, which gives reflectivity as

$$R(\omega) = \frac{(n-1)^2+\kappa^2}{(n+1)^2+\kappa^2}. \tag{3.37}$$

Bulk-SnS_2 crystal has an absorption peak at 3.35 eV with an absorption coefficient of $2.2 \times 10^4\,cm^{-1}$. In comparison to the monolayer-SnS_2, the bulk absorption spectra have shifted to the low-energy region. This might be due to the presence of several layers in the bulk system, which are stacked by Van der Waals interaction. The electrons in these layers undergo an interband transition from valence band maxima near Γ-point to conduction band minima at L-point. The indirect bandgap calculated using absorption spectra is 2.22 eV. For pure SnS_2, the first prominent peak in the entire energy region is located at 6.3 eV, and two small peaks are positioned at 3.35 eV and 4.36 eV. The higher intensity peaks are observed above 6.3

eV. This shows that more of the absorption occurs in the near-ultraviolet region. The absorption spectra of all the doped systems are shown in Figure 3.9 in comparison with the pristine SnS_2. This shows the redshift in the energy of all the transition metal-doped systems in comparison with the pristine SnS_2. This redshift is due to the mediation of impurity 3*d*-bands of the transition metal atoms near the Fermi level of the system. This can also be verified from the band structure calculations. In comparison with pure SnS_2, the absorption coefficient of the doped system has increased. Ni-doped system has the highest absorption in the lower energy range than the other doped systems. The behaviour of the Cr-doped system is different from other systems. It resembles free-electron absorption. This is because of the half-metallic nature of the Cr-doped system in the bulk form. However Cr-doped system in monolayer form is a semiconductor. It undergoes a transition from a bulk half-metallic system to a monolayer semiconductor when it is doped at 25% concentration. Co, Cu and Zn-doped systems also have metallic absorption. The metallic nature can be seen from the absorption at zero energy in Figure 3.11. All the transition metal-doped systems look similar in the (near) infrared region. From the absorption spectra with 25% dopant concentration, we can see the enhanced absorption coefficient. This shows that these systems have a higher tendency of light absorption in the near-ultraviolet region. Figure 3.11 shows the optical absorption in Co, Cu, and Zn-doped SnS_2 systems. We can also see how the concentration of dopant affects the absorption by using the example of the Fe-doped monolayer SnS_2. As the concentration of Fe in the SnS_2 crystal increases, the absorption peaks shift towards the low-energy region. In other words, the bandgap becomes narrower as the Fe-concentration increases (Figure 3.11).

The reflectivity (R) and refractivity index (n) spectra of SnS_2 and all the doped systems are presented in Figure 3.10. Both the spectra of the doped systems are enhanced below 3 eV energy which is highest in Ni-doped SnS_2 in comparison

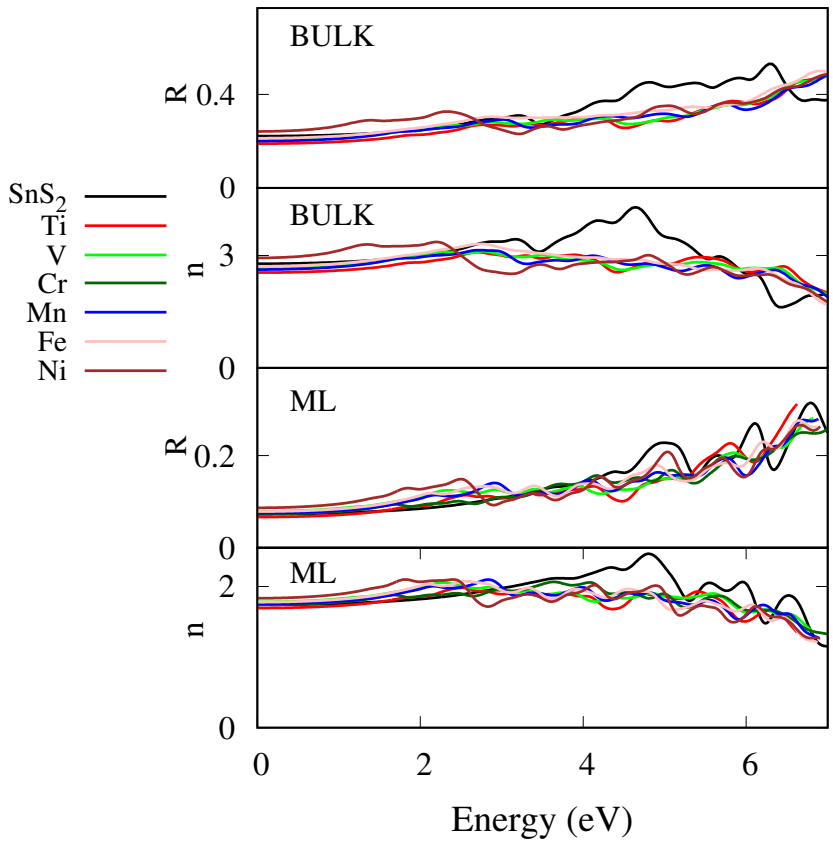

Figure 3.10: Reflectivity and refractivity spectra of Ti, V, Cr, Mn, Fe and Ni-doped bulk and monolayer SnS_2 systems.

with the pure SnS_2 crystal. Above 3 eV, reflectivity and refractivity of the doped systems are less enhanced in comparison with the pure SnS_2. We have seen the significant absorption of all these doped systems below 3 eV. Hence all these results together indicate that the optical properties are greatly improved in the low energy region.

3.4.1 Exciton binding energy

Excitons are the bound state of electrons and holes. Excitons play a vital role in the optical properties of the crystal. The behaviour of the excitons in a system purely depends on the electronic environment of the system. The bulk system is surrounded by a dielectric medium thoroughly from all three directions, and

hence the Coulomb interaction between electron and hole is well screened by the dielectric medium. In the case of a 2D system, the screening effect is reduced and is confined only to the 2D plane. On top of this, quantum confinement also adds to the dielectric confinement in the 2D system. Finally, these two confinement effects make the exciton to be tightly bound on 2D-plane rather than in the bulk environment of the system. This fact leads to higher binding energy in monolayer systems. Hence it is very important to understand the dielectric screening in 2D semiconductors or insulators. The dielectric screening can be measured using the screening length r_0. For a better understanding we adopted the theory described by other work [241], we imagine a 2D dielectric sheet embedded in a vacuum exposed to an external potential caused by a point charge placed at the origin. In the long-wavelength limit, the induced charge density is related to the 2D polarization P_{2D}. Then using Poissons equation, the total electrostatic potential generated by the point charge can be given by [241],

$$\nabla^2\phi(\mathbf{r}) = -4\pi e\delta(\mathbf{r}) - 4\pi\chi_{2D}\nabla^2\phi(\rho, z=0)\delta(z). \tag{3.38}$$

Then by using the Fourier transform, we can get the 2D macroscopic potential.

$$\phi_{2D}(\mathbf{q}) = \frac{2\pi e}{|q|(1+2\pi\chi_{2D}|q|)}. \tag{3.39}$$

Here q is the in-plane component of the wave vector, and the χ_{2D} is the 2D polarizability of the dielectric sheet. Here ϕ_{2D} describes the 2D macroscopic screening of a point charge. By considering the above expression of ϕ_{2D}, it is evident that the macroscopic dielectric screening has no connection with a simple dielectric constant, whereas that plays a role in 3D systems. Now by the inverse Fourier transform of the $e\phi_{2D}(q)$, one can determine the effective potential experienced by the electron in a dielectric 2D plane in the presence of a point charge. This was

originally derived by Keldysh [242]

$$V_{2D}(\mathbf{r}) = -\frac{e^2}{8\varepsilon_0\bar{\varepsilon}r_0}\left[H_0(\frac{r}{r_0}) - Y_0(\frac{r}{r_0})\right]. \tag{3.40}$$

Where H_0 and Y_0 are the Struve and the second kind of Bessel functions, respectively. We have $r_0 = 2\pi\chi_{2D}/\kappa_{eff}$, where κ_{eff} is the effective dielectric constant of the environment surrounding the 2D system. With χ_{2D} calculated using the relation $\varepsilon_{xy} = 1 + 4\pi\chi_{2D}/L$. Here ε_{xy} is the in-plane dielectric constant, and L is the thickness of the vacuum layer. From the expression of the 2D effective potential created by a point charge, we can understand that this potential depends on distance r, relative to r_0. The simplified potential given by Keldysh [242] when $r << r_0$ is

$$V_{2D}(r << r_0) \approx \frac{e^2}{4\pi\varepsilon_0\bar{\varepsilon}}\frac{1}{r_0}\left[ln(\frac{r}{2r_0}) + \gamma\right]. \tag{3.41}$$

Here γ is the Euler constant. When $r >> r_0$,

$$V_{2D}(r >> r_0) \approx -\frac{e^2}{4\varepsilon_0\bar{\varepsilon}}\frac{1}{r}. \tag{3.42}$$

One can notice the logarithmic potential like a line charge in the case of $r << r_0$ and in the case of $r >> r_0$ the potential varies like $\frac{1}{r}$ which is a standard electrostatic potential created by a point charge [243]. The combination of these two limits is expressed in a single equation by Cudazzo et al. [241], given by

$$V^C_{2D}(r << r_0) \approx \frac{e^2}{4\pi\varepsilon_0\bar{\varepsilon}}\frac{1}{r_0}\left[ln(\frac{r}{r+r_0}) + (\gamma - ln(2))e^{-\frac{r}{r_0}}\right]. \tag{3.43}$$

For a 2D system with anisotropic electron and hole, effective masses $m_x{}^e \neq m_y{}^e$ and $m_x{}^h \neq m_y{}^h$, the exciton wave function obtained using variational principle is given by [244]

$$\phi(x,y) = (\frac{2}{a_x^2\lambda\pi})^{1/2} exp\left[-\sqrt{(x/a_x)^2+(y/\lambda a_x)^2}\right]. \tag{3.44}$$

Here λ is the variational anisotropy scaling factor, a_x is the exciton extension along the x direction, λ and a_x are related by $a_y = \lambda a_x$. Using this variational wave function, the kinetic and potential energies of exciton are given by [243]. The expression for the kinetic energy is

$$E_{kin}(a_x,\lambda) = \frac{\hbar^2}{2}\int\int \phi\left[\frac{1}{\mu_x}\frac{\partial^2\phi}{\partial x^2}+\frac{1}{\mu_y}\frac{\partial^2\phi}{\partial y^2}\right]dxdy, \tag{3.45}$$

$$E_{kin}(a_x,\lambda) = \frac{\hbar^2}{4a_x^2}\left(\frac{1}{\mu_x}+\frac{1}{\lambda^2\mu_y}\right). \tag{3.46}$$

Here μ_x and μ_y are the reduced effective masses of the exciton along x and y-directions respectively, $\mu = m^e m^h/(m^e+m^h)$. The potential energy is given by

$$E_{pot}(a_x,\lambda) = \int\int V_{2D}(x,y)\phi(x,y)^2 dxdy. \tag{3.47}$$

Using the expected kinetic and potential energy of the exciton, its binding energy is expressed as

$$E_{X-2D}(a_x,\lambda) = E_{kin}+E_{pot}. \tag{3.48}$$

Where E_{X-2D} specifies the exciton binding energy in a 2D system and it is calculated using a code developed in the our research group. The detailed study of the exciton binding energy mentioned in [245] leads to running a Mathematic code to calculate E_{X-2D}. Using the above expression (3.48) formulated by the Wolfram

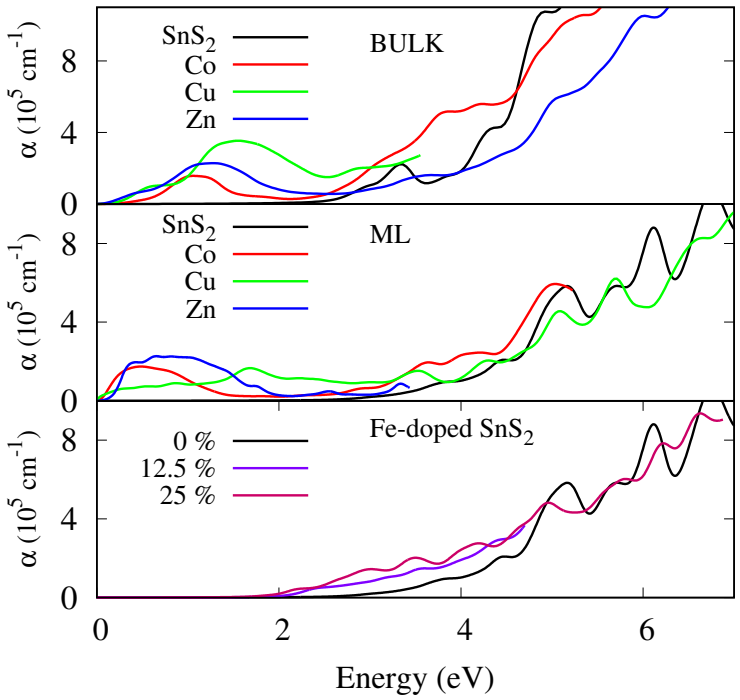

Figure 3.11: Absorption spectra of Co, Cu and Zn-doped SnS_2 in comparison with pure SnS_2 crystal in bulk and monolayer form. Absorption spectra of Fe doped monolayer SnS_2 for 12.5% and 25% concentration

Mathematica code of version 10.2.0 [246], we calculated the exciton binding energy of all the monolayer systems doped with TM-atoms. This requires the effective masses of the charge carriers along x, y-directions and the 2D polarizability χ_{2D}. The effective masses of charge carriers are calculated by fitting the HSE06 bands to the parabolic dispersion E(k) = $\frac{\hbar^2 k^2}{2m^*}$ using VASPKIT version 0.52 [247]. Let us consider the excitons in a 3D system. The dielectric screening is neglected while formulating the exciton binding energy in a 3D system. By using the effective mass theory of excitons developed by Velizhanin et al. [248] the 2D exciton binding energy is approximated to the 3D systems [59]. The exciton binding energy in the 3D system is given by [59]

$$E_{X-3D} = \frac{\mu^{3D} E_{Ryd}}{\kappa_B^2} \tag{3.49}$$

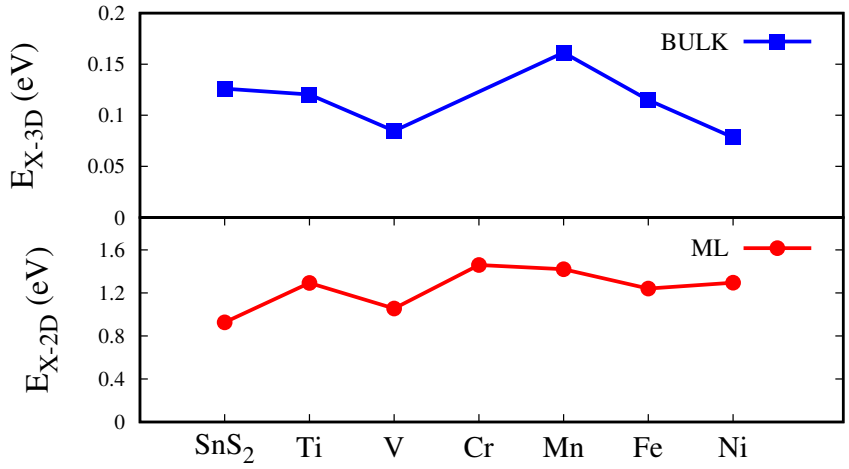

Figure 3.12: Exciton binding energy in TM-doped monolayer and bulk SnS_2 systems.

Table 3.8: Effective masses of electron $m_e^*(k_x)$, $m_e^*(k_y)$, $m_e^*(k_z)$ and hole $m_h^*(k_x)$, $m_h^*(k_y)$, $m_h^*(k_z)$ along x, y, z-directions for the bulk-SnS_2 and doped semiconductor systems. Also the reduced 3D effective mass, $\mu^{3D} = 3(\mu_x^-1 + \mu_y^-1 + \mu_z^-1)^{-1}$, the effective bulk dielectric constant κ_B and the exciton binding energy E_{X-3D} values are given. Here $\mu_i = (m_i^e m_i^h)/(m_i^e + m_i^h)$. Effective masses are in units of the electron rest mass.

System	$m_e^*(k_x)$	$m_e^*(k_y)$	$m_e^*(k_z)$	$m_h^*(k_x)$	$m_h^*(k_y)$	$m_h^*(k_z)$	μ_{3D}	κ_B	$E_{X-3D}(meV)$
BULK-SnS_2 [59]	1.104	0.375		0.424	2.542		0.345	5.85	137 112 (expt) [59]
Present work	1.095	0.398	1.221	0.422	2.460	2.10	0.398	6.56	126.2
Ti	0.476	0.419	1.14	3.269	3.269	0.239	0.295	5.79	120.3
V	0.314	0.325	4.032	0.458	0.337	1.043	0.238	6.19	84.72
Mn	0.909	0.612	3.194	1.355	7.38	2.405	0.394	5.77	161.3
Fe	3.142	0.508	0.304	0.792	0.496	7.263	0.375	6.68	114.9
Ni	0.64	1.024	4.464	2.13	1.795	0.239	0.376	8.09	78.31

Here $\mu^{3D} = 3(\mu_x^-1 + \mu_y^-1 + \mu_z^-1)^{-1}$, $\mu_i = (m_i^e m_i^h)/(m_i^e + m_i^h)$ and κ_B is the effective bulk dielectric constant calculated using the bulk dielectric tensor. The expression

Table 3.9: Effective masses of electron $m_e^*(k_x)$, $m_e^*(k_y)$ and hole $m_h^*(k_x)$, $m_h^*(k_y)$ along x and y-directions for the monolayer-SnS_2 and doped semiconductor systems. Also the reduced 2D polarizability χ_{2D} and the exciton binding energy E_{X-2D} values are given. Effective masses are in units of the electron rest mass.

	System	$m_e^*(k_x)$	$m_e^*(k_y)$	$m_h^*(k_x)$	$m_h^*(k_y)$	χ_{2D}(Å)	$E_{X-2D}(eV)$
ML-SnS_2	[59]	0.342	0.815		0.342	2.266	0.912
	Present work	0.340	0.810	0.335	2.272	2.28	0.926
	Ti	0.869	0.663	0.60	0.436	2.11	1.293
	V	0.658	0.346	2.486	0.112	2.03	1.055
	Cr	0.638	0.682	2.609	0.407	1.88	1.46
	Mn	0.526	0.657	1.988	0.450	2.04	1.42
	Fe	0.277	0.483	0.426	2.134	2.18	1.24
	Ni	0.740	0.895	2.127	0.384	2.3	1.295

is given by $\kappa_B = \sqrt{\varepsilon_z \varepsilon_{xy}}$, with ε_z and ε_{xy} are the transverse and in-plane component of the bulk dielectric tensor.

We computed the dielectric tensor by using HSE06 functionals. Using the above formula (3.49), we calculated the exciton binding energy of the bulk SnS_2 crystal as 126.2 meV, which is near to the calculated value by other theory work [59](137 meV). Also, it is in good agreement with the experimental work [249](112 meV). Table 3.8 and 3.9 provide the exciton binding energy of all the bulk and monolayer doped SnS_2 systems along with the required parameters. The calculated value of E_{X-2D} for the pristine monolayer-SnS_2 is 0.926 eV which is in good agreement with the other theory value [59](0.912 eV). The variation in the exciton binding energy after doping with the transition metal atoms is mainly due to the involvement of the localized 3*d*-orbitals, which are absent in the pristine system. These 3*d*-orbitals change the hybridization between the host and chalcogen atom. Thus changing the extrema positions. This affects the curvature of the electron path in the valence and conduction band. Since the curvature of the electron has an inverse dependence on

its effective mass, exciton binding energy changes accordingly. The plot in Figure 3.12 shows, in the case of bulk doped systems Mn-doped system has the highest exciton binding energy of 161 meV. To our knowledge, this large exciton binding energy is because of the higher reduced effective exciton mass due to the flat band near the Fermi level. This can be seen in the Mn-band structure in Figure 3.7 (d). This flat valence band is due to the p_z-orbital of S and d_{z^2} orbital of Mn-atom. Also, note that, it has a lower value of bulk dielectric constant (5.77) than other systems. Further, the flatness of this band is more towards Γ to M path, and hence the hole mass is heavier (7.38 m_0) along the x-direction. The electron mass in the conduction band is lighter than the hole mass, as shown in the band structure in Figure 3.7 (d), which has more curvature than the flat valence band. Secondly, Ti and Fe-doped systems also have larger binding energies of 120.3 meV and 114.9 meV, respectively. In this case, it is mainly because of the effective mass of the carriers.

In the Fe-doped system, the spin-up hole has heavier mass along the y-direction due to a flat curve along Γ to M path. This valence band just below the Fermi level is mainly due to p_z-orbital of S-atom and d-orbitals of Fe-atom. The same trend holds for the Ti-doped system. The valence band is flatter than that of the Fe-doped system. In the conduction band, the path along Γ to A has heavier electron because the corresponding band has more contribution from the localized $d_{xy}/d_{x^2-y^2}$ and d_{xz}/d_{yz} orbitals of Ti-atom with very less s-orbital contribution from Sn-atom. This implies a heavier electron along the z-direction. These observations can be seen in Ti and Fe-doped systems' band structure in Figure 3.7 (a) and (e). In the case of V and Ni-doped systems, the charge carriers possess lighter effective masses along x, and y-directions, though the electron has a heavier mass along the z-direction. Their bulk dielectric constants are higher compared to other systems. These two factors compensate and result in smaller exciton binding energy in Ti and V-doped

systems. Figure 3.12 shows the comparison between the exciton binding energy of all of the transition metal-doped semiconducting systems in bulk and monolayer environment. Among these systems, exciton binding energy is larger in the monolayer than in the bulk environment.

3.5 Conclusion

In conclusion, we have systematically studied the electronic bandgap and optical properties of all the 3*d*-series transition metal-doped SnS_2 crystal both in the bulk and monolayer form. Calculation of the formation energies shows that the Sn-poor (S-rich) condition is the favourable condition to incorporate the TM-atom into SnS_2 crystal at Sn-site. The dielectric-dependent hybrid functionals calculations have predicted the experimentally matchable bandgaps for TiS_2 and SnS_2 crystals. Using the dielectric-dependent HSE06 and PBE0 hybrid functionals, we have calculated the range of bandgap values for all the doped systems in bulk and monolayer environment. The converged bandgap is calculated at the level of the converged dielectric constant. The calculated range of bandgap values using DDHF give the lower and upper bound to the true bandgap of the system. Possible experimental gaps are expected within this range. This helps us to determine the application perspectives of the transition metal-doped systems.

The absorption spectra reveal the redshift in the energy of all the doped systems. V, Mn and Fe-doped systems are nearly direct bandgap semiconductors and exhibit higher absorption coefficients in the bulk environment. These are suitable optical absorber materials for optoelectronic devices. Cr doped bulk SnS_2 is a half-metal that is good for spin-injector materials. The absorption coefficient, reflectivity and refractivity of all the doped systems are enhanced in the low energy region. Thus, our calculations support the effective use of solar energy. Semiconductors

with a monolayer environment show higher exciton binding energy than in the bulk environment. These results emphasize the importance of transition metal doping on SnS_2 crystal for optoelectronic device applications.

CHAPTER 4

TUNING THE MAGNETIC PROPERTIES OF MONOLAYER SNS_2 BY 3*D* TRANSITION METAL DOPING

In this chapter, we systematically study the electronic and magnetic properties of 3*d* transition metal atom-doped monolayer SnS_2. The spin-polarized First-principles calculations reveal that Sn-poor condition is the energetically favourable condition to substitute all the 3*d* transition metal atoms into SnS_2 monolayer at the Sn-site. We observe that, in all the doped systems, the denser valence bands are filled with the hybridized impurity 3*d* and S-3*p* orbitals. Here we show that, Sc-doped SnS_2 is a nonmagnetic metal, and Ti and Ni-doped systems are nonmagnetic semiconductors. Single V, Cr, Mn, Fe, Co, Cu, and Zn atom doped systems with a dopant concentration of 6.25% are semiconductors with an induced magnetic moment of 1, 2, 3, 2, 1, 0.688, and 1.275 μ_B, respectively. Among them, Cu and Zn-doped systems are direct bandgap semiconductors. With a dopant concentration of 4.08%, the double Fe and Co-doped SnS_2 monolayers are ferromagnetic half metals with 4 and 2 μ_B, respectively. The double V, Cr, Mn and Zn-doped SnS_2 are ferromagnetic semiconductors with 2, 4, 6 and 2.56 μ_B, respectively. These results emphasize the importance of 3*d* transition metal doped monolayer SnS_2 for spin injection, spin polarized current generation and other spintronics device applications. The above findings have been published in Materials Today Communications 33, 104626 (2022) [250].

4.1 Introduction

In recent years, spintronic devices have attracted researchers due to their advantages over electronic devices. They have low power consumption because of less Joule-heating effect, non-volatility, less heat dissipation, and greater processing speed compared to their electronic counterparts. However, utilizing the unpaired electrons which give the spin and manipulating the spins are the biggest challenges in these devices. Therefore tremendous attempts have been made in search of materials suitable for spintronic devices. Two-dimensional (2D) materials have attracted a great deal of attention. Among them, metal monochalcogenides [251] (MX-type, where M = Sn, Ge and X = S, Se, Te) and transition metal dichalcogenides [126, 127, 128, 129, 130, 131, 132, 133, 134, 135] (MX_2-type, where M = Ti, Hf, Zr and X = S, Se, Te) are extensively studied and utilized in electronic and optoelectronic devices. With all these materials the transition metal dichalcogenides MoS_2 [136, 137, 138, 139], WS_2 [140, 141], WSe_2 [142, 143], and NbS_2 [144], are promising materials due to their applications in electrical, optical, and magnetic fields. All of these layered materials show semiconducting nature. The semiconductors that we have studied till date are almost of nonmagnetic behaviour. The lack of unpaired electrons in all these semiconductors, such as graphene, phosphorene, transition metal dichalcogenides (TMDCs), metal dichalcogenides and metal monochalcogenides restrict them for spintronic device applications. One can utilize these purely diamagnetic semiconductors for the spintronic purpose by inducing magnetic moment. Defects induce the magnetism in graphene [252]. It can also be made magnetic by single vacancy defect [253], by hydrogination [254], flourination [255, 256] and by TM doping [257]. Phosphorene becomes magnetic with a single vacancy defects [258] and also with TM doping [259]. TMDCs namely MoS_2 [260], $MoSe_2$ [261], WS_2 [262] and WSe_2 [263] all become magnetic with TM

doping at the metal site.

Here we consider a layered metal dichalcogenide, namely SnS_2 as a host material. It originates from the MX_2 or CdI_2 crystal type [145]. Earth abundance and non-toxic nature of SnS_2 makes it as an environmental healthy and friendly material. Thus it is also a promising candidate for electronic devices. It is non-flammable, inexpensive, as well as impervious to water and air. Monolayer (ML) SnS_2 is a semiconductor with an indirect bandgap of 2.43 eV. Having an abandance of visible-light photocatalyst [74], makes SnS_2 as an excellent electrode material for Li-ion batteries [81, 82], gas sensors [83], and field emitters [84]. A complete solar cell model was constructed [146] using SnS_2. With a high on/off ratio exceeding 2×10^6 and a carrier mobility of $\sim$1 $cm^2\,V^{-1}\,s^{-1}$ [85], nano-membranes of SnS_2 are able to demonstrate high FET performance. An integrated logic circuit based on a high-performance top-gated field-effect transistor was fabricated [86] using SnS_2 monolayer. The electronic and optoelectronic properties of SnS_2, along with the photocatalytic [74, 82, 83, 84] properties, have been studied extensively. These properties show that SnS_2 is a good candidate for future electronic, nanoelectronic and optoelectronic basis material. As a nonmagnetic semiconductor, SnS_2 has limited applicability in spintronic devices. Therefore inducing the magnetism into SnS_2 is necessary to utilize it for the spintronic device applications. Inspired by the magnetism induced $SnSe_2$ [264], $HfSe_2$ [154], $ZrSe_2$ [265], via 3*d* TM doping, we use the density functional theory (DFT) calculations to study the induced magnetism in TM substituted SnS_2 monolayer. Here the TM atoms Sc, Ti, V, Cr, Mn, Fe, Co, Ni, Cu and Zn are substituted at the Sn-site in the SnS_2 crystal. The electronic properties of SnS_2 monolayer vary with the TM doping. In this article, we have studied the structural, electronic and magnetic properties of single and double TM doped SnS_2 monolayer. The formation energy calculations are performed by considering the Sn-poor and Sn-rich conditions. The spin-polarized band struc-

ture and density of states calculations are done using Heyd-Scuseria-Ernzerhof (HSE06) [266, 267, 112] hybrid density functionals of DFT. To comprehend the formation of the local magnetic moment, a single TM atom is doped in a smaller supercell of size $4\times4\times1$. For double TM atom doping in order to better understand the magnetic interaction and magnetic ordering between the two TM atoms, a larger supercell of size $7\times7\times1$ is employed.

4.2 Computational Details

First-principles calculations [179] are performed by using Vienna *ab initio* Simulation Package(VASP) [180]. The electron-ion interactions in these calculations were carried by projector augmented wave (PAW) [182, 183] pseudopotentials. A supercell of size $4\times4\times1$ is considered, and it is fully relaxed using Perdew, Burke, and Enzerhof (PBE) Generalized Gradient Approximation (GGA) [109] to calculate the ground state lattice parameters. Each transition metal (TM) atom replaces one of the Sn atoms. Each dopant atom has a 6.25 % concentration. While doing the calculations, atomic positions are optimized using the conjugate-gradient method with a force convergence criterion of 10^{-3} eV/Å and a tight energy convergence criterion of 1×10^{-6} eV. Cutoff energy of 400 eV is used. The thickness of the vacuum layer along the z-direction is relaxed to 20 Å. The Brillouin zone sampling was employed by Monkhorst-Pack [186] k-grid of size $21\times21\times1$ for pristine SnS_2 unit cell and $9\times9\times1$ for $4\times4\times1$ cell. All the TM doped systems are relaxed using spin-polarized PBE functionals. The spin-polarized band structure and density of states (DOS) are studied using HSE06 functionals. A supercell of size $7\times7\times1$ is used to determine the magnetic ordering in V, Cr, Mn, Fe, Co, Cu, and Zn-doped SnS_2 systems. Two identical TM atoms replace the two Sn atoms in this cell. Now the dopant concentration becomes 4.08 %. In this relaxation Monkhorst-Pack [186]

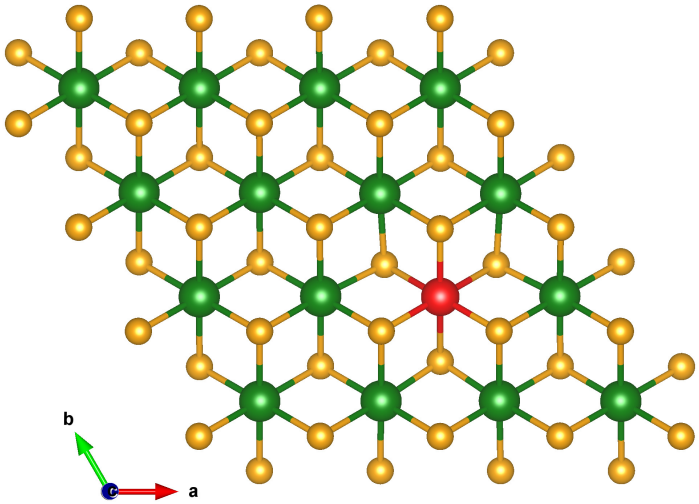

Figure 4.1: Top view of 4×4×1 cell of SnS_2 crystal doped with transition metal atom. Green, yellow and red balls represent Sn, S and transition metal atom respectively.

k-grid of size 5×5×1 is used to calculate the magnetic ground state.

4.3 Results and discussion

4.3.1 Formation energy of single TM doped ML-SnS_2

It is necessary to calculate the formation energy of every TM doped SnS_2 monolayer for studying the stability of the systems. TM atom is substituted at the Sn-site. The formation energy of the TM doped systems is calculated using the relation [189, 190, 268],

$$E_{form} = E_{doped} - E_{pristine} - n\mu_{TM} + n\mu_{Sn}. \tag{4.1}$$

Table 4.1: The bond length of S with TM atom d_{TM} and formation energy of TM doped monolayer SnS_2 systems at Sn-rich and Sn-poor conditions are given.

System	d_{TM} (Å)	E_{form} Sn-rich (eV)	E_{form} Sn-poor (eV)
SnS_2	2.596	-	-
Sc	2.608	-0.925	-1.874
Ti	2.500	-2.354	-3.303
V	2.438	-0.388	-1.337
Cr	2.411	0.292	-0.657
Mn	2.396	-1.026	-1.975
Fe	2.347	0.359	-0.590
Co	2.312	0.994	0.045
Ni	2.327	0.413	-0.536
Cu	2.428	2.575	1.626
Zn	2.519	2.461	1.512

Here E_{doped} and $E_{pristine}$ are the energies of transition metal-doped and pristine systems respectively. n is the number of Sn atoms replaced with transition metal atom. μ_{TM} and μ_{Sn} are the chemical potentials of the transition metal and Sn-atom, respectively. The formation energy of ML-SnS_2 is found to be -0.95 eV/atom. Several thermodynamic constraints are applied to the chemical potentials to avoid the formation of elemental phases (Sn, S and TM atom) and the secondary phases by TM atom with S-atom [191]. Since SnS_2 has two-type of atoms Sn and S, we need to find the formation energies both in Sn-rich (S-poor) and Sn-poor (S-rich) conditions. These conditions are based on the chemical potentials of the individual atoms. The detailed calculation for the formation energy is explained in([291]) Chapter 3. In Sn-rich and Sn-poor conditions μ_{Sn} is given by [192],

$$\mu_{Sn}^{Sn-rich} = \mu_{Sn,bulk},, \tag{4.2}$$

$$\mu_{Sn}^{Sn-poor} = \mu_{Sn,bulk} + \Delta E_f(SnS_2). \tag{4.3}$$

The formation energy of ML-SnS_2 is found to be -0.95 eV/atom. Table 4.1 shows the formation energy of TM doped SnS_2 monolayer in both the Sn-rich and Sn-poor conditions and the bond length of transition metal with S-atom. The formation energy values are lower in the Sn-poor (S-rich) condition than in the Sn-rich (S-poor) condition. Hence Sn-poor condition is the energetically favourable growth condition to substitute the Ti, V, Cr, Mn, Fe, Co, Ni, Cu and Zn atoms into SnS_2 monolayer at the Sn-site. Under the Sn-poor condition, the formation energy values for all dopants are negative with the exception of Co, Cu, and Zn-doped ML-SnS_2. A negative formation energy shows stable doped system. As a result, substitutional doping is employed to model the doping of Sn sites with transition metal atoms.

4.3.2 Binding energy of double TM doped ML-SnS_2

In order to understand the interaction between the two TM atoms at two different Sn-sites and hence to determine the magnetic ordering in the ML-SnS_2 systems, we have considered a bigger supercell of size 7×7×1. The binding energy of two TM atoms on two different Sn-sites in ML-SnS_2 has been calculated before we proceed with the double TM doping. It represents whether the two TM dopants prefer to stay together at two different Sn-sites or they prefer to dissociate into individual dopants. After studying the binding energy of TM doped 2D crystals [269, 270, 271], the binding energy of double TM doped ML-SnS_2 system is defined as

$$E_b = E_{\mathrm{TM-SnS_2}} - E_{\mathrm{SnS_2}} - 2E_{TM} + 2E_{Sn}. \tag{4.4}$$

Where E_b, $E_{\mathrm{TM-SnS_2}}$ and $E_{\mathrm{SnS_2}}$ are the binding energy, total energy of relaxed SnS_2 supercell of size 7×7×1 with two TM atoms and without TM atoms. E_{TM} and E_{Sn} are the energy of isolated TM atom and Sn atom, respectively. As the two TM atoms are doped at two Sn-sites their energies are multiplied by two. Binding

Table 4.2: The binding energy E_b of double TM atom doped monolayer SnS_2 systems.

System	E_b (eV)
V	-5.399
Cr	-1.381
Mn	-1.606
Fe	-1.629
Co	-0.721
Cu	-0.941
Zn	-0.521

energies are calculated only for systems wherein the TM atom induces magnetism and helps to study the magnetic interactions. The E_b values are listed in the Table 4.2. Here E_b ranges from -5.399 eV to -0.521 eV, indicates double V, Cr, Mn, Fe, Co, Cu and Zn atoms prefer to remain together at two different Sn-sites in ML-SnS_2.

4.3.3 Electronic property

Monolayer SnS_2 has hexagonal crystal structure with the space group of $P\bar{3}m1$ [59, 197, 58] belongs to MX_2 or CdI_2 crystal family. The top view of 4×4×1 cell of TM doped SnS_2 monolayer is shown in Figure 4.1. The six sulfur ligand field octahedrally surrounds the central Sn-atom with Sn-S bond length of 2.59 Å. The in-plane lattice parameter is 3.68 Å. The calculated bond length and lattice parameters are exactly matching with the theoretical work [196] using PBE functional. Each S atom is bonded to three Sn atoms. The HSE06 bandstructure of pristine ML-SnS_2 is shown in Figure 4.2 (a). It is a nonmagnetic semiconductor with an indirect bandgap of 2.43 eV. This is comparable with the other theoretical works shown in Table 4.3. The direct gap calculated at the M-point using HSE06 band structure is 2.64 eV. The experimental bandgap is 2.29 eV [200]. The valence band edge originates near Γ-point (Γ′) from the S-p_x,p_y and Sn-p_x,p_y orbitals, whereas

Table 4.3: Bandgap of ML-SnS_2 calculated using different DFT functionals.

System	E_g^{indirect} [Γ′-M](eV)	E_g^{direct} [M](eV)
PBE	1.45	1.69
HSE06	2.43	2.64
	(2.41) [59]	(2.68) [59]

conduction band edge originates at M-point from the Sn-*s* and S-p_x orbitals. The valence bands near Fermi level are mainly influenced by S-p_x,p_y orbitals and Sn-p_x,p_y orbitals. The conduction bands near the Fermi level have very high contribution from the Sn-*s* orbital and very less by the Sn and S-p_x,p_y orbitals.

Figure 4.2 (b) to (k) show the spin-polarized HSE06 band structures of Sc, Ti, V, Cr, Mn, Fe, Co, Ni, Cu, and Zn-doped ML-SnS_2 systems. Blue and red curves represent the spin-up and spin-down states. Except for Sc-doped SnS_2, all other doped systems are semiconductors. Sc-doped system is a nonmagnetic metal, and Ti and Ni-doped systems are nonmagnetic semiconductors. Their band structures involve only blue curves like pristine SnS_2. V, Cr, Mn, Fe, Co, Cu, and Zn-doped SnS_2 are semiconductors with finite magnetic moments. In their case, the band structure has well-separated spin-up (blue) and spin-down (red) states. The bandgap of all the doped systems varies between 0.69 to 2.17 eV, and it is below the pristine SnS_2 bandgap. Figure 4.3 clearly shows the total magnetic moment values, fundamental bandgap values along with the bandgaps of spin-up and spin-down states for all the TM doped systems. The Ti and Mn-doped systems have the highest bandgap of 2.17 eV, and the Zn-doped system has the lowest bandgap of 0.69 eV. In all these cases valence bands section is denser than the conduction bands section. Also, all the doped systems have denser valence bands section in comparison with the pris-

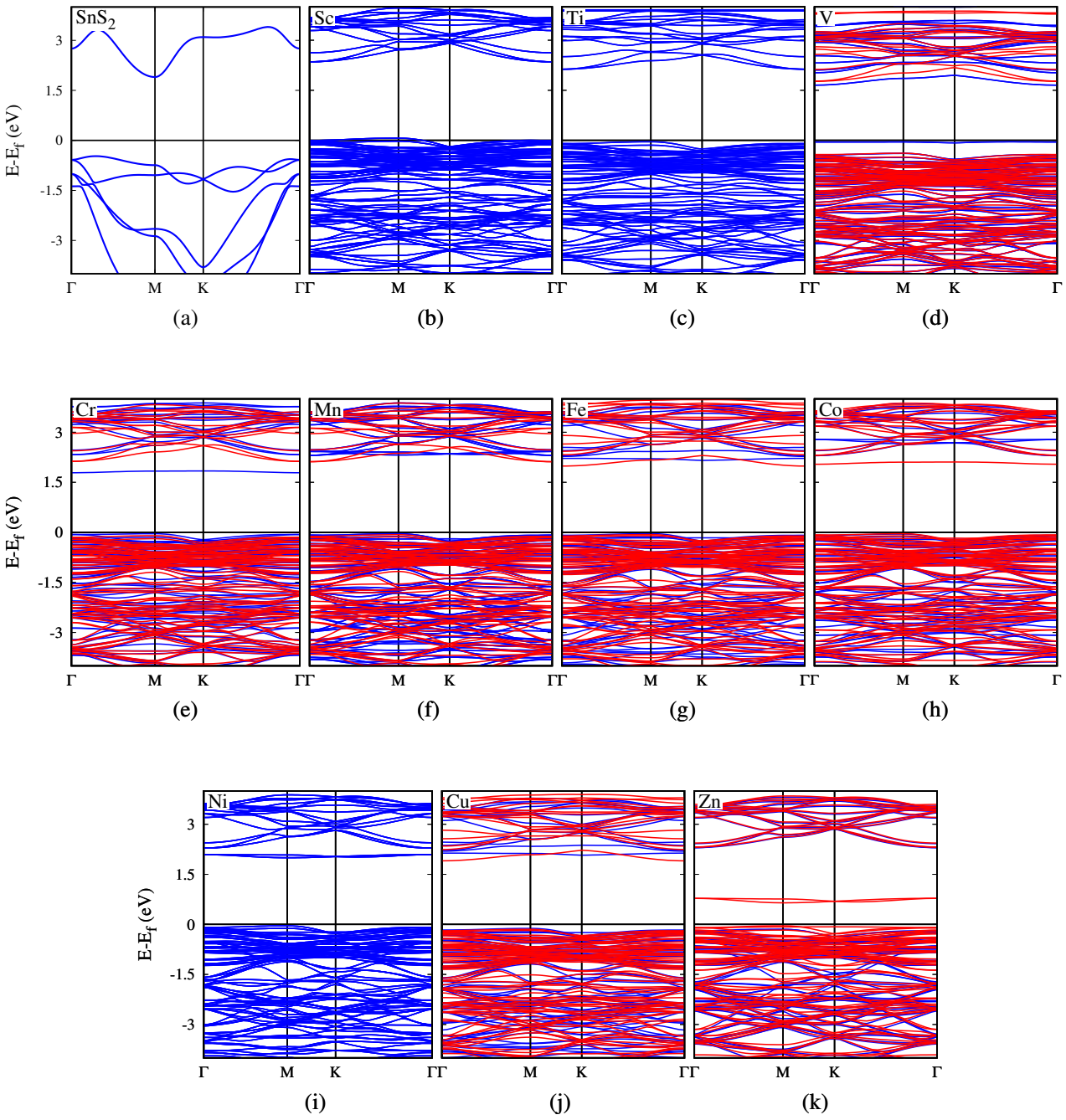

Figure 4.2: Spin-polarized bandstructure of (a) pristine SnS_2, and (b) Sc, (c) Ti, (d) V, (e) Cr, (f) Mn, (g) Fe, (h) Co, (i) Ni, (j) Cu, and (k) Zn-doped monolayer SnS_2 calculated using HSE06 functionals. Blue and red lines represent the spin-up and spin-down states. Fermi energy is set to zero.

tine SnS_2. Valence band near the Fermi level of pristine SnS_2 is mainly influenced by S-p_x,p_y and Sn-p_x,p_y orbitals. When the TM atom is substituted at the Sn-site, *d* orbitals play the role of Sn-p_x,p_y orbitals. The valence bands section of pristine SnS_2 is filled with the hybridized Sn-*p* and S-*p* orbitals. But the TM atom doping changes this hybridization in the valence bands section to S-*p* and TM-*d* orbitals, making the valence band denser. The impurity 3*d* states are observed in the conduction bands section of the pristine SnS_2 bands. In the pristine SnS_2, the indirect transition arises from Γ′ (VBM) to M-point (CBM). After substituting Ti, Cr, Mn, Fe, Co, and Cu atoms to SnS_2 systems, the indirect transition occurs from the valence band edge at M-point to the conduction band edge at Γ-point. In the case of a V-doped system, the valence band edge arises near K-point, and the conduction band edge is at Γ-point. Monolayers of Ni and Zn-doped SnS_2 undergo a direct transition at M-point (Figure 4.2 (i) and (k)).

4.3.4 Magnetism in single TM atom doped ML-SnS_2

Ti, Cr, Mn, Co, Ni, and Zn-doped systems exhibit trigonal prismatic symmetry with the two sets of two-fold degenerate orbitals and one nondegenerate orbital. These orbitals are named as e_1-$d_{xy}/d_{x^2-y^2}$, e_2-d_{yz}/d_{xz} and a_1-d_{z^2}. This kind of degeneracy is not observed in the case of V, Fe, and Cu-doped systems. The observations reveal the similarity in the electron filling in the impurity *d*-orbitals of Ti, Cr, Mn, Co, Ni, and Zn-doped ML-SnS_2. In all these systems electron fills the a_1 (d_{z^2}) orbital first and then e_1 and e_2 orbitals. Pristine SnS_2 is a purely diamagnetic system. The Sn-site is substituted with the 3*d* transition metal atoms. The Sn($5s^2 5p^2$) orbitals form bonds with S-atom. When it is substituted by the TM atom, the impurity 3*d* orbitals will participate in the bonding. The remaining 3*d* electrons occupy the nonbonding orbitals. Once after participated in bonding with the Sn-atom ($5s^2 5p^2$) the transition metal atoms Sc($3d^1 4s^2$), Ti($3d^2 4s^2$),

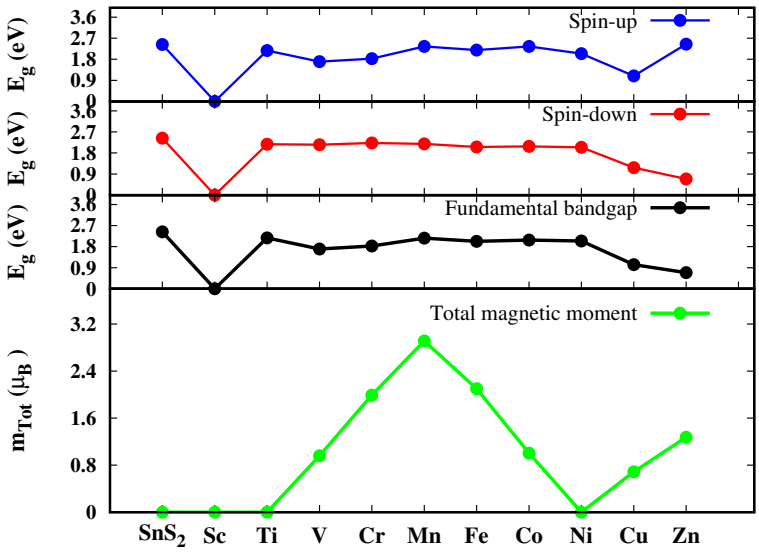

Figure 4.3: Total magnetic moment m_{Tot} (μ_B), fundamental band gap (E_g), spin-up and spin-down band gap values of 3*d* TM doped (6.25% concentration) ML-SnS_2 systems are shown in green, black, red and blue curves, respectively.

V($3d^3 4s^2$), Cr($3d^5 4s^1$), Mn($3d^5 4s^2$), Fe($3d^6 4s^2$), Co($3d^7 4s^2$), Ni($3d^8 4s^2$), Cu($3d^{10} 4s^1$) and Zn($3d^{10} 4s^2$)-doped SnS_2 systems have 0, 0, 1, 2, 3, 4, 5, 6, 7, and 8 unbalanced valence electrons, respectively in comparison with the host Sn-atom ($5s^2 5p^2$). From Ti to Mn, these unbalanced electrons remain unpaired and contribute 0, 1, 2 and 3 μ_B respectively, thereby remaining in high spin states. From Fe onwards, these unbalanced electrons tend to be paired and unpaired. Fe, Co, Ni, Cu, and Zn-doped SnS_2 systems contain 1, 2, 3, 3, and 3 sets of paired electrons and 2, 1, 0, 1 and 2 unpaired electrons, respectively, contributing 2, 1, 0, 0.688 and 1.275 μ_B magnetic moments and belonging to the low spin state.

In a Ti-doped system, two spin-up and spin-down d_{z^2} electrons participate in bonding with S-p_z orbital, and hence there are no unpaired electrons. It is an indirect bandgap semiconductor with E_g 2.17 eV. In Ni-doped systems, the spin-up and spin-down channels are symmetric with a bandgap of 2.04 eV. Here spin-up and spin-down e_2 orbitals overlap with S-p_x,p_y orbitals. e_1 and a_1 orbitals are fully

filled. These are nonmagnetic semiconductors. An asymmetry arises between the two spin channels in the case of V, Cr, Mn, Fe, Co, Cu, and Zn-doped systems with a finite bandgap, which indicates magnetic semiconductors shown in DOS Figure 4.4 (a) to (g). In V-doped system out of five d electrons three spin-up d_{xz}, $d_{x^2-y^2}$ and d_{yz} orbitals are overlapping on S-p_x, p_y, and p_z orbitals, that is shown in DOS plot. One spin-down electron from d_{z^2} orbital is overlapping with S-p_z orbitals. This overlapping orbitals show the strong dp hybridization in the V-doped system. Also a prominent peak arises from d_{xy} orbital in the spin-up channel reveals the presence of unpaired electron which gives 1 μ_B magnetic moment to V-doped SnS_2. It is an indirect bandgap semiconductor with E_g 1.70 eV. Here VBM arises near K-point from S-p_x + V-d_{xy} orbitals and CBM at Γ-point from Sn-s + V-$d_{x^2-y^2}$ orbitals. In Cr-doped system out of six electrons, e_1 orbital has two unpaired electrons, give 2 μ_B magnetic moment. Two spin-up electrons in the degenerate e_2 orbital overlap S-p_x,p_y orbital. One spin-up and spin-down electron in a_1 overlaps on spin-up and spin-down p_z orbital. It is shown in the DOS plot. Here VBM arises at M-point from S-p_x,p_y,p_z + Cr-*e1* orbitals and CBM at Γ-point from S-p_z + Sn-s + Cr-d_{z^2}. This makes it as an indirect bandgap semiconductor with E_g 1.83 eV. In Mn-doped system out of seven electrons, e_1 and a_1 contribute one unpaired electron each and gives 3 μ_B magnetic moment. Spin-up and spin-down Mn-e_2 orbitals overlap on spin-up and spin-down S-p_x,p_y orbitals as shown in DOS. It is an indirect bandgap semiconductor with E_g 2.17 eV. Here VBM arises at M-point from S-p_x,p_y,p_z + Mn-e_1 orbitals and CBM at Γ-point from Sn-s + S-p_x,p_y + Mn-e_1 orbitals. In Fe-doped system, out of eight electrons, d_{xy} and d_{z^2} orbitals have one unpaired electron each and gives 2 μ_B magnetic moment. $d_{x^2-y^2}$ is fully filled. Electrons in spin-up d_{yz}, d_{xz} orbitals overlap on S-p_y,p_x orbitals in the spin-up channel and electrons in spin-down d_{yz}, d_{xz} orbitals overlap on S-p_y,p_x orbitals in the spin-down channel. It is an indirect bandgap semiconuctor with E_g 2.03 eV. Here VBM arises at M-point from

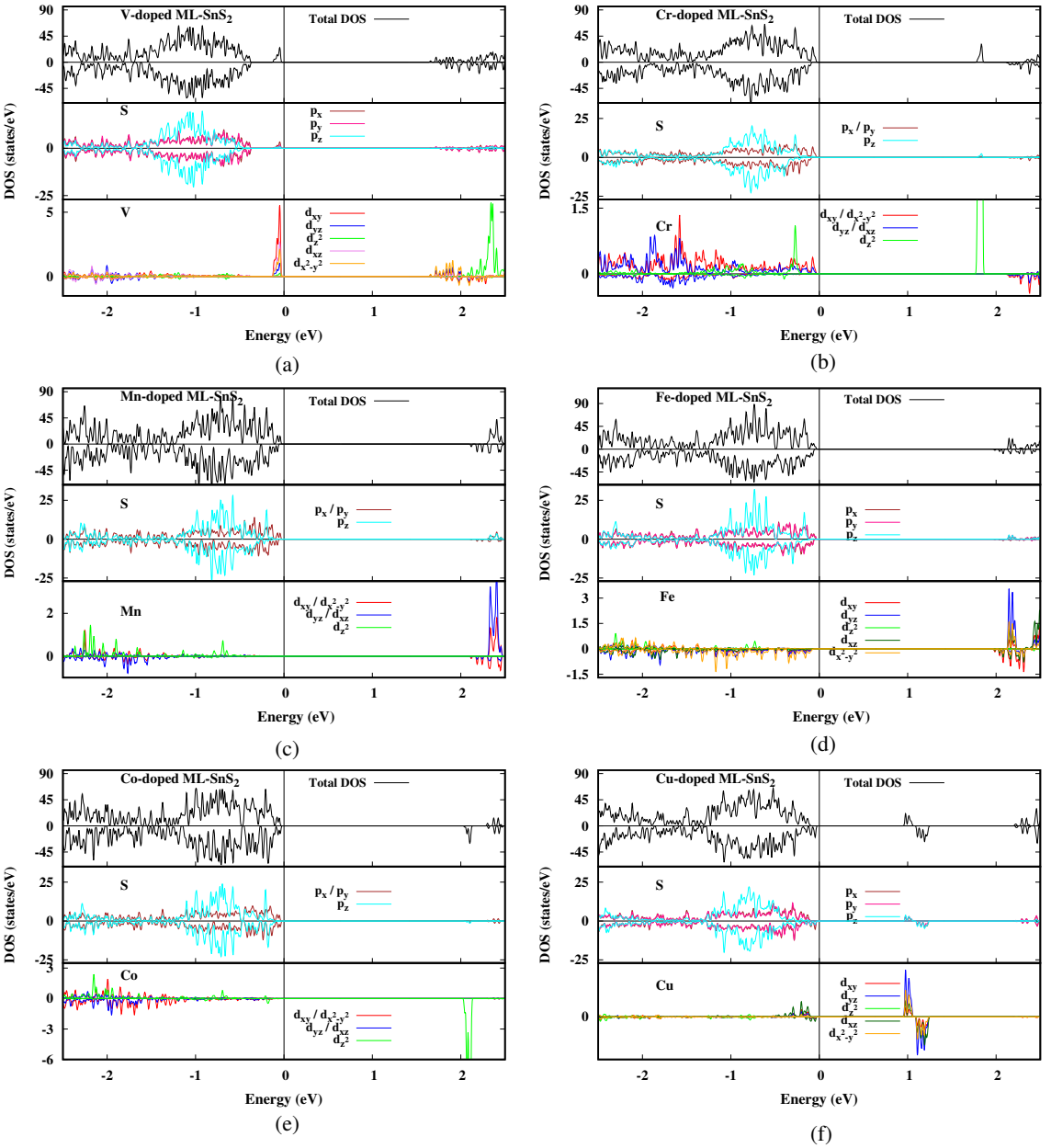

Figure 4.4: Spin-polarized density of states of (a) V, (b) Cr, (c) Mn, (d) Fe, (e) Co, (f) Cu, and (g) Zn-doped mo nolayer SnS_2 systems, calculated using HSE06 functionals. Positive and negative energy values along y-axis indicate the spin-up and spin-down states. Fermi energy is set to zero.

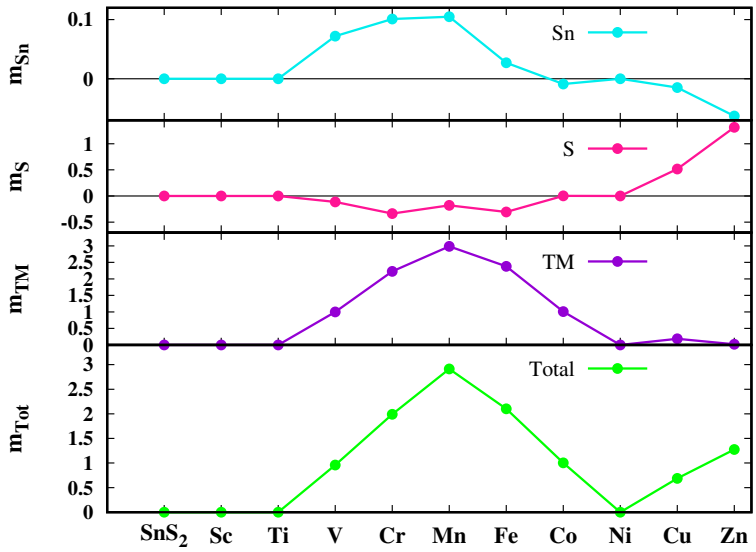

Figure 4.5: Total magnetic moment m_{Tot} (μ_B), magnetic moment due to TM m_{TM} (μ_B, S m_S (μ_B) and Sn m_{Sn} (μ_B) atom of TM doped (6.25% concentration) ML-$_2$ systems are shown in green, violet, pink and cyan curves, respectively.

S-p_x,p_y,p_z + Fe-$d_{x^2-y^2}$ orbitals and CBM at Γ-point from S-p_x + Fe-d_{xz},d_{xy} orbitals. In Co-doped system, out of nine electrons, e_1 orbital is fully filled. The spin-down e_2 orbitals overlap on spin-down S-p_y,p_x orbitals. The spin-up e_1 orbitals overlap on spin-up S-p_y,p_x orbitals. Spin-down e_1 and spin-up e_2 orbitals are fully filled. a_1 orbital gives 1 μ_B magnetic moment. It is an indirect bandgap semiconductor with E_g 2.08 eV. Here VBM arises at M-point from S-p_x,p_y + Co-e_1 orbitals and CBM at Γ-point from Sn-s + Co-a_1 orbitals.

In Cu-doped system, out of ten d electrons, d_{xy}, d_{yz} ,d_{z^2} and d_{xz} orbitals are fully filled. The spin-up d_{yz},d_{xz} orbitals overlap on S-p_y,p_x orbitals and spin-down d_{z^2},d_{xz} overlap on spin-down S-p_z,p_x orbitals. A tiny magnetic moment of 0.196 μ_B arises due to the asymmetry in the spin-up and spin-down $d_{x^2-y^2}$. It is an indirect bandgap semiconductor with E_g 2.03 eV. Here VBM arises at M-point from S-p_x,p_y + Cu-d_{xz} orbitals and CBM at Γ-point from S-p_z,p_x,p_y + Cu-d_{yz} orbitals. In Zn-doped system, out of ten d electrons, e_1 and a_1 orbitals are fully filled in the deeper

energy level. Electrons in spin-up and spin down e_2 orbitals overlap on spin-up and spin-down S-p_y,p_x orbitals. A tiny magnetic moment of 0.086 μ_B arises due to the asymmetry in the spin-up and spin-down $d_{x^2-y^2}$ orbital. Here direct bandgap of 0.69 eV arises at M-point from S-p_x,p_y,p_z + Sn-s + Zn-e_2 orbitals. This tiny magnetic moment in Cu and Zn-doped systems is due to the fully filled shell nature of the 3d orbitals in Cu and Zn atoms.

In V, Cr, Mn, Fe, and Co-doped SnS_2 systems, the total magnetic moment is mainly from the localized 3d orbital of TM atoms. In all these doped systems, the induced magnetic moment by the impurity 3d orbital is antiparallel to the magnetic moment generated by S-atom. As a result, the total magnetic moment is smaller than the dopant atom's local magnetic moment, as shown in Figure 4.5. Even though the total magnetic moments induced in the Cu and Zn-doped systems are 0.688 and 1.275 μ_B, the local moments generated by the 3d-orbitals of Cu and Zn atoms are 0.198 and 0.086 μ_B only. The surrounded S-atoms generate 0.515 and 1.315 μ_B for Cu and Zn-doped systems. This observation is reflected by the S-atom DOS (Figure 4.3 (f) and (g)), which is more asymmetric in these two systems in comparison with other systems. This indicates most of the magnetic moment arises from S-3p orbitals rather than impurity 3d orbital. As the 3d orbitals in Cu and Zn-doped systems are fully filled, they are not sufficient to provide greater magnetic moments like other TM doped systems [272, 154]. On top of this, in these two systems, the induced magnetic moment by 3d orbital is parallel to the magnetic moment generated by surrounded six S-atoms (Figure 4.9 (f) and (g)). As a result, in the total magnetic moment, only a tiny fraction is caused by the 3d orbital, whereas the S-atom causes a more significant part. In all the TM doped systems the overlapping of impurity 3d orbital on S-3p shows strong dp hybridization.

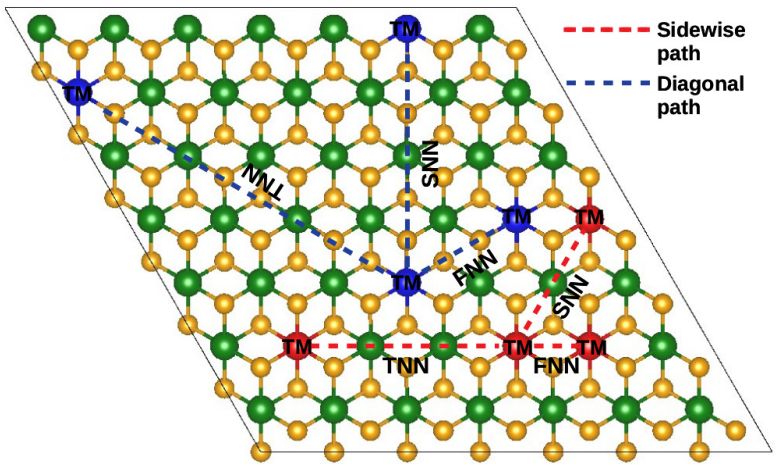

Figure 4.6: Top view of 7×7×1 cell of SnS_2 crystal doped with two identical TM atoms. Green and yellow balls represent Sn and S atom respectively. Red and blue balls are TM atoms. Red and blue dashed lines represent sidewise and diagonal paths.

4.3.5 Magnetism in double TM atom doped ML-SnS_2

To understand the interaction between two identical TM atoms in the doped system, we considered a 7×7×1 cell. In that cell, two Sn atoms are substituted by two identical TM atoms. The distance between the two TM atoms is varied along sidewise and diagonal paths represented as path1 and path2, respectively. It is shown in Figure 4.6. The distance between two TM atoms in sidewise path varies by 3.6, 7.2, and 11.1 Å. It is denoted by red dashed lines as first nearest neighbour (FNN), second nearest neighbour (SNN), and third nearest neighbour (TNN). Similarly, there are three closest neighbour distances along path2: 6.4 (FNN), 12.8 (SNN) and 19.2 (TNN) Å as shown in blue dashed lines. After relaxing the cell, the value of these distances changes slightly. This method is applied to V, Cr, Mn, Fe, Co, Cu, and Zn-doped SnS_2 monolayers which give finite magnetic moment when it is substituted with a single Sn atom. The relaxed ferromagnetic (FM) and antiferromagnetic (AFM) energy are calculated for all these systems. The difference between the FM and AFM energy is represented as $\Delta E = E_{FM} - E_{AFM}$. We plot the

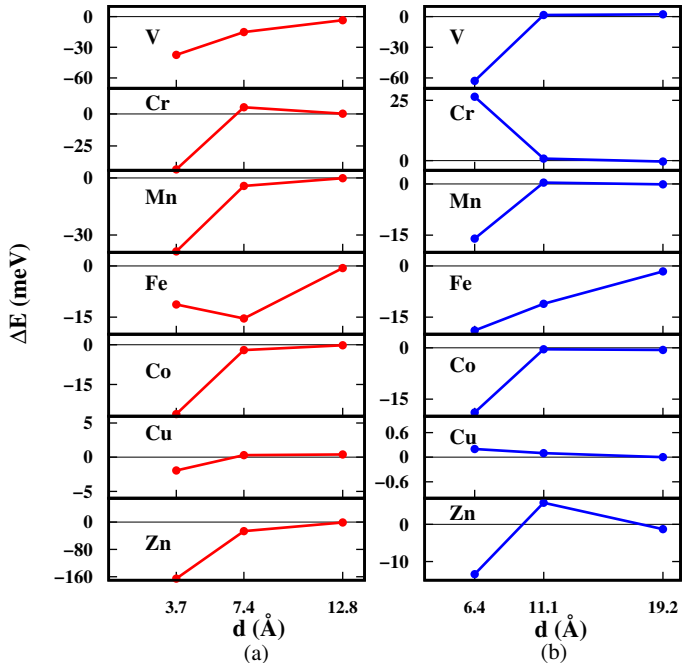

Figure 4.7: ΔE, the energy difference between FM and AFM states as a function of distance between two TM atoms for V, Cr, Mn, Fe, Co, Cu, and Zn-doped ML-SnS_2. Sidewise (a) and diagonal (b) paths are indicated by red and blue curves, respectively.

ΔE as a function of the distance between the two TM dopants in Figure 4.7 (a) and (b) for path1 (red curves) and path2 (blue curves). In the FNN the two TM atoms are separated by 3.3 Å. In this case, the two TM atoms are bridged by the S atom with an angle of 90°. In path2, the two TM atoms are intermediated by S, Sn and S atoms; these intermediate atoms are nonmagnetic only. The two V, Mn, Fe, Co, Cu, and Zn-doped ML-SnS_2 systems induce 2, 6, 4, 2, 1.26 and 2.56 μ_B magnetic moments respectively. As shown in Figure 4.7 (a) and (b) ΔE is negative in both path1 and path2 for V, Mn, Fe, Co, Cu and Zn-doped ML-SnS_2 systems, indicating the ferromagnetic ground state. Only in the case of Cr-doped (4 μ_B) SnS_2, ΔE is negative in path1 and positive in path2, indicating dual magnetic ground states. It has FM coupling in path1 and AFM coupling in path2. Though the Cu-doped SnS_2 exhibits the exact nature, the positive ΔE value in path2 is negligible. It is around 0.3 mev. As the distance between the TM ions increases, the ΔE value becomes

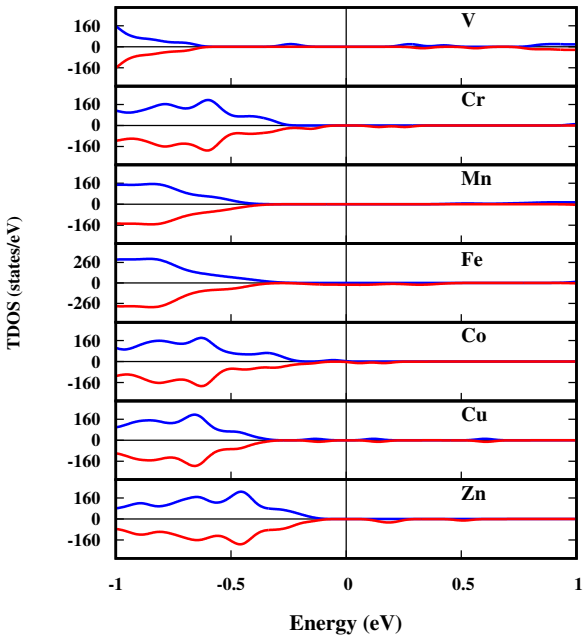

Figure 4.8: Total DOS of two identical TM atoms doped ML-SnS_2, separated by a distance of 3.7 Å for FM coupling.

insignificant in all cases. In the case of Cu-doped system, it is zero for the distance 19.2 Å. In case of V, Cr, Mn, Fe, Co, Cu, Zn-doped SnS_2 systems the energy difference between the FM and AFM states are -3.5, 0.2, -0.1, -0.6, -0.2, 0.4, -1.1 meV for the distance 12.8 , and 2.2, -0.4, -0.1, -1.6, -0.6, 0.0, -1.3 meV for the distance 19.2 respectively. This indicates that the interaction between the two TM atoms decreases as the distance between them increases. All the TM doped systems has negative ΔE value for the first nearest neighbour distance in the sidewise path. In this distance a nonmagnetic S atom bridges the two identical TM atoms with an intermediate angle of 90° (two TM atoms form with an S atom). The magnetic interaction between these two TM atoms is well explained by using the Goodenough-Kanamari-Anderson (GKA) rules [273]. The ferromagnetic coupling is explained by using the GKA rule of 90° superexchange (SE). The total DOS of all these systems are shown in Figure 4.8. Here the spin-up and spin-down channels are shown in blue and red curves. The two Fe and Co atom doped SnS_2 are half-metals, in which one of the

spin channel has semiconducting nature and other has metallic nature. In other words if spin-up channel is semiconductor then spin-down channel is a metal. So the semiconducting channel has 100% spin polarization. Hence these doped systems are potential candidates for spin injector materials. V, Cr, Mn and Zn-doped SnS_2 are magnetic semiconductors with magnetic moment of 2, 4, 6 and 2.56 μ_B, respectively. This factor makes them as attractive materials for spintronic devices.

We have shown the spin distribution of TM doped systems using spin density isosurfaces in Figure 4.9 (a) to (g). As we explained in the previous section 4.3.4, the magnetic moment mainly arises due to the polarized S atoms in case of Cu and Zn-doped systems. It is clearly shown in the spin-density isosurface plots, that the local induced spins of dopant atoms are significantly less, and it is high on the S atom in case of Cu and Zn doped systems (Figure 4.9 (f) and (g)). Hence the spin density is almost of one spin orientation belonging to the S atom. The six S ligands together produce a greater magnetic moment. A tiny magnetic moment induced by the two Cu or Zn atoms are ferromagnetically coupled as the ΔE is negative. The two Cu-doped SnS_2 is a ferromagnetic metal with a magnetic moment of 1.26 μ_B, in that 0.402 μ_B is coming from Cu atoms. The Zn-doped SnS_2 is a half-metal with a magnetic moment of 2.56 μ_B, in that Zn atoms give 0.130 μ_B. Its spin-up channel is 100% spin-polarized. In the case of V, Cr, Mn, Fe, and Co-doped SnS_2 the spin density isosurface shows that the spins of the TM atoms are parallel to each other. Once again, it indicates the FM coupling between the two TM atoms. Also, in all of these cases, the spins of the TM atoms are antiparallel to the induced spins of the six nearest neighbour S atoms. Hence the resultant or the total magnetic moment is smaller than the local magnetic moment of TM atoms.

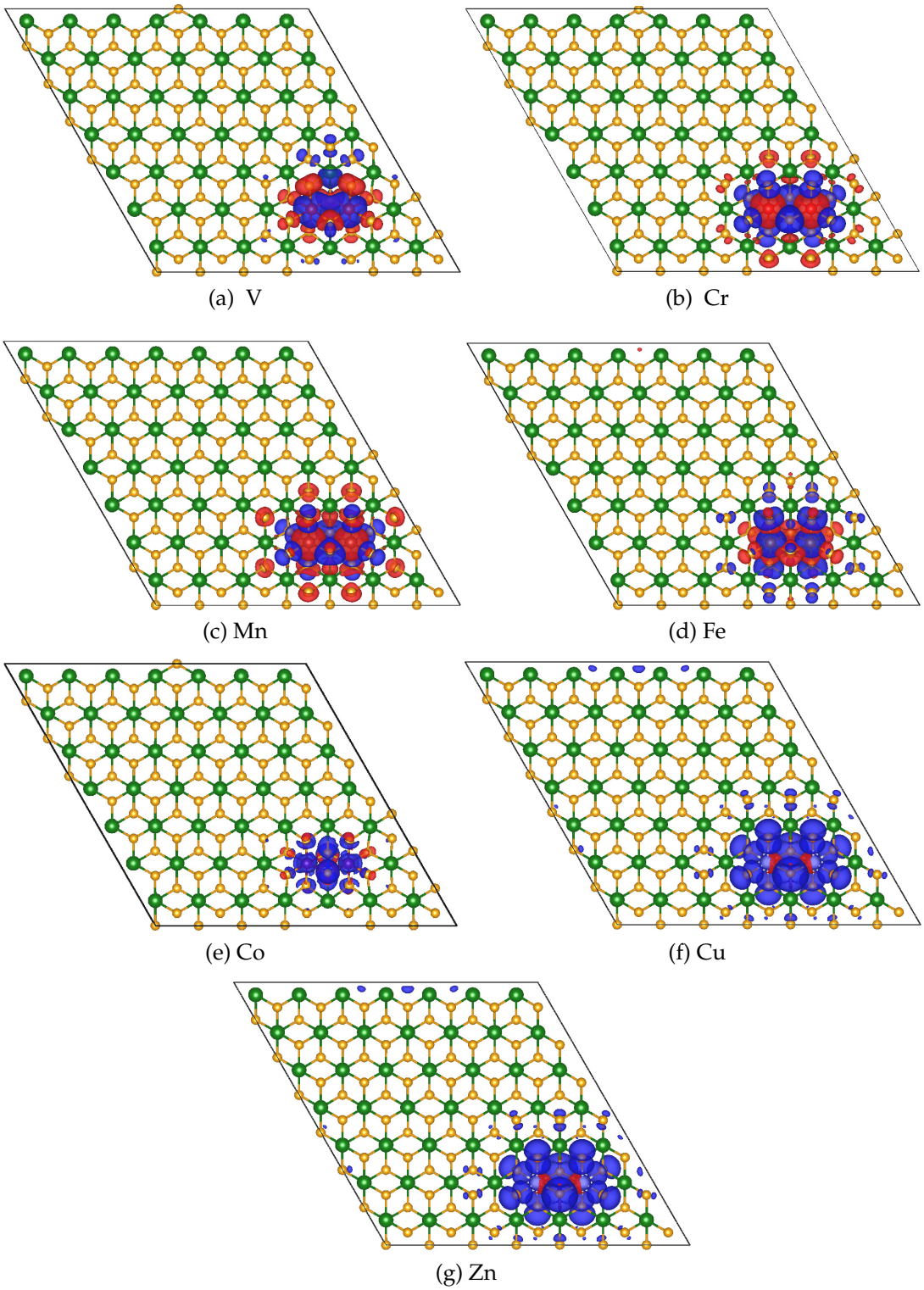

(a) V (b) Cr

(c) Mn (d) Fe

(e) Co (f) Cu

(g) Zn

Figure 4.9: Spin densities of two V, Cr, Mn, Fe, Co, Cu, and Zn atoms and its neighboring S atoms in the double TM atoms doped SnS_2 systems for first nearest configuration of path1 at 4.08% dopant concentration. Blue and red isosurfaces represent positive and negative spin densities (+0.001 eV $Å^{-3}$), respectively.

4.4 Conclusion

We have systematically studied the formation energy, electronic properties and magnetic properties of 3*d* transition metal-doped SnS_2 monolayer. Formation energy calculation reveals that the Sn-poor (S-rich) condition is the favourable condition to incorporate the TM atom into SnS_2 crystal at Sn-site. Double TM doped systems with negative binding energies indicate that two TM atoms prefer to stay together at two different Sn-sites in ML-SnS_2.

The spin-polarized HSE06 band structure calculations reveal that single V, Cr, Mn, Fe, Co, Cu and Zn-doped SnS_2 are semiconductors with the magnetic moment of 1, 2, 3, 2, 1, 0.688, and 1.275 μ_B respectively. Sc-doped system is a nonmagnetic metal. Ti and Ni-doped systems are nonmagnetic semiconductors. Ni and Zn-doped SnS_2 are direct bandgap semiconductors, and all other doped systems are indirect bandgap semiconductors. As the Ni-doped SnS_2 is direct bandgap semiconductor it is good for optoelectronic devices. Except for V, Fe and Cu-doped SnS_2 all other systems have trigonal prismatic geometry in the 3*d* orbitals. A strong *dp* hybridization occurs in all the doped systems, which is confirmed by the overlapping of transition metal 3*d* and sulfur 3*p* orbitals in the DOS plot. Due to the fully filled *d* orbitals, the local magnetic moment induced by the Cu and Zn atoms is significantly less (0.196 and 0.086 μ_B). Most of the total magnetic moment in these systems comes from the six S ligand field.

In the double transition metal atom doped SnS_2, the ferromagnetic ground state is observed for V, Cr, Mn, Fe, Co and Zn-doped SnS_2 system. The 90° superexchange operates the FM coupling in all these systems for the first nearest neighbour distance. Among them, the V, Cr, Mn, and Zn-doped ML-SnS_2 are ferromagnetic semiconductors with the magnetic moment of 2, 4, 6 and 2.56 μ_B, respectively. Further, Fe and Co-doped ML-SnS_2 are ferromagnetic half-metals with

the magnetic moment of 4 and 2 μ_B respectively. In this article the magnetic moment formation in all the single and double TM atom-doped monolayer SnS_2 are well explained. Magnetic half-metals exhibit 100% spin polarization. Hence they are suitable spin injector materials. In conclusion, ferromagnetic semiconductors, ferromagnetic half-metals and ferromagnetic metal are obtained by doping the 3*d* transition metals into SnS_2 monolayer. These results show that the 3*d* transition metal doping on SnS_2 monolayer is important for spin injection, spin polarized current generation and other spintronic device applications.

CHAPTER 5

RASHBA SPIN-SPLITTING IN JANUS SNXY/WXY (X, Y = S, SE, TE WITH X $\neq$ Y) HETEROSTRUCTURES

Janus transition metal dichalcogenide monolayers have shown a lack of mirror symmetry perpendicular to the 2D plane. The breaking of out-of-plane symmetry, along with the spin-orbit coupling, induces Rashba spin splitting in these materials. In this chapter, we study the Rashba spin splitting in Janus tin dichalcogenide monolayers. In addition, we also discuss the heterostructures from Janus SnXY and WXY monolayers. A Rashba spin-splitting energy of about 43 meV, more significant than the room temperature energy, is observed in the SnSSe/WSSe heterostructure. We examined the consequences of vertical strain on the semiconducting heterostructure. Compressive vertical strain enhances the Rashba splitting, and tensile strain reduces the Rashba splitting. The SnSSe/WSSe heterostructure remains semiconductor only with Rashba bands near the Fermi level with an increase in the Rashba parameter of about 0.96 eVÅ and splitting energy of about 72 meV for the compressive strain of 10.4%. The calculated spin precession length for the corresponding momentum offset is about 1.04 nm. These findings confirm that the SnSSe/WSSe heterostructure is a good Rashba material and a productive material for spintronic device applications. The manuscript involving the results of this work is under preparation.

5.1 Introduction

Janus transition metal dichalcogenide monolayers are promising candidates for optoelectronic and spintronic applications. In most of the Janus TMXY (TM = transition metal, X, Y = S, Se, Te with X ≠ Y) monolayers, one can observe the interesting physics in the band nature, which is absent in transition metal dichalcogenide (TMX_2) monolayers. In recent years transition metal dichalcogenides (TMDCs) have been essential materials for electronic and optoelectronic device making. Though the TMDC monolayers exhibit coupled spin and valley physics [274] due to strong spin-orbit coupling (soc) [275], and lack of in-plane inversion symmetry, the Rashba type spin splitting [88] is not present in monolayer TMDCs. The Rashba spin splitting (RSS) strictly demands the breaking of inversion symmetry along the out-of-plane direction of the crystal. As the monolayer TMDCs possess out-of-plane inversion symmetry, they failed to produce Rashba spin splitting in their electronic band structure. This limitation was overcome by the successful synthesis of the Janus MoSSe monolayer. It was fabricated using monolayer MoS_2 through chemical vapor deposition [276] in 2017. Some particular ways to break the out-of-plane inversion symmetry include applying the electric or magnetic field perpendicular to the crystal plane. Also, the interfaces across the vertical heterostructures break the out-of-plane inversion symmetry. This is the effect of a built-in electric field across the interface perpendicular to the 2D plane.

In the TMX_2 monolayers, the metal atom is bonded to the two identical chalcogen atoms (X) with similar potential energy; this will not allow having RSS. When one of the chalcogen atoms is replaced by a different chalcogen atom (Y), a potential gradient will be created along the out-of-plane direction. The potential drop across TM-X and TM-Y environments is different in this case. Due to this, the built-in electric field generated perpendicular to the crystal plane allows the

TMXY monolayer to possess RSS. This approach of building the internal electric field perpendicular to the crystal plane by bonding the metal atom with two different chalcogen environments attracted the other TMX_2 systems to produce RSS. In this regard, monolayers of MoSTe, MoSeTe, WSSe, WSTe, and WSeTe [97] exhibit considerable Rashba effect. The strong soc and lack of inversion symmetry along the out-of-plane direction make them better candidates for spintronic applications. The heterostructures of MoXY, and WXY monolayers exhibit enhanced RSS [277]. The Janus monolayers of other transition metals for TM = Ti, Zr, Hf, V, Nb, Ta, Cr, Pt and X, Y = S, Se, Te, Cl, Br, O are also studied using first-principles calculations [278, 279, 280, 281, 282, 283].

In the recent studies on Janus transition metal dichalcogenide (J-TMXY) monolayers, one can see the development of other metals in place of transition metals. This work focuses on Janus tin dichalcogenide (SnXY, X, Y = S, Se, Te with X ≠ Y) monolayers and their heterostructures with WXY monolayers. The electronic and optical properties of Janus SnSSe, SnSTe, and SnSeTe monolayers are well studied using first-principles calculations [284, 285, 286]. The density functional theory studies have proven that these Janus SnXY monolayers are energetically and dynamically stable materials [287]. J-SnSSe is predicted as a good candidate for solar cell design [288]. Along with applicable optoelectronic properties J-SnSSe monolayers [285, 286] have also expanded their applications in the thermoelectric and piezoelectric perspectives [287, 289, 290]. But, the applications towards the spintronic perspective have yet to be studied from J-SnXY monolayers. The spin-related studies of these J-SnXY monolayers are not entirely performed. Hence in this study, we focus on the spin-splitting in the Janus-SnXY monolayers and their heterostructures with J-WXY monolayers, which leads to a significant Rashba effect. This work will take forward by applying vertical strain on heterostructure.

Table 5.1: Relaxed lattice parameters a, Sn-X d_{Sn-X} and Sn-Y d_{Sn-Y} bond lengths, thickness h_0, PBE and HSE06 band gap values with and without incorporating soc E_g^{PBE}, $E_g^{PBE+soc}$, E_g^{HSE06} and $E_g^{HSE06+soc}$ for SnS_2, $SnSe_2$, $SnTe_2$, J-SnXY and J-WXY monolayers. Here X and Y are chalcogen atoms with smaller and larger atomic numbers respectively.

System	a (Å)	d_{Sn-X} (Å)	d_{Sn-Y} (Å)	h_0 (Å)	E_g^{PBE} (eV)	$E_g^{PBE+soc}$ (eV)	E_g^{HSE06} (eV)	$E_g^{HSE06+soc}$ (eV)
SnS_2	3.68	2.59	-	2.96	1.45	1.44	2.43	2.429
	3.68	2.59	-	-	1.45	-	2.43	-
	[196]	[196]	-	-	[291]	-	[291]	-
$SnSe_2$	3.87	2.74	-	3.19	0.95	0.946	1.46	1.41
	3.82	2.73	-	3.212	0.953	1.41		
	[292] [292]	-	[285]	0.953	[292]			
$SnTe_2$	4.14	2.98	-	3.56	0.0	0.0	0.23	0.0
	4.10	2.74	-	-	-	-	-	-
	[293]	[293]	-	-	-	-	-	-
J-SnSSe	3.782	2.63	2.72	3.07	0.96	0.83	1.71	1.59
	3.81	2.63	2.72		0.95	-	1.69	-
	[287]	[287]	[287]		[286]	-	[287]	-
J-SnSTe	3.901	2.66	2.93	3.30	0.0	0.0	0.0	0.0
	3.89	2.64	2.96	-	-	-	-	-
	[284]	[287]	[287]	-	-	-	-	-
J-SnSeTe	3.984	2.78	2.94	3.39	0.0	0.0	0.0	0.0
	3.98	2.77	2.98	3.43	-	-	-	-
	[284]	[287]	[287]	[284]	-	-	-	-
J-WSSe	3.248	2.423	2.539	3.25	1.71	1.42	2.19	1.92
	3.232	2.421	2.538	-	1.77,1.72	1.23	2.27,2.13,2.15	1.85
	[97]	[97]	[97]	-	[97], [294]	[97]	[97], [295], [294]	[296]
J-WSTe	3.362	2.439	2.723	3.39	1.23	1.14	1.79	1.67
	3.344,3.27	2.559	2.722	-	1.34,1.23	0.85,1.14	1.82,1.71	-
	[97], [294]	[97]	[97]	-	[97], [294]	[97], [297]	[97], [294]	-
J-WSeTe	3.392	2.573	2.751	3.46	1.30	1.08		1.48
	3.413	2.559	2.722	-	1.42	0.83	1.88,1.79	1.40
	[97]	[97]	[97]	-	[97]	[97]	[97], [296]	[296]

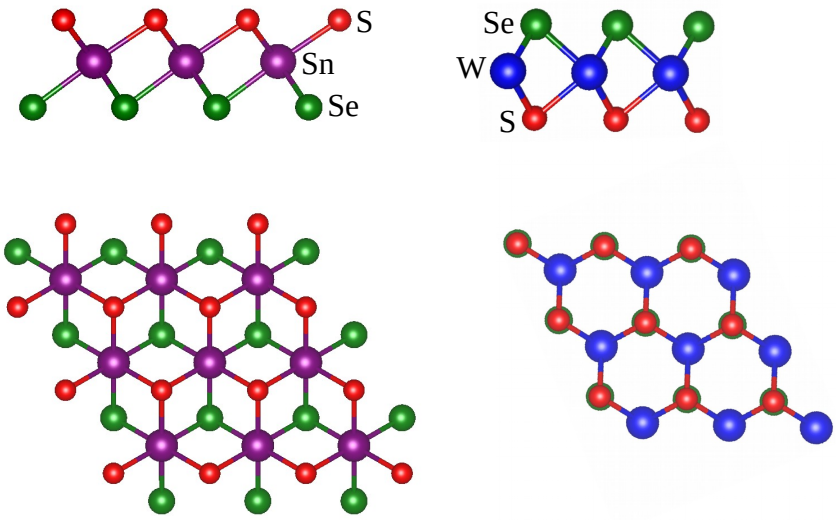

(a) 1T-SnSSe (b) 2H-WSSe

Figure 5.1: Crystal structures of Janus (a) 1T-SnSSe and (b) 2H-WSSe monolayers. Upper panel shows the side view and lower panel shows the top view of the crystals. Purple and blue balls represent Sn and W atoms, respectively. Red and green balls represent S and Se atoms, respectively.

Table 5.2: Band gap using orbital projected PBE band structure included with soc $E_g^{\mathrm{PBE+soc}}$, intersection energy E_{int}, energy difference E_R, momentum offset k_R for the Rashba bands splitting at Γ-point, and Rashba parameter α_R for the J-SnXY, J-SnXY/WXY and J-WXY layers. The Rashba spin splitting along Γ-M and Γ-K are given separately.

System	$E_g^{\mathrm{PBE+soc}}$ (eV)	E_{int} (eV)	Γ-M E_R (meV)	Γ-M k_R $(Å)^{-1}$	Γ-M α_R (eVÅ)	Γ-K E_R (meV)	Γ-K k_R $(Å)^{-1}$	Γ-K α_R (eVÅ)
J-SnSSe	0.80	1.199	0.15	0.0164	0.018	1.03	0.0189	0.109
J-SnSSe/WSSe	0.55	-0.323	42.96	0.122	0.704	42.91	0.126	0.681
J-WSSe	1.39	-0.478	2.694	0.0376	0.143	2.743	0.0436	0.126
J-SnSTe	-	0.539	5.031	0.0162	0.621	6.95	0.0184	0.755
J-SnSTe/WSTe	-	-0.051	2.34	0.0364	0.129	2.47	0.0366	0.135
J-WSTe	1.05	-0.291	7.58	0.0546	0.278	7.78	0.0631	0.247
J-SnSeTe	-	0.704	1.05	0.0156	0.135	2.46	0.0180	0.273
J-WSeTe	0.99	-0.487	35.7	0.145	0.492	23.5	0.123	0.380

Table 5.3: Band gap using orbital projected PBE band structure included with soc $E_g^{PBE+soc}$, intersection energy E_{int}, energy difference $E_R(E_{R-like})$, momentum offset $k_R(k_{R-like})$ for the Rashba(Rashba-like) bands splitting at M-point, and Rashba(Rashba-like)parameter $\alpha_R(\beta_{R-like})$ for the J-SnXY and J-SnXY/WXY layers. The Rashba spin splitting along M-Γ and M-K are given separately.

System	$E_g^{PBE+soc}$ (eV)	E_{int} (eV)	M-Γ E_R (meV)	M-Γ k_R $(Å)^{-1}$	M-Γ α_R (eVÅ)	M-K E_{R-like} (meV)	M-K k_{R-like} $(Å)^{-1}$	M-K β_{R-like} (eVÅ)
J-SnSSe	0.80	0.405	0.324	0.0163	0.039	0.76	0.0096	0.158
J-SnSSe/WSSe	0.55	0.274	0.656	0.0094	0.139	0.635	0.0083	0.152
J-SnSTe	-	-0.316	0.983	0.0159	0.124	23.01	0.0277	1.661
J-SnSTe/WSTe	-	-0.393	17.72	0.0272	1.303	15.27	0.0327	0.934
J-SnSeTe	-	-0.187	0.62	0.0156	0.079	11.3	0.0271	0.833
J-SnSeTe/WSeTe	-	-0.377	10.74	0.018	1.193	9.38	0.0238	0.788

5.2 Computational Details

To investigate the properties of J-SnXY and J-WXY heterostructures, we performed the first-principles calculations [179] using Vienna *ab initio* Simulation Package(VASP) [180]. Projector augmented wave (PAW) [182, 183] pseudopotentials are used for electron-ion interactions in these calculations. Perdew, Burke, and Enzerhof (PBE) Generalized Gradient Approximation (GGA) [109] are used to relax the monolayers. As the ground state of J-SnXY and J-WXY monolayers belong to the trigonal prismatic and hexagonal phases, the heterostructures derived from their unit cells have a lattice mismatch greater than 5%. To suppress the lattice mismatch, heterostructures (HSs) are constructed using $2\times2\times1$ supercell of J-WXY monolayer and $\sqrt{3}\times\sqrt{3}\times1$ supercell of J-SnXY monolayer rotated by 30°. The J-SnSSe/WSSe, J-SnSTe/WSTe, and J-SnSeTe/WSeTe HSs have the least lattice mismatch of 0.069, 0.4, and 1.52%, respectively. The individual layers are stacked within each heterostructure by Van der Waals (vdw) interaction. Hence all these HSs are relaxed using PBE functionals

with a vdw functional. Here Grimme's DFT-D2 [298] method is employed for vdw interaction. Each J-SnXY, J-WXY monolayers and their heterostructures are relaxed using a force convergence criterion of 10^{-3} eV/Å and a tight energy convergence criterion of 1×10^{-6} eV. Cut-off energy of 450 eV is used. The thickness of the vacuum layer along the z-direction is relaxed to 30 Å. The Brillouin zone sampling was employed by Monkhorst-Pack [186] k-grid of size $21\times21\times1$ for monolayers and $13\times13\times1$ for heterostructures. Spin-orbit coupling (soc) is involved in all the PBE bandstructure calculations involving vdw functional.

5.3 Results and discussion

5.3.1 Janus-SnXY and WXY monolayers

J-SnXY monolayers can be created using SnS_2 or $SnSe_2$ or $SnTe_2$ monolayers which belong to the space group of $P\bar{3}m1$ [59, 197, 58]. In SnX_2 monolayers, the two chalcogen atoms bonded with the Sn atom in a trigonal geometry, thereby creating mirror symmetry in the crystal structure. This mirror symmetry will break when one of the chalcogen atoms is replaced by a different one. In Janus-SnXY monolayers, the Sn atom layer is sandwiched by two unidentical chalcogen atom layers, X and Y. The well-known J-WXY monolayers belong to $P6_3/mmc$ space group, the chalcogen and metal atoms are in hexagonal geometry. The crystal structure of J-SnXY and J-WXY monolayers are shown in Figure 5.1. The relaxed lattice parameters, bond lengths, thickness, and band gap values were calculated using PBE and HSE06 functionals with and without soc for SnS_2, $SnSe_2$ and $SnTe_2$, J-SnXY and J-WXY monolayers are listed in Table 5.1. In SnX_2 monolayers, as the atomic number of the chalcogen atom increases, the lattice parameter increases, and the band gap decreases from 2.43 eV (SnS_2) to 1.46 eV ($SnSe_2$) to ($SnTe_2$) 0.23 eV. In J-SnXY monolayers also, we can see this trend of increasing lattice parameters with

the size of the chalcogen atom. The lattice parameters of each J-SnXY monolayer are in between the lattice parameters of SnX_2 and SnY_2 monolayers, $a_{SnX_2} < a_{SnXY} < a_{SnY_2}$. Here X and Y are chalcogen atoms with smaller and larger atomic numbers, respectively. J-SnSSe monolayer has a semiconducting gap of 0.96 eV using PBE and 1.71 eV using HSE06 functionals. With soc, the PBE and HSE06 gaps reduce to 0.83 eV and 1.59 eV, respectively. It is an indirect band gap semiconductor with a conduction band edge located at M-point and a valence band edge located at Γ-point (Figure 5.6 (a)). The conduction band edge is mainly originating from Sn *s*-orbital, and it has a small contribution from S and Se p_x+p_y-orbitals. Valence band edge is mainly contributing from Se p_x+p_y-orbitals and lightly from S p_x+p_y-orbitals. The band structures of monolayers with Te environment, such as J-SnSTe and J-SnSeTe, acquire metallicity, which is shown in Figure 5.10 (a) and 5.13 (a). The metallicity is mainly originating from the Te p_x+p_y-orbitals and less from Se p_x+p_y-orbitals. The J-WXY monolayers are semiconductors in which J-WSSe and J-WSeTe are direct gap semiconductors. The soc included orbital projected PBE band structure of J-SnXY, and J-WXY monolayers are shown in Figure 5.6, Figure 5.10, and Figure 5.13 (a) and (c).

5.3.2 Rashba spin splitting in J-SnXY and J-WXY monolayers

In J-SnXY monolayers, the X and Y chalcogen atoms have different electronegativities. The electric field directs from a lower electronegative atom to a higher one. Due to the difference in the electronegativity of chalcogen atoms, the electron transfer from Sn to X and Sn to Y atoms are different. This difference in the charge transfer can be seen from the Bader charge analysis. In the J-SnSSe monolayer, the Sn atom loses 1.34 e. S and Se atoms gain 0.74 e and 0.60 e, respectively. The charge aggregation on the S atom is more than in the Se atom. This is because the S atom has more electronegativity than the Se atom. Due to the unequal charge ag-

gregation on chalcogen atoms, a net electric field will be created that directs from Se to S atom, which is absent in the SnX_2 monolayers. Similarly, using the Bader charge analysis, we observed that the electric field points from Te to S and Te to Se in J-SnXY and J-WXY monolayers with S-Te and Se-Te chalcogen environments.

Now the presence of two different chalcogen atoms breaks the out-of-plane mirror symmetry in the Janus monolayers, and this intern produces asymmetry in the potential perpendicular to the 2D plane. Hence an internal electric field builds normal to the crystal plane, $\vec{E}_{int} = \nabla V$. In presence of $\vec{E}_{int}$ the moving electron experiences an effective magnetic field $B_{eff} = \nabla V \times \vec{p}$, which is perpendicular to both $\vec{E}_{int}$ (∇V) and $\vec{p}$. B_{eff} quantizes the electron spins. As the magnetic field depends on electron momentum direction, spin orientation is also momentum dependent. As electrons are restricted to the 2D plane, their momentum ($p = \hbar\vec{k}$, $\vec{k}$ is wave vector) is in-plane. Thus the electron spins change orientation in the 2D plane according to the $\vec{k}$-direction. Due to the presence of $\vec{E}_{int}$, electrons lose their spin degeneracy within the same energy band. This produces spin splitting of the energy band within the 2D plane. Hence the two bands now possess opposite spin polarizations, which are in-plane. Hamiltonian for the pure RSS in a 2D plane is given by

$$H_R = \alpha_R |\vec{E}_{int}| (\vec{\sigma} \times \vec{k}).\hat{z} \tag{5.1}$$

Here α_R is the Rashba parameter, $\vec{\sigma}$ is the Pauli spin matrices, $\vec{E}_{int}$ is the internal electric field, and $\hat{z}$ is the unit vector perpendicular to 2D-plane.

$$\vec{\sigma} \times \vec{k} = (\sigma_y k_z - \sigma_z k_y)\hat{x} + (\sigma_z k_x - \sigma_x k_z)\hat{y} + (\sigma_x k_y - \sigma_y k_x)\hat{z} \tag{5.2}$$

$$(\vec{\sigma} \times \vec{k}).\hat{z} = \sigma_x k_y - \sigma_y k_x \tag{5.3}$$

This implies,

$$H_R = \alpha_R |\vec{E}_{int}| (\sigma_x k_y - \sigma_y k_x) \tag{5.4}$$

Thus equation (5.4) shows that for the pure RSS, both the spin and momentum components are strictly in-plane, and their out-of-plane component is absent. Unlike the Zeeman splitting, here, the spin splitting is $\vec{k}$-dependent due to $\vec{k}$-dependent in-plane spin orientation.

Thus band dispersion relation for the spin split bands is given by

$$E \pm (k) = \frac{\hbar^2}{2m^*} \pm \alpha_R |\Delta k| \tag{5.5}$$

where m^* is the effective mass of the electron. The E_+k and E_-k represent energy eigenstates for the opposite in-plane spin polarization and are shifted by Δk. By keeping the one parabolic band fixed, other bands will either shift by $+\Delta k$ or by $-\Delta k$. This is what exactly happens in the pure Rashba type of spin splitting. This dispersion relation is the well-known Rashba spin splitting or the Rashba effect. Here α_R dictates the strength of Rashba spin splitting. This is given by

$$\alpha_R = \frac{2 * E_R}{k_R} \tag{5.6}$$

Here E_R is the amount of spin splitting energy, and to operate the device at room temperature $E_R \geq 25$ meV. k_R the wavenumber difference between the two Rashba spin split bands. The relationship between the spin precession channel length L and α_R, ($L = \pi\hbar^2/(2m^*\alpha_R)$ [299, 300]) implies spin precession length, $L = \pi/2k_R$ [99]. Here $\pi = 180^\circ$ is the spin precession angle, and m^* is the effective mass of the electron. To get a spin precession angle of 180°, the spin precession length should be in the range of 1 nm. Thus, a larger Rashba parameter (≥ 1 eVÅ) allows the device to operate with a shorter channel length (1 nm). In other words, a wavenumber

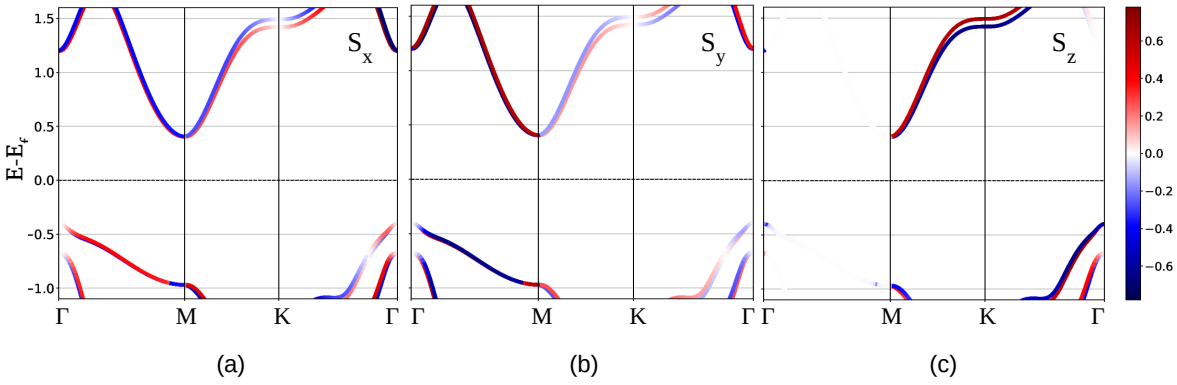

Figure 5.2: Spin projected PBE band structure of J-SnSSe monolayer included with soc. (a) S_x, (b) S_y and (c) S_z are the spin projection components along x,y (in-plane) and z (out-of-plane) directions respectively.

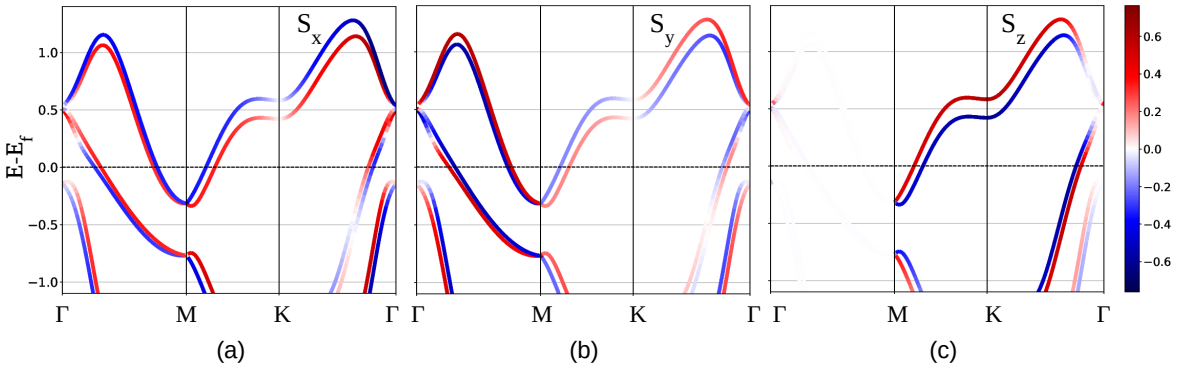

Figure 5.3: Spin projected PBE band structure of J-SnSTe monolayer included with soc. (a) S_x, (b) S_y and (c) S_z are the spin projection components along x,y (in-plane) and z (out-of-plane) directions respectively.

difference of at least 0.157 $Å^{-1}$ provides a channel length of 1 nm.

J-SnSSe has spin splitting at two symmetry points, Γ-point ; along Γ-M and Γ-K path and M-point ; along M-Γ and M-K path. The spin-projected PBE band structures with soc is shown in Figure 5.2. Here S_x and S_y are the in-plane, and S_z is the out-of-plane spin projection components. Only the in-plane spin polarization components are present in pure RSS bands, and the out-of-plane spin polarization component is absent. In Figure 5.2 (a) and (b) at Γ-point along the Γ-M and Γ-K paths and at M-point along M-Γ path, the spin split bands show only in-plane spin

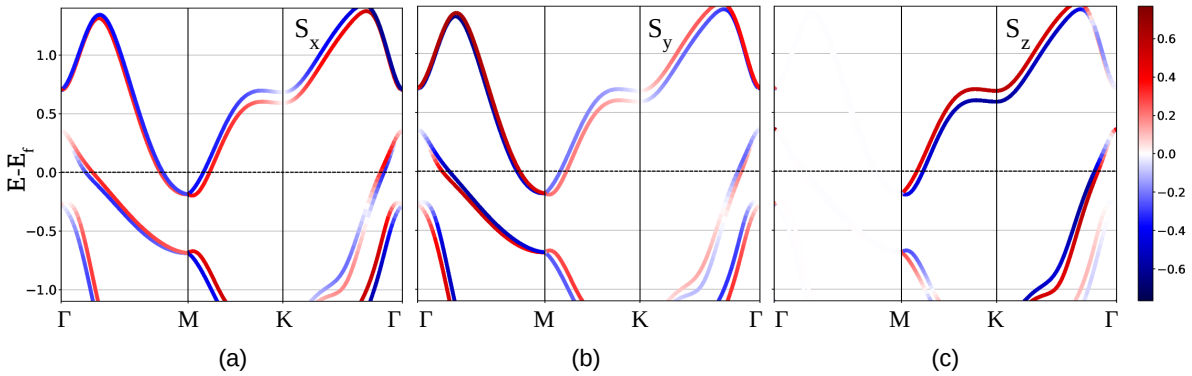

Figure 5.4: Spin projected PBE band structure of J-SnSeTe monolayer included with soc. (a) S_x, (b) S_y and (c) S_z are the spin projection components along x,y (in-plane) and z (out-of-plane) directions respectively.

polarizations and out-of-plane spin polarization is absent. Hence the spin splitting along these paths is pure RSS. But at M-point along M-K path, the splitting has a significant contribution from out-of-plane spin polarization (Figure 5.2 (c)), and in-plane spin polarization components are absent. To explain the origin of the spin splitting along the M-K path, we go back to equation 5.2, here M-point has only the x-coordinate, and the K-point has both the x and y-coordinates. It is evident that the $\vec{k}$ is in-plane and σ_x, $\sigma_y = 0$, then

$$H_R = \beta_R |\vec{E}_{int}| (\vec{\sigma} \times \vec{k}).\hat{m} \tag{5.7}$$

Here $\hat{m} = \hat{x} + \hat{y}$.

$$\vec{\sigma} \times \vec{k} = \sigma_z k_x \hat{y} - \sigma_z k_y \hat{x} \tag{5.8}$$

$$H_R = \beta_R |\vec{E}_{int}| \sigma_z (k_x \hat{y} - k_y \hat{x}).(\hat{x} + \hat{y}) \tag{5.9}$$

$$H_R = \beta_R |\vec{E}_{int}| \sigma_z (k_x - k_y) \tag{5.10}$$

Though it's not the pure RSS, one can call it Rashba-like spin splitting [301], the trigonal layered $PtBi_2$ (bulk) exhibits pure Rashba spin splitting along in-plane momentum direction, and the spin splitting observed along out-of-plane (k_z) direction is considered as Rashba-like spin splitting. In our study, as the system is monolayer, the k_z component is absent, but along the in-plane momentum direction, we observed the presence of out-of-plane spin polarization. As shown in Figure 5.3 and 5.4 in J-SnSTe and J-SnSeTe monolayers, the spin splitting at M-point along the M-K path has considerable S_z contribution and has no involvement of in-plane spin polarization. Along the M-Γ path, it is pure RSS.

Thus all three J-SnXY monolayers exhibit significant Rashba-like spin splitting along the M-K path due to the presence of out-of-plane spin polarization. This unusual spin splitting in all the three J-SnXY monolayers along the M-K path originates mainly from Sn-*s* orbital and less but equally from *p* orbital of X and Y chalcogen atoms (Figure 5.6 (a), Figure 5.10 (a), Figure 5.13 (a)). Below the Fermi level, the bands are significantly originating from *p*-orbital of bigger chalcogen atom (Y) and less from *p*-orbital of smaller chalcogen atom (X). Here the contribution from Sn-*s* orbital is negligible. The spin splitting energy E_R, a shift in momentum k_R, and Rashba parameter α_R at G and M-point are listed in Table 5.2 and 5.3, respectively. Janus SnSSe, SnSTe, and SnSeTe monolayers exhibit the highest E_R of 0.76, 23.01, and 11.3 meV, respectively, and α_R of 0.109, 0.755, and 0.273 eVÅ^3, respectively. The Rashba-like splitting energy for the three monolayers at M-point along the M-K path is 0.76, 23.01, and 11.3 meV, respectively. The respective splitting parameters (β_{R-like} = 2*E_{R-like}/k_{R-like}) are 0.158, 1.661 and 0.833 eVÅ for Janus SnSSe, SnSTe, and SnSeTe monolayers. The E_R values for Janus WSSe, WSTe, and WSeTe monolayers are 2.743, 7.78, and 35.7 meV, respectively, at G-point. Corre-

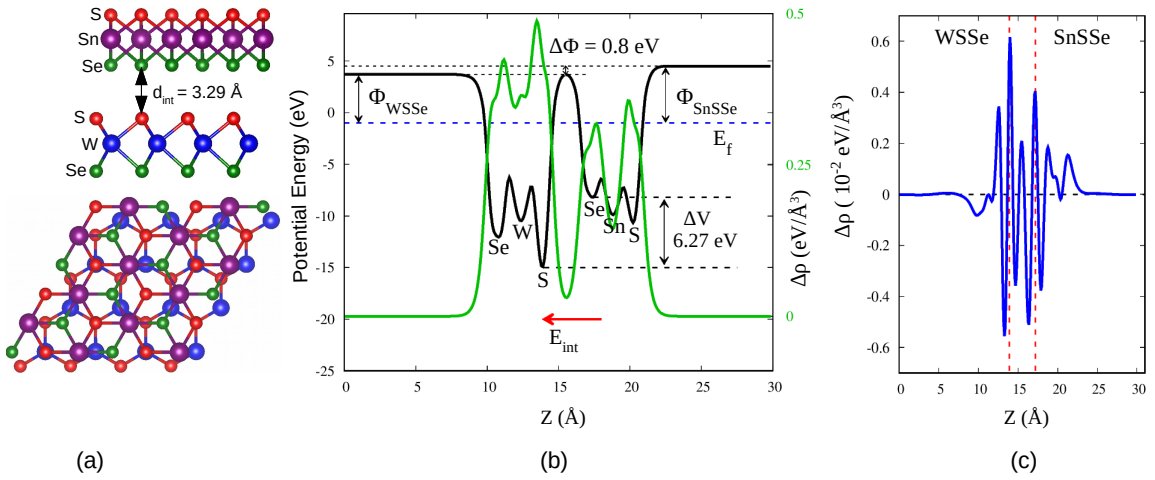

Figure 5.5: For the SnSSe/WSSe HS crystal structure (side and top view) (a), planar average of the electrostatic potential energy is shown in black line and planar average of the charge density is shown in green line (c). Here the Fermi energy is indicated by blue dashed line. Internal electric field E_{int} points from Se to S across Se-S interface, shown in red arrow. Planar average of the charge density difference of the HS is shown in blue line (d),the space between the two red dashed lines is the interface formed by the SnSSe and WSSe layers.

sponding α_R values are 0.126, 0.247, and 0.492 eVÅ, respectively. These findings are calculated using the PBE band structure with vdw correction and soc. The material with Rashba spin splitting is helpful for applications in spintronics. The spin split bands help to generate spin-polarized current.

5.3.3 Spin splitting in SnXY/WXY heterostructures

Heterostructures constructed using J-SnXY and J-WXY monolayers have X-Y interface. The X-Y interface is selected based on stability compared to X-X and Y-Y interfaces. Within the X-Y interface, each heterostructure shows three possible stable stackings. Among them, one stacking with the most stable energy configuration is considered in this work for further study. The binding energy of HSs is calculated using the relation [302]

$$E_b = (E_{SnXY/WXY} - E_{SnXY} - E_{WXY})/N \tag{5.11}$$

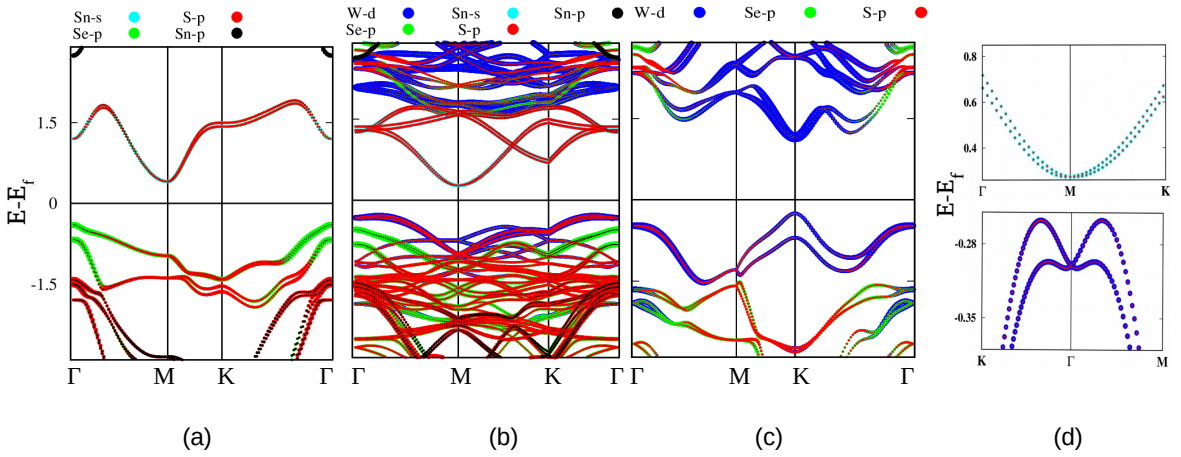

Figure 5.6: Orbital projected PBE band structure of Janus monolayres and heterostructures. (a) SnSSe (b) SnSSe/WSSe (c) WSSe with spin orbit coupling. Fermi energy is set to zero.

where $E_{SnXY/WXY}$, E_{SnXY} , and E_{WXY} are the total energies of the fully relaxed J-SnXY/WXY heterostructure, isolated $\sqrt{3}\times\sqrt{3}\times1$ supercell of J-SnXY monolayer rotated by 30° and isolated 2×2×1 supercell of J-WXY monolayer. N is the total number of atoms in the heterostructure. J-SnSSe/WSSe HS has $E_{SnSSe/WSSe}$ = -134.58 eV, E_{SnXY} = -39.41 eV, E_{WXY} = -94.51 eV and N = 21. Hence E_b is -31.43 meV per atom. Similarly, E_b for the J-SnSTe/WSTe and J-SnSeTe/WSeTe HSs are -79.52 meV and -93.05 meV per atom, respectively. The negative binding energy values confirm that the HSs are stable enough to study the electronic properties.

The crystal structure of SnSSe/WSSe HS is shown in Figure 5.5 (a). S-atom of the J-SnSSe layer is situated in the middle of the ring formed by both J-SnSSe and J-WSSe layers. The S-atom of the J-WSSe layer is facing the Se-atom of the J-SnSSe layer. After the complete relaxation, the interlayer distance is fixed to 3.29 Å. The planar average of the electrostatic potential energy and the charge density are shown in black and green curves in Figure 5.5 (b). The interface has two different chalcogen atoms with unequal electronegativities. We calculated the charge density difference using $\delta\rho = \rho_{SnSSe/WSSe}$-$\rho_{SnSSe}$-$\rho_{SnSSe}$, here $\rho_{SnSSe/WSSe}$,

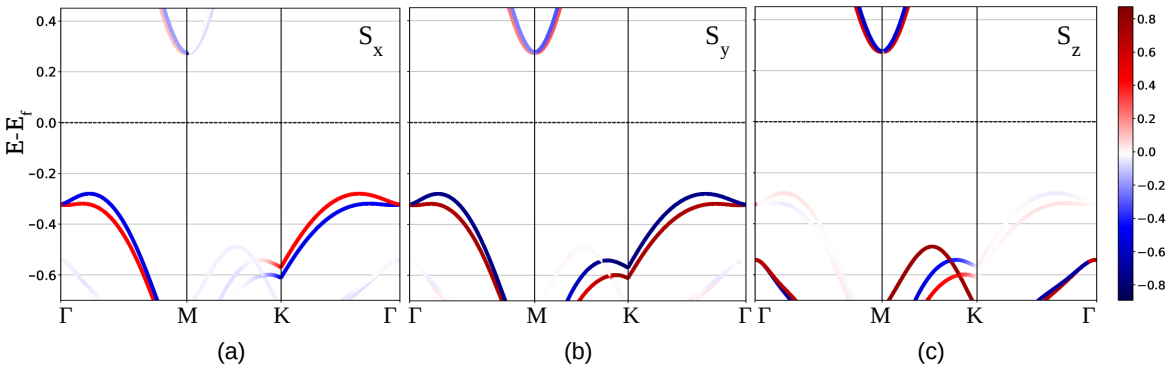

Figure 5.7: Spin projected PBE band structure of SnSSe/WSSe heterostructure included with soc. (a) S_x, (b) S_y and (c) S_z are the spin projection components along x,y (in-plane) and z (out-of-plane) directions respectively.

ρ_{SnSSe} and ρ_{SnSSe} represent the total charge densities of J-SnSSe/WSSe HS, J-SnSSe and J-WSSe layers, respectively. $\delta\rho$ is plotted in Figure 5.5 (c), which shows that the charge has transferred from J-SnSSe layer to J-WSSe layer. Hence a potential drop of 6.27 eV is built across the Se-S interface, which produces an internal electric field that flows from Se-atom to S-atom. This is emphasized by the greater charge density on the S-atom of J-WSSe layer than the Se-atom of J-SnSSe layer shown in a green curve. The interface has charge accumulation and depletion shown in Figure 5.15 (a), indicates that J-SnSSe and J-WSSe layers undergo strong interaction while stacking on each other and hence the band gap reduces to 0.55 eV. The work function of each layer is calculated using $\Phi = E_{Vac} - E_{Fermi}$. Φ for J-SnSSe and J-WSSe layers are 5.51 and 4.71 eV, respectively, and their difference is $\Delta\Phi$ = 0.80 eV. The orbitals projected PBE band structure with soc, and vdw interaction is shown in Figure 5.6 (b).

Figure 5.7 (a) and (b) show that the in-plane spin projection components have the spin split bands at Γ-point along Γ-M and Γ-K paths. This indicates that spin-splitting at Γ-point is in-plane. Also, we calculated the spin texture of spin split bands at Γ-point around E = E_f - 0.4 eV. In Figure 5.8 (a) and (b), the concentric

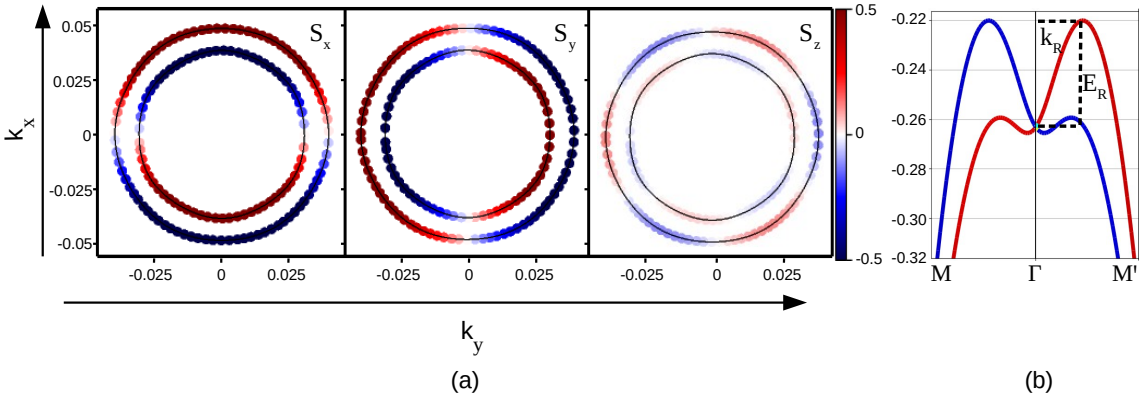

Figure 5.8: In SnSSe/WSSe HS (a) spin texture of Rashba spin split bands at Γ-point, calculated around E = E_f - 0.4 eV. S_x, S_y and S_z are the spin projection components along x,y (in-plane) and z (out-of-plane) directions, respectively. (b) Pure Rashba spin-splitting at Γ-point, showing spin splitting energy E_R and wavenumber difference k_R.

circles represent the inner and outer branches of the spin split bands at Γ-point (figure). Within each circle, one can observe that spin orientation is changing with k_x and k_y directions. The significant spin densities are observed in in-plane S_x and S_y components, which are of 90° phase shift. The spin orientation is different along the out-of-plane S_z component, and spins are almost absent. The spin-projected band structure and spin textures confirm that the spin-splitting at Γ-point is purely RSS. Compared with the individual SnSSe and WSSe layers, the spin splitting energy at Γ-point has increased in the SnSSe/WSSe heterostructure. Along Γ-M path E_R^{G-M} = 42.96 meV (> 25 meV), k_R^{G-M} = 0.122 Å^{-1} (L = 1.29 nm) and α_R^{G-M} = 0.704 eVÅ. Along Γ-K path, E_R^{G-K} = 42.91 meV (> 25 meV), k_R^{G-K} = 0.126 Å^{-1} (L = 1.25 nm) and α_R^{G-K} = 0.681 eVÅ. The splitting at Γ-point is mainly caused by the W-*d* orbital and S-*p* orbitals. In the WSSe layer, though the splitting at Γ-point is caused by the W-atom, it is tiny, about 2.69 meV (Figure 5.6 (c)). It has enhanced to about 43 meV due to the presence of the SnSSe layer in SnSSe/WSSe HS. Bands along Γ-M and Γ-K path just below the Fermi level are pushed by the Se-atom of the SnSSe

layer. Whereas the corresponding band along Γ-M and Γ-K path in the WSSe layer is not affected by other bands in the energy range 0 up to -1.5 eV, as there are not many bands below the Fermi level. The stronger interaction between the two layers forms a denser valence band in the HS, which causes the enhanced spin splitting at Γ-point and decreases the band gap. The spin-splitting at Γ-point and M-points are shown in the lower and upper panels of Figure 5.6 (d). As shown in Figure 5.7 (c), the spin-splitting along M-point is Rashba-like spin splitting which originated mainly from Sn-*s* orbital. In this semiconductor heterostructure, spin splitting is observed at both the band maxima. At the VBM (Γ-point), the spin splitting is purely RSS, whereas, at CBM (M-point), it is Rashba-like spin splitting (along M-Γ and M-K).

The spin splitting in a semiconductor material has an advantage in optoelectronic applications. The effective mass of electron at CBM and hole at VBM along k_x and k_y-directions are $m_e^*(k_x) = 0.03\ m_0$, $m_e^*(k_y) = 0.013\ m_0$ and $m_h^*(k_x) = 0.081\ m_0$, $m_h^*(k_y) = 0.122\ m_0$, respectively. Here m_0 is the rest mass of the electron. The relative ratio of effective masses along k_x and k_y-directions are indicated as variance which is defined as [303, 304]

$$D_{k_x} = \frac{m_h^*(k_x)}{m_e^*(k_x)}, D_{k_y} = \frac{m_h^*(k_y)}{m_e^*(k_y)} \tag{5.12}$$

Here D indicates the ease of electron and hole recombination. The value of D closer to 1 indicates similar electron and hole mass, which implies similar carrier mobility. Hence carrier recombination is easy. Thus, a D value closer to 1 means high recombination in the system. On the other hand, a substantial variation in the carrier effective masses results from a significant difference in carrier mobilities. This indicates the greater probability of separating electrons and holes in the system, thereby lowering carrier recombination. Hence a greater variance of D from 1

shows the low recombination in the system. In SnSSe/WSSe HS, the value of D_{k_x} = 2.7 and D_{k_y} = 9.39 leads the greater variance in the carrier mobilities. This may be because the electron mass (CBM) and hole mass (VBM) come from two separate layers, SnSSe and WSSe, respectively. However, when spin-splitting is considered, the new optical selection rules [305, 306] obstruct the direct recombination of electron and hole at the band maxima. In this way, spin split bands suppress the carrier recombination in the system. This is one of the advantages of pure Rashba and Rashba-like spin splitting in SnSSe/WSSe HS. Therefore, SnSSe/WSSe HS is a viable candidate for separating the electron and holes instead of allowing them to recombine. Thus SnSSe/WSSe HS could be a good candidate for building solar cells.

The crystal structure of SnSTe/WSTe(SnSeTe/WSeTe) HS is shown in Figure 5.9 (a) (5.12 (a)). In SnSTe/WSTe(SnSeTe/WSeTe) HS, the Sn-atom is situated at the center of the hexagonal ring formed by the WSTe (WSeTe) layer. Figure 5.9 (b)(5.12 (b)) shows the planar average of the electrostatic potential energy in the black line and the planar average of the charge density in the green line. Greater charge density on S-atom (SnSTe) than on Te-atom (WSTe), and the Bader charge analysis indicates that a charge of about 0.017 e has transferred from WSTe to the SnSTe layer in the heterostructure. The internal electric field directs from Te-atom (WSTe) to S-atom(SnSTe) across the Te-S interface. Whereas in SnSeTe/WSeTe HS, the charge density on Se-atom (WSeTe) is greater than on Te-atom (SnSeTe), indicating that a charge of about 0.01 e has transferred from SnSeTe to J-WSeTe layer and the E_{int} flows from Te-atom (SnSeTe) to Se-atom (WSeTe) across the Se-Te interface. The charge density difference shown in Figure 5.9 (c) (5.12 (c)) also supports these findings. The potential drop across the Te-S(Se-Te) interface in SnSTe/WSTe(SnSeTe/WSeTe) HS is 5.39(4.09) eV. The work function of SnSTe(SnSeTe) and WSTe(WSeTe) layers is 4.87(5.25) and 5.52(4.40) eV, respectively and $\Delta\Phi$ is

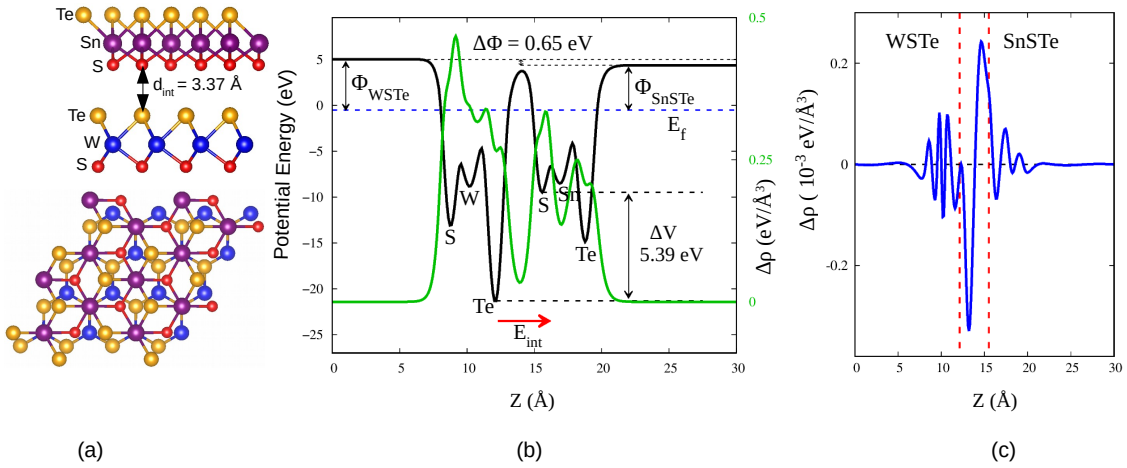

Figure 5.9: For the SnSTe/WSTe HS crystal structure (side and top view) (a), planar average of the electrostatic potential energy is shown in black line and planar average of the charge density is shown in green line (c). Here the Fermi energy is indicated by blue dashed line. Internal electric field E_{int} points from Te to S across S-Te interface, shown in red arrow. Planar average of the charge density difference of the HS is shown in blue line (d),the space between the two red dashed lines is the interface formed by the SnSTe and WSTe layers.

0.65(0.85) eV.

The J-SnSTe/WSTe and J-SnSeTe/WSeTe HSs are metals as shown by the PBE band structures Figure 5.10 (b) (5.13 (b)). The metallicity originates from the J-SnSTe and J-SnSeTe layers. The splitting at Γ-point in J-SnSTe/WSTe HS mainly comes from the *d*-orbital of W-atom and *p*-orbital of S-atom, which is absent in J-SnSeTe/WSeTe HS. The spin-splitting at M-point in both the HSs is mainly caused by the *s*-orbital of S-atom, and it has a less and equal contribution from the *p*-orbital of S (Se) and Te-atoms. As shown in Figure 5.11 and 5.14 at M-point (Γ-M-K path), the spin-splitting has both S_y and S_z components, indicates mixed Rashba and Rashba-like spin-splittings. Whereas at Γ-point (K-Γ-M path), only in-plane components present denotes pure RSS. In J-SnSTe/WSTe HS at M-point along M-Γ and M-K path, the splitting energy is 17.72 and 15.27 meV, with a splitting strength β_{R-like} of 1.303 and 0.934 eVÅ, respectively. The β_{R-like} is greater than α_R along

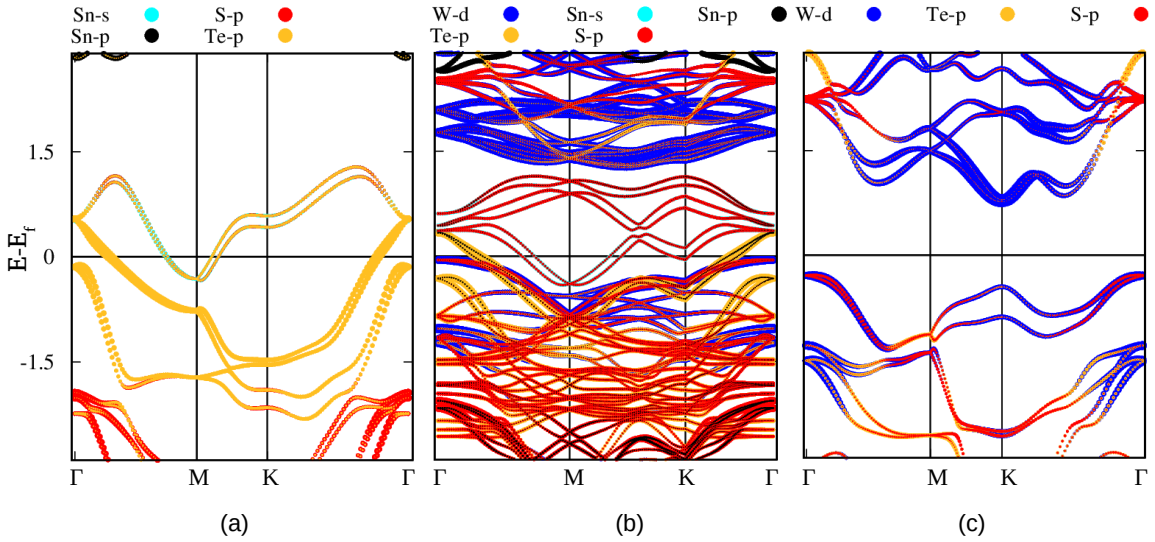

Figure 5.10: Orbital projected PBE band structure of Janus monolayres and heterostructures. (a) SnSTe (b) SnSTe/WSTe (c) WSTe with spin orbit coupling. Fermi energy is set to zero.

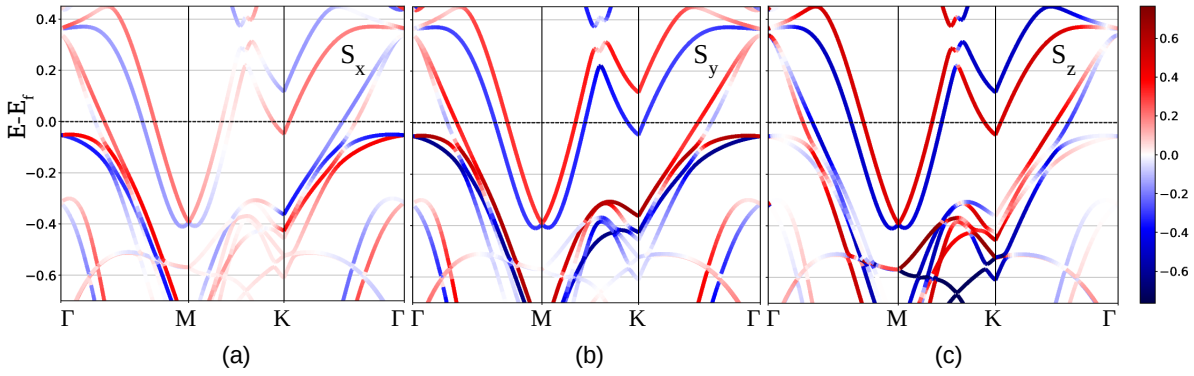

Figure 5.11: Spin projected PBE band structure of SnSTe/WSTe heterostructure included with soc. (a) S_x, (b) S_y and (c) S_z are the spin projection components along x,y (in-plane) and z (out-of-plane) directions respectively.

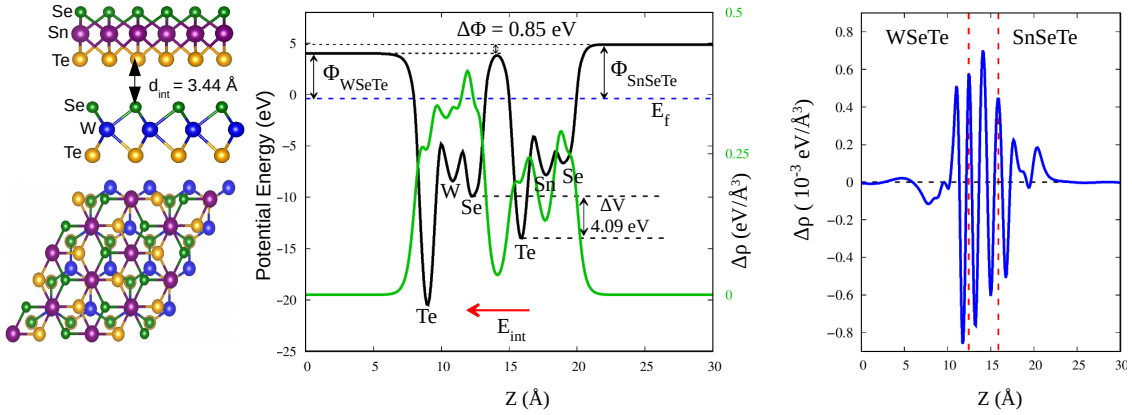

Figure 5.12: For the SnSeTe/WSeTe HS crystal structure (side and top view) (a), planar average of the electrostatic potential energy is shown in black line and planar average of the charge density is shown in green line (c). Here the Fermi energy is indicated by blue dashed line. Internal electric field E_{int} points from Te to Se across Se-Te interface, shown in red arrow. Planar average of the charge density difference of the HS is shown in blue line (d),the space between the two red dashed lines is the interface formed by the SnSeTe and WSeTe layers.

Γ-M and Γ-K path as showmn in Table 5.2. In J-SnSeTe/WSeTe HS along M-Γ and M-K path, the splitting energy is 10.74 and 9.38 meV, with β_{R-like} of 1.193 and 0.788 eVÅ, respectively.

Out of three heterostructures created using J-SnXY and J-WXY monolayers, only SnSSe/WSSe HS is a semiconductor with strong interaction between the individual layers. Pure RSS and Rashba-like spin-splitting are observed, with Rashba spin-splitting energy greater than room temperature energy. Including this, the carrier recombination is suppressed in this heterostructure. This also adds up and makes the heterostructure a viable candidate for optoelectronic and spintronic device applications.

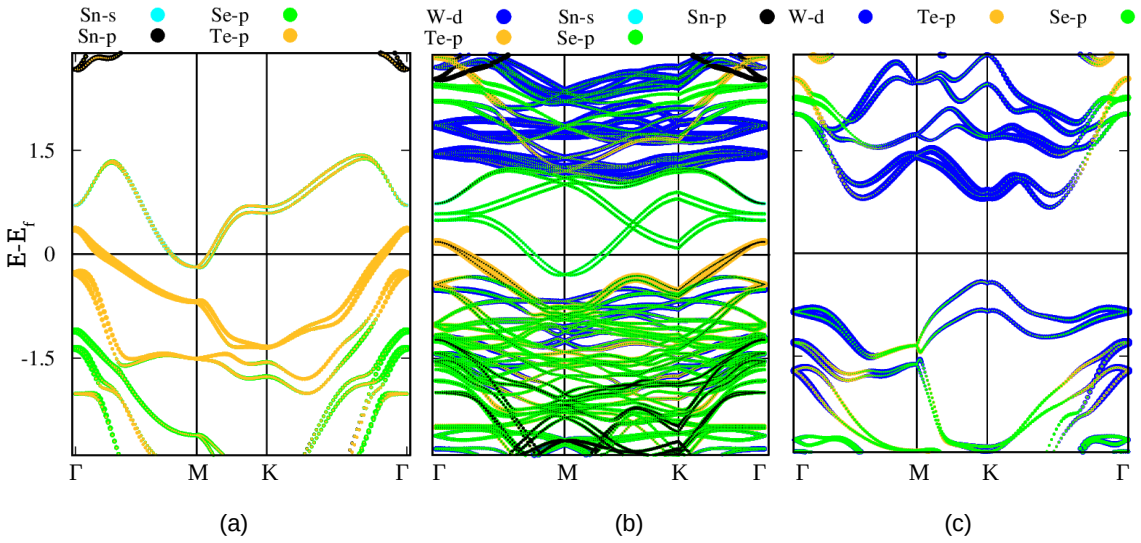

Figure 5.13: Orbital projected PBE band structure of Janus monolayres and heterostructures. (a) SnSeTe (b) SnSeTe/WSeTe (c) WSeTe with spin orbit coupling. Fermi energy is set to zero.

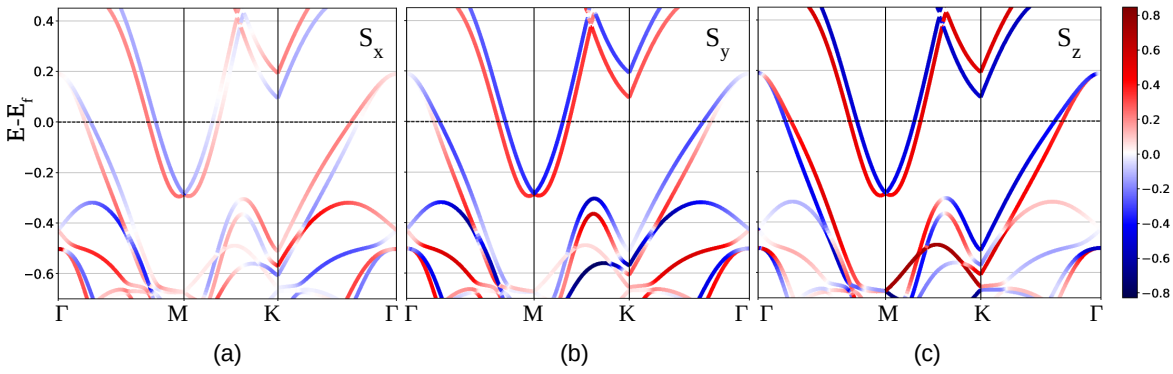

Figure 5.14: Spin projected PBE band structure of SnSeTe/WSeTe heterostructure included with soc. (a) S_x, (b) S_y and (c) S_z are the spin projection components along x,y (in-plane) and z (out-of-plane) directions respectively.

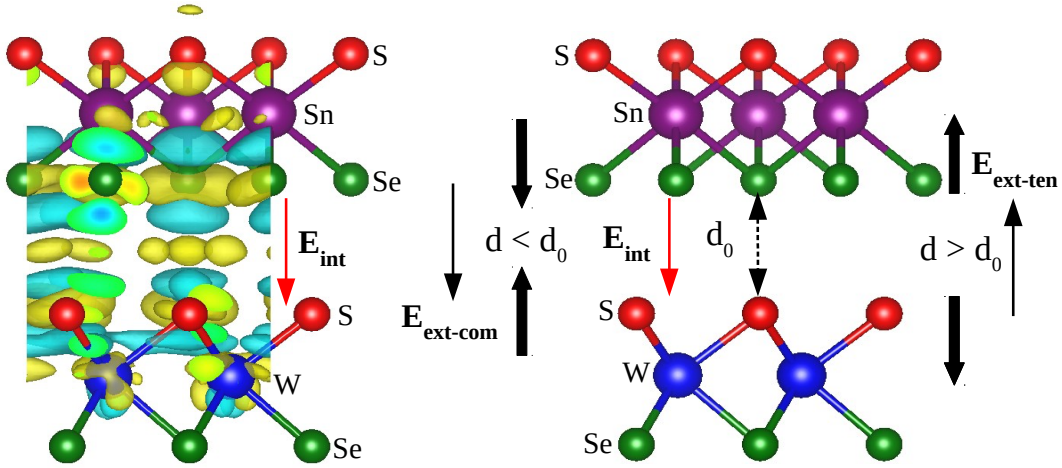

Figure 5.15: (a) Charge density difference in SnSSe/WSSe HS, yellow and cyan isosurfaces indicate the charge accumulation and depletion regions when the HS is at equilibrium. The direction of internal electric field is shown in red arrow. (b) Schematic diagram showing the compressive and tensile strain applications on SnSSe/WSSe HS. $E_{ext-com}$ and $E_{ext-ten}$ are the external electric field induced by the compressive and tensile strains, their directions are shown in black arrows.

5.3.4 Effect of vertical strain on SnSSe/WSSe HS

The application of vertical strain has significant consequences on the electronic properties of semiconductor heterostructure. Here the primary focus is to apply the vertical strain on semiconductor SnSSe/WSSe HS and study the effect on electronic properties. The relaxed interlayer distance we fixed to the heterostructure is 3.29 Å. This distance is increased and decreased. This is considered a tensile and compressive strain defined as $\epsilon = d_0\text{-}d/d_0$, here d_0 and d are the equilibrium and deformed interlayer distances, respectively [307]. The schematic diagram showing the application of vertical strain on SnSSe/WSSe HS is shown in Figure 5.15 (b). We apply about 12% compressive and tensile strain. To confirm the stability of the heterostructure, first, we calculated the binding energy of SnSSe/WSSe HS upon strain applications. Figure 5.16 shows the binding energy and band gap as a function of applied strain. The negative and positive strains represent the

compressive and tensile strains, respectively. The negative binding energy values suggest that the HS is stable and remains with similar stacking till 12% of vertical strain. With compressive strain band gap of the HS decreases and increases with the tensile strain. As we have observed the trend of band gap variation with strain, the compressive strain causes greater interactions between the layers and decreases the band gap. With this, the pure Rashba spin splitting at Γ-point (VBM) also enhances along Γ-K and Γ-M path, as shown in Figure 5.17 (a) and (b). For -5.31 %, E_g = 0.52 eV, E_R = 56.31 meV and k_R = 0.1418 $Å^{-1}$, L = 1.11 nm, α_R = 0.794 eVÅ. For -10.39 % strain, the HS has a semiconducting gap of 0.47 eV with E_R = 72.20 meV and k_R = 0.1512 $Å^{-1}$, L = 1.04 nm, α_R = 0.96 eVÅ. For -12.8% E_g = 0.44 eV, E_R = 80.8 meV and k_R = 0.1513 $Å^{-1}$, L = 1.04 nm, α_R = 1.07 eVÅ. These values indicate that up to -12.79% strain, the heterostructure is suitable to operate at room temperature, with a channel length of about 1 nm. Even if we consider -10% strained heterostructure, it is good enough for spintronic device applications at room temperature.

The compressive strain enhances the Rashba splitting energy and parameter, which are decreased by the tensile strain. We also have observed that the heterostructure remains a semiconductor throughout the strain application. Figure 5.15 (b) depicts that with compressive strain, the interlayer distance decreases, and hence the interaction between the layers increases, thereby reducing the band gap. The external electric field driven by the compressive strain is parallel to the built-in or internal electric field across the Se-S interface of the heterostructure. This increases the magnitude of the net electric field, and hence there is an increase in Rashba spin splitting. This is also evident by the tensile strain, which decreases the Rashba spin-splitting due to the opposite orientation of the external electric field applied by the tensile strain to the internal field across the interface. The metallicity of SnSTe/WSTe and SnSeTe/WSeTe heterostructures remains the same with

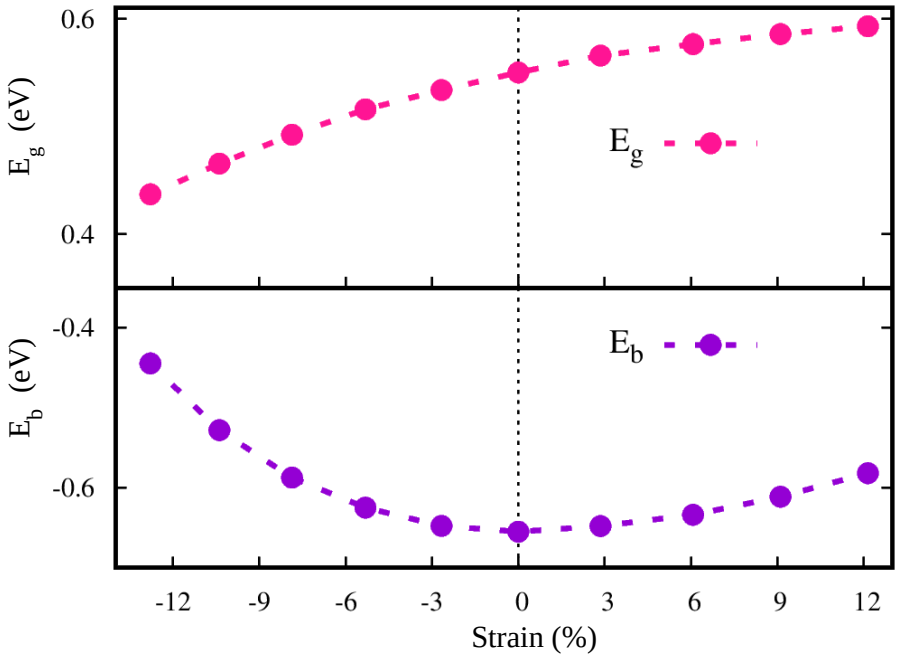

Figure 5.16: Band gap E_g and binding energy E_b of SnSSe/WSSe HS under compressive and tensile strain applications.

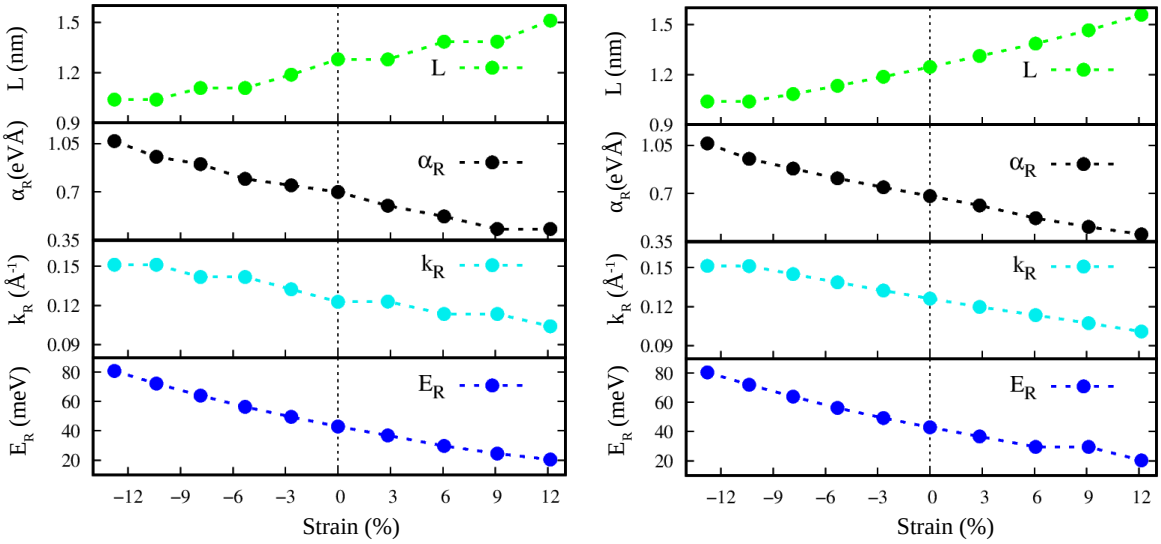

Figure 5.17: Effect of vertical strain on Rashba splitting energy E_R, wavenumber difference k_R, Rashba parameter α_R and spin-precession length L in SnSSe/WSSe HS, at Γ-point along (a) Γ-M and (b) Γ-K path. Negative and positive strain values represent compressive and tensile strains, respectively.

the vertical strain.

5.4 Conclusion

In this chapter, we have discussed the Rashba and Rashba-like spin-splitting J-SnXY monolayers and their heterostructures with J-WXY monolayers. The strength of the spin-splitting in SnXY/WXY heterostructures enhances with the size of the chalcogen atom. The heterostructures with the Te environment are metals. The SnSSe/WSSe heterostructure is a semiconductor with pure RSS at Γ-point. It shows significant variation in the effective masses of carriers which leads to suppressing the carrier recombination. It has only spin-splitting bands near the Fermi level, with a Rashba spin-splitting energy of about 43 meV and a parameter of 0.7 eVÅ. We found a trend of heterostructure on strain applications. The band gap increases with tensile strain and decreases with compressive strain. The Rashba spin-splitting and strength increase with compressive strain. 12.8% of compressive strain application enhances the Rashba splitting energy to about 80.8 meV and Rashba parameter of 1.07 eVÅ. All these findings emphasize the importance of the SnSSe/WSSe heterostructure for future optoelectronic and spintronic applications.

CHAPTER 6

SUMMARY AND FUTURE OUTLOOK

In order to get suitable materials for optoelectronic and spintronic device applications, we predicted a variety of layered materials along with their vertical heterostructures. In this thesis, we computationally presented the structural properties, electronic structure, optical properties such as optical absorption, excitons, and their binding energy, magnetism, magnetic interaction, and spin-splitting leading to the Rashba effect in the layered 2D materials.

Computational methods are highly recommended for real experiments. The accuracy of the calculation depends on which approximation is considered. Finding experimentally matchable or true band gaps in semiconducting systems is a challenge for theoretical methods. Regarding this, we tried less popular but highly promising calculations involving dielectric-dependent hybrid functionals. The performance of hybrid functionals depends on the amount of mixing parameter α incorporated in the exchange energy. α decides the amount of Hartree-Fock and semilocal exchange energies involved in the calculation. We started with α = 25%, and for the next iterations, α is taken as the inverse of the static dielectric constant of the material, ${\epsilon_\infty}^{-1}$. The self-consistent steps are continued till the dielectric constant and band gap converge. The band gap converges when $\epsilon_\infty <$ 0.01. Using this approach, we calculated the band gap of the sensitive TiS_2 system. The TiS_2 system shows an inconsistent band gap for various experimental methods. When the DDHF approach is applied, we obtain a range of band gap values within which the ARPES band gap exists. In addition to assisting in obtaining the experimental band gap, the approach also provides the system with a range of pos-

sible band gaps. We have successfully reproduced the true band gap of bulk and monolayer SnS_2 crystal. The non-magnetic SnS_2 system is substituted by $3d$ transition metal atoms. Their experimental band gaps are unknown; hence, we applied DDHF calculations. We iteratively produced a range of band gap values till its convergence. For each doped system in bulk and monolayer limit, we presented upper and lower band gap values along with the converged band gap. The true or experimental band gap is expected to be in this range. We firmly believe that this approach aids experimentalists in anticipating potential applications in the electronic and nanoelectronic fields. The outcomes demonstrated that the DDHF approach is an excellent prediction of the experimental band gap.

We have investigated the optical properties of doped systems to comprehend their optical response. The optical absorption spectra reveal the red shift in the doped system's energy. Compared with the pure SnS_2, the doped semiconductors have enhanced absorption of about 10^5 cm^{-1}. The direct electronic transition is observed in V, Mn, and Fe-doped systems. Hence these semiconductors are strongly recommended for optical absorber materials. The absorption coefficient, reflectivity, and refractivity are greatly enhanced in the low-energy region for all the doped systems. This shows the effective utilization of solar energy. Understanding excitons and their binding energy are very important for optoelectronic applications. The excitonic properties result in heavier binding energy in the monolayer than in the bulk environment. These results emphasize the importance of transition metal doping on SnS_2 crystal for optoelectronic device applications.

The spintronics devices demand spin-polarized materials for the spin current generation. We continued our work to understand the magnetism and possible magnetic interactions happening in transition metal doped monolayer SnS_2. The formation energy calculation reveals that the Sn-poor condition energetically stabilizes the doped compounds. The negative binding energy values confirm that

the two impurities interact magnetically within the monolayer SnS_2. We observed that the double V, Cr, Mn, and Zn-doped ML-SnS_2 are ferromagnetic semiconductors with the magnetic moment of 2, 4, 6, and 2.56 μ_B, respectively. Further Fe and Co-doped ML-SnS_2 are ferromagnetic half-metals with the magnetic moment of 4 and 2 μ_B, respectively. Magnetic half-metals exhibit 100% spin polarization. Hence they are suitable spin injector materials. The ferromagnetic semiconductors and ferromagnetic half-metals induced by $3d$ transition metal doping on 2D-SnS_2 are viable materials for the spin-polarized current generation, spin injection, and other spintronic device applications.

Janus transition metal dichalcogenide monolayers have shown considerable Rashba spin splitting. In this thesis, we have studied the Janus tin dichalcogenide monolayers. J-SnSSe is a semiconductor, and J-SnSTe and J-SnSeTe are metals. These Janus monolayers have lost the out-of-plane inversion symmetry due to two chalcogen atoms with different electronegativities. The Rashba and Rashba-like spin splitting in these monolayers increase with the size of the chalcogen atom. We referred to Rashba-like splitting to reveal the existence of out-of-plane spin-polarization along in-plane momentum direction(M-K).

Further, the SnSSe/WSSe heterostructure is a semiconductor that exhibits only the spin-splitting bands near the Fermi level. It shows a room temperature Rashba splitting energy, E_R of about 43 meV and Rashba parameter α_R of about 0.7 eVÅ. Further, we noticed that the heterostructure has a greater variance of 9.37 in the effective masses of carriers. This leads to a more significant variance in carrier mobilities and substantially suppresses the carrier recombination in the system. Therefore, J-SnSSe/WSSe heterostructure is a feasible candidate for separating the electron and holes instead of allowing them to recombine. We also have studied the effect of vertical strain on Rashba spin splitting. With the compressive strain, the band gap decreases with an increase in the Rashba splitting energy and parameter,

whereas with tensile strain, the band gap increases, and the Rashba splitting decreases. The heterostructure retains negative binding energy for the applied strain of 10%, indicating its stability. We have observed a significant enhancement in the E_R and α_R to 72.2 meV and 0.96 eVÅ, respectively, for the vertical compressive strain of about 10%. In this case, $k_R = 0.1513$ Å^{-1} implies a channel length of about 1.04 nm. These observations confirm that SnSSe/WSSe heterostructure can operate at room temperature with a small channel length and easy modulation of the Rashba parameter. This way, SnSSe/WSSe heterostructure meets all the requirements for a good Rashba material. From all these predictions, the SnSSe/WSSe heterostructure is a productive material for spintronic device applications.

Our study investigated appropriate materials for electronic, optoelectronic, and spintronic device applications. Therefore experimental efforts are needed to design the potential devices from these materials.

BIBLIOGRAPHY

[1] A. K. Geim and K. S. Novoselov. The rise of graphene. *Nature Materials*, 6(3):183–191, Mar 2007.

[2] K Novoselov. Room-temperature quantum hall effect in graphene. science. *Science*, 315, 2007.

[3] Xinxin Yang, Andrei Vorobiev, Andrey Generalov, Michael A. Andersson, and Jan Stake. A flexible graphene terahertz detector. *Applied Physics Letters*, 111(2):021102, 2017.

[4] Jie Yang, PingAn Hu, and Gui Yu. Perspective of graphene-based electronic devices: Graphene synthesis and diverse applications. *APL Materials*, 7(2):020901, 2019.

[5] Xiao-Guang Gao, Ling-Xiao Cheng, Wen-Shuai Jiang, Xiao-Kuan Li, and Fei Xing. Graphene and its derivatives-based optical sensors. *Frontiers in Chemistry*, 9, 2021.

[6] Hikari Kitadai, Meng Yuan, Yongqiang Ma, and Xi Ling. Graphene-based environmental sensors: Electrical and optical devices. *Molecules*, 26(8), 2021.

[7] Syed Farooq Adil, Mujeeb Khan, and Dharmalingam Kalpana. 7 - graphene-based nanomaterials for solar cells. In Zhiqun Lin, Meidan Ye, and Mengye Wang, editors, *Multifunctional Photocatalytic Materials for Energy*, Woodhead Publishing in Materials, pages 127–152. Woodhead Publishing, 2018.

[8] Xuegong Yu, Lifei Yang, Qingmin Lv, Mingsheng Xu, Hongzheng Chen, and

Deren Yang. The enhanced efficiency of graphenesilicon solar cells by electric field doping. *Nanoscale*, 7:7072–7077, 2015.

[9] Siyuan Luo, Yanan Wang, Xin Tong, and Zhiming Wang. Graphene-based optical modulators. *Nanoscale Research Letters*, 10(1):199, Apr 2015.

[10] Shoma Nakamura, Kota Sekiya, Shinichiro Matano, Yui Shimura, Yuuki Nakade, Kenta Nakagawa, Yasuaki Monnai, and Hideyuki Maki. High-speed and on-chip optical switch based on a graphene microheater. *ACS Nano*, 16(2):2690–2698, 2022.

[11] Marco A. Giambra, Vaidotas Mieikis, Sergio Pezzini, Simone Marconi, Alberto Montanaro, Filippo Fabbri, Vito Sorianello, Andrea C. Ferrari, Camilla Coletti, and Marco Romagnoli. Wafer-scale integration of graphene-based photonic devices. *ACS Nano*, 15(2):3171–3187, 2021.

[12] Kuldeep Rana, Seong Dae Kim, and Jong-Hyun Ahn. Additive-free thick graphene film as an anode material for flexible lithium-ion batteries. *Nanoscale*, 7:7065–7071, 2015.

[13] Syed Farooq Adil, Mujeeb Khan, and Dharmalingam Kalpana. 7 - graphene-based nanomaterials for solar cells. In Zhiqun Lin, Meidan Ye, and Mengye Wang, editors, *Multifunctional Photocatalytic Materials for Energy*, Woodhead Publishing in Materials, pages 127–152. Woodhead Publishing, 2018.

[14] Jiang Zhou, Ying Huang, Xiehong Cao, Bo Ouyang, Wenping Sun, Chaoliang Tan, Yu Zhang, Qinglang Ma, Shuquan Liang, Qingyu Yan, and Hua Zhang. Two-dimensional nico2o4 nanosheet-coated three-dimensional graphene networks for high-rate, long-cycle-life supercapacitors. *Nanoscale*, 7:7035–7039, 2015.

[15] Longfei Wu, Xinsheng Wang, Yupeng Sun, Yang Liu, and Jinghong Li. Flawed moo2 belts transformed from moo3 on a graphene template for the hydrogen evolution reaction. *Nanoscale*, 7:7040–7044, 2015.

[16] Zi-Rong Tang, Yanhui Zhang, Nan Zhang, and Yi-Jun Xu. New insight into the enhanced visible light photocatalytic activity over boron-doped reduced graphene oxide. *Nanoscale*, 7:7030–7034, 2015.

[17] Nikolaos Tombros, Csaba Jozsa, Mihaita Popinciuc, Harry T. Jonkman, and Bart J. van Wees. Electronic spin transport and spin precession in single graphene layers at room temperature. *Nature*, 448(7153):571–574, Aug 2007.

[18] Wei Han, K. Pi, K. M. McCreary, Yan Li, Jared J. I. Wong, A. G. Swartz, and R. K. Kawakami. Tunneling spin injection into single layer graphene. *Phys. Rev. Lett.*, 105:167202, Oct 2010.

[19] Sajedeh Manzeli, Dmitry Ovchinnikov, Diego Pasquier, Oleg V. Yazyev, and Andras Kis. 2d transition metal dichalcogenides. *Nature Reviews Materials*, 2(8):17033, Jun 2017.

[20] Roscoe G. Dickinson and Linus Pauling. The crystal structure of molybdenite. *Journal of the American Chemical Society*, 45(6):1466–1471, 1923.

[21] Kin Fai Mak, Changgu Lee, James Hone, Jie Shan, and Tony F. Heinz. Atomically thin mos_2: A new direct-gap semiconductor. *Phys. Rev. Lett.*, 105:136805, Sep 2010.

[22] Wenjuan Zhu, Tony Low, Han Wang, Peide Ye, and Xiangfeng Duan. Nanoscale electronic devices based on transition metal dichalcogenides. *2D Materials*, 6(3):032004, jun 2019.

[23] Qing Hua Wang, Kourosh Kalantar-Zadeh, Andras Kis, Jonathan N Coleman, and Michael S Strano. Electronics and optoelectronics of two-dimensional transition metal dichalcogenides. *Nature Nanotechnology*, 7(11):699–712, nov 2012.

[24] Tania Roy, Mahmut Tosun, Xi Cao, Hui Fang, Der-Hsien Lien, Peida Zhao, Yu-Ze Chen, Yu-Lun Chueh, Jing Guo, and Ali Javey. Dual-gated mos2/wse2 van der waals tunnel diodes and transistors. *ACS Nano*, 9(2):2071–2079, 2015.

[25] Yu-Chuan Lin, Ram Krishna Ghosh, Rafik Addou, Ning Lu, Sarah M. Eichfeld, Hui Zhu, Ming-Yang Li, Xin Peng, Moon J. Kim, Lain-Jong Li, Robert M. Wallace, Suman Datta, and Joshua A. Robinson. Atomically thin resonant tunnel diodes built from synthetic van der waals heterostructures. *Nature Communications*, 6(1):7311, Jun 2015.

[26] Woo Jong Yu, Zheng Li, Hailong Zhou, Yu Chen, Yang Wang, Yu Huang, and Xiangfeng Duan. Vertically stacked multi-heterostructures of layered materials for logic transistors and complementary inverters. *Nature Materials*, 12(3):246–252, Mar 2013.

[27] Daria Krasnozhon, Dominik Lembke, Clemens Nyffeler, Yusuf Leblebici, and Andras Kis. Mos2 transistors operating at gigahertz frequencies. *Nano Letters*, 14(10):5905–5911, 2014.

[28] Rui Cheng, Shan Jiang, Yu Chen, Yuan Liu, Nathan Weiss, Hung-Chieh Cheng, Hao Wu, Yu Huang, and Xiangfeng Duan. Few-layer molybdenum disulfide transistors and circuits for high-speed flexible electronics. *Nat. Commun.*, 5(1):5143, oct 2014.

[29] Hesameddin Ilatikhameneh, Yaohua Tan, Bozidar Novakovic, Gerhard Klimeck, Rajib Rahman, and Joerg Appenzeller. Tunnel field-effect transis-

tors in 2-d transition metal dichalcogenide materials. *IEEE Journal on Exploratory Solid-State Computational Devices and Circuits*, 1:12–18, 2015.

[30] Ram krishna Ghosh and Santanu Mahapatra. Monolayer transition metal dichalcogenide channel-based tunnel transistor. *IEEE Journal of the Electron Devices Society*, 1:175–180, 2013.

[31] Aron Szabo, Steven Koester, and Mathieu Luisier. Ab-initio simulation of van der waals mote2sns2 heterotunneling fets for low-power electronics. *Electron Device Letters, IEEE*, 36:514–516, 05 2015.

[32] Tania Roy, Mahmut Tosun, Mark Hettick, Geun Ho Ahn, Chenming Hu, and Ali Javey. 2d-2d tunneling field-effect transistors using wse2/snse2 heterostructures. *Applied Physics Letters*, 108(8):083111, 2016.

[33] Pratik Agnihotri, Prathamesh Dhakras, and Ji Ung Lee. Bipolar junction transistors in two-dimensional wse2 with large current and photocurrent gains. *Nano Letters*, 16(7):4355–4360, 2016.

[34] Che-Yu Lin, Xiaodan Zhu, Shin-Hung Tsai, Shiao-Po Tsai, Sidong Lei, Yumeng Shi, Lain-Jong Li, Shyh-Jer Huang, Wen-Fa Wu, Wen-Kuan Yeh, Yan-Kuin Su, Kang L. Wang, and Yann-Wen Lan. Atomic-monolayer two-dimensional lateral quasi-heterojunction bipolar transistors with resonant tunneling phenomenon. *ACS Nano*, 11(11):11015–11023, 2017.

[35] Chang-Hung Yu, Ming-Long Fan, Kuan-Chin Yu, Vita Pi-Ho Hu, Pin Su, and Ching-Te Chuang. Evaluation of monolayer and bilayer 2-d transition metal dichalcogenide devices for sram applications. *IEEE Transactions on Electron Devices*, 63:625–630, 2016.

[36] Chaitanya U Kshirsagar, Weichao Xu, Yang Su, Matthew C Robbins, Chris H Kim, and Steven J Koester. Dynamic memory cells using mos2 field-

effect transistors demonstrating femtoampere leakage currents. *ACS nano*, 10(9):84578464, September 2016.

[37] Simone Bertolazzi, Daria Krasnozhon, and Andras Kis. Nonvolatile memory cells based on mos2/graphene heterostructures. *ACS Nano*, 7(4):3246–3252, 2013.

[38] Min Sup Choi, Gwan-Hyoung Lee, Young-Jun Yu, Dae-Yeong Lee, Seung Hwan Lee, Philip Kim, James Hone, and Won Jong Yoo. Controlled charge trapping by molybdenum disulphide and graphene in ultrathin heterostructured memory devices. *Nat. Commun.*, 4(1):1624, 2013.

[39] Alexey Lipatov, Pankaj Sharma, Alexei Gruverman, and Alexander Sinitskii. Optoelectrical molybdenum disulfide (mos2)ferroelectric memories. *ACS Nano*, 9(8):8089–8098, 2015.

[40] Mengwei Si, Pai-Ying Liao, Gang Qiu, Yuqin Duan, and Peide D. Ye. Ferroelectric field-effect transistors based on mos2 and cuinp2s6 two-dimensional van der waals heterostructure. *ACS Nano*, 12(7):6700–6705, 2018.

[41] Kartikey Thakar and Saurabh Lodha. Optoelectronic and photonic devices based on transition metal dichalcogenides. *Materials Research Express*, 7(1):014002, jan 2020.

[42] Yu Huang, Fuwei Zhuge, Junxian Hou, Liang Lv, Peng Luo, Nan Zhou, Lin Gan, and Tianyou Zhai. Van der waals coupled organic molecules with monolayer mos2 for fast response photodetectors with gate-tunable responsivity. *ACS Nano*, 12(4):4062–4073, 2018.

[43] Shiwei Cao, Yanhui Xing, Jun Han, Xin Luo, Wenxing Lv, Weiming Lv, Baoshun Zhang, and Zhongming Zeng. Ultrahigh-photoresponsive uv pho-

todetector based on a bp/res2 heterostructure pn diode. *Nanoscale*, 10:16805–16811, 2018.

[44] Ah-Jin Cho, Seok Daniel Namgung, Hojoong Kim, and Jang-Yeon Kwon. Electric and photovoltaic characteristics of a multi-layer res2/rese2 heterostructure. *APL Materials*, 5(7):076101, 2017.

[45] Mingsheng Long, Erfu Liu, Peng Wang, Anyuan Gao, Hui Xia, Wei Luo, Baigeng Wang, Junwen Zeng, Yajun Fu, Kang Xu, Wei Zhou, Yangyang Lv, Shuhua Yao, Minghui Lu, Yanfeng Chen, Zhenhua Ni, Yumeng You, Xueao Zhang, Shiqiao Qin, Yi Shi, Weida Hu, Dingyu Xing, and Feng Miao. Broadband photovoltaic detectors based on an atomically thin heterostructure. *Nano Letters*, 16(4):2254–2259, 2016.

[46] F Withers, O Del Pozo-Zamudio, A Mishchenko, A P Rooney, A Gholinia, K Watanabe, T Taniguchi, S J Haigh, A K Geim, A I Tartakovskii, and K S Novoselov. Light-emitting diodes by band-structure engineering in van der waals heterostructures. *Nat. Mater.*, 14(3):301–306, mar 2015.

[47] Aleksander A. Tedstone, David J. Lewis, and Paul OBrien. Synthesis, properties, and applications of transition metal-doped layered transition metal dichalcogenides. *Chemistry of Materials*, 28(7):1965–1974, 2016.

[48] Liang Cai, Jingfu He, Qinghua Liu, Tao Yao, Lin Chen, Wensheng Yan, Fengchun Hu, Yong Jiang, Yidong Zhao, Tiandou Hu, Zhihu Sun, and Shiqiang Wei. Vacancy-induced ferromagnetism of mos2 nanosheets. *Journal of the American Chemical Society*, 137(7):2622–2627, 2015.

[49] Yandong Ma, Ying Dai, Meng Guo, Chengwang Niu, Yingtao Zhu, and Baibiao Huang. Evidence of the existence of magnetism in pristine vx2 monolay-

ers (x = s, se) and their strain-induced tunable magnetic properties. *ACS Nano*, 6(2):1695–1701, 2012.

[50] Yungang Zhou, Zhiguo Wang, Ping Yang, Xiaotao Zu, Li Yang, Xin Sun, and Fei Gao. Tensile strain switched ferromagnetism in layered nbs2 and nbse2. *ACS Nano*, 6(11):9727–9736, 2012.

[51] Hongliang Shi, Hui Pan, Yong-Wei Zhang, and Boris I. Yakobson. Strong ferromagnetism in hydrogenated monolayer mos_2 tuned by strain. *Phys. Rev. B*, 88:205305, Nov 2013.

[52] Jiangang He, Kechen Wu, Rongjian Sa, Qiaohong Li, and Yongqin Wei. Magnetic properties of nonmetal atoms absorbed mos2 monolayers. *Applied Physics Letters*, 96(8):082504, 2010.

[53] Daqiang Gao, Shoupeng Shi, Kun Tao, Baorui Xia, and Deshene Xue. Tunable ferromagnetic ordering in mos2 nanosheets with fluorine adsorption. *Nanoscale*, 7:4211–4216, 2015.

[54] ZhongCheng Xiang, Zhong Zhang, XiJin Xu, Qin Zhang, QingBao Wang, and Chengwu Yuan. Room-temperature ferromagnetism in co doped mos2 sheets. *Phys. Chem. Chem. Phys.*, 17:15822–15828, 2015.

[55] Z. Y. Zhu, Y. C. Cheng, and U. Schwingenschlögl. Giant spin-orbit-induced spin splitting in two-dimensional transition-metal dichalcogenide semiconductors. *Phys. Rev. B*, 84:153402, Oct 2011.

[56] Di Xiao, Gui-Bin Liu, Wanxiang Feng, Xiaodong Xu, and Wang Yao. Coupled spin and valley physics in monolayers of mos_2 and other group-vi dichalcogenides. *Phys. Rev. Lett.*, 108:196802, May 2012.

[57] S. Acharya and O. N. Srivastava. Electronic behaviour of sns2 crystals. *physica status solidi (a)*, 65(2):717–723, 1981.

[58] Lee A. Burton, Diego Colombara, Ruben D. Abellon, Ferdinand C. Grozema, Laurence M. Peter, Tom J. Savenije, Gilles Dennler, and Aron Walsh. Synthesis, characterization, and electronic structure of single-crystal sns, sn2s3, and sns2. *Chemistry of Materials*, 25(24):4908–4916, 2013.

[59] Joseph M. Gonzalez and Ivan I. Oleynik. Layer-dependent properties of $\mathbf{sns}_2$ and $\mathbf{snse}_2$ two-dimensional materials. *Phys. Rev. B*, 94:125443, PhysRev.143.536Sep 2016.

[60] X.F. Qian, X.M. Zhang, C. Wang, W.Z. Wang, Y. Xie, and Y.T. Qian. Solvent-thermal preparation of nanocrystalline tin chalcogenide. *Journal of Physics and Chemistry of Solids*, 60(3):415–417, 1999.

[61] Huilan Su, Yi Xie, Yujie Xiong, Peng Gao, and Yitai Qian. Preparation and morphology control of rod-like nanocrystalline tin sulfides via a simple ethanol thermal route. *Journal of Solid State Chemistry*, 161(2):190–196, 2001.

[62] Yujie Ji, Hui Zhang, Xiangyang Ma, Jin Xu, and Deren Yang. Single-crystalline sns2 nano-belts fabricated by a novel hydrothermal method. *Journal of Physics: Condensed Matter*, 15(44):L661, oct 2003.

[63] Qing Li, Yi Ding, Hao Wu, Xianming Liu, and Yitai Qian. Fabrication of layered nanocrystallites sns and -sns2 via a mild solution route. *Materials Research Bulletin*, 37(5):925–932, 2002.

[64] D. Chen, G.-Z. Shen, K.-B. Tang, Y.-K. Liu, and Y.-T. Qian. Aligned sns2 nanotubes fabricated via a template-assisted solvent-relief process. *Applied Physics A*, 77(6):747–749, Nov 2003.

[65] Guozhen Shen, Di Chen, Kaibin Tang, Liying Huang, Yitai Qian, and Guien Zhou. Novel polyol route to nanoscale tin sulfides flaky crystallines. *Inorganic Chemistry Communications*, 6(2):178–180, 2003.

[66] Haviv Grisaru, Oleg Palchik, Aharon Gedanken, Valery Palchik, Michael A. Slifkin, and Arie M. Weiss. Microwave-assisted polyol synthesis of cuinte2 and cuinse2 nanoparticles. *Inorganic Chemistry*, 42(22):7148–7155, 2003.

[67] Babu Ram and Abhishek K. Singh. Strain-induced indirect-to-direct band-gap transition in bulk sns_2. *Phys. Rev. B*, 95:075134, Feb 2017.

[68] Tawinan Cheiwchanchamnangij and Walter R. L. Lambrecht. Quasiparticle band structure calculation of monolayer, bilayer, and bulk mos_2. *Phys. Rev. B*, 85:205302, May 2012.

[69] Falco Hüser, Thomas Olsen, and Kristian S. Thygesen. How dielectric screening in two-dimensional crystals affects the convergence of excited-state calculations: Monolayer mos_2. *Phys. Rev. B*, 88:245309, Dec 2013.

[70] S. Latini, T. Olsen, and K. S. Thygesen. Excitons in van der waals heterostructures: The important role of dielectric screening. *Phys. Rev. B*, 92:245123, Dec 2015.

[71] A. Chaves, J. G. Azadani, Hussain Alsalman, D. R. da Costa, R. Frisenda, A. J. Chaves, Seung Hyun Song, Y. D. Kim, Daowei He, Jiadong Zhou, A. Castellanos-Gomez, F. M. Peeters, Zheng Liu, C. L. Hinkle, Sang-Hyun Oh, Peide D. Ye, Steven J. Koester, Young Hee Lee, Ph. Avouris, Xinran Wang, and Tony Low. Bandgap engineering of two-dimensional semiconductor materials. *npj 2D Materials and Applications*, 4(1):29, Aug 2020.

[72] Yongqing Cai, Gang Zhang, and Yong-Wei Zhang. Layer-dependent band

alignment and work function of few-layer phosphorene. *Scientific Reports*, 4(1):6677, Oct 2014.

[73] Saptarshi Das, Wei Zhang, Marcel Demarteau, Axel Hoffmann, Madan Dubey, and Andreas Roelofs. Tunable transport gap in phosphorene. *Nano Letters*, 14(10):5733–5739, 2014.

[74] Lee A. Burton, Thomas J. Whittles, David Hesp, Wojciech M. Linhart, Jonathan M. Skelton, Bo Hou, Richard F. Webster, Graeme O'Dowd, Christian Reece, David Cherns, David J. Fermin, Tim D. Veal, Vin R. Dhanak, and Aron Walsh. Electronic and optical properties of single crystal sns2: an earth-abundant disulfide photocatalyst. *J. Mater. Chem. A*, 4:1312–1318, 2016.

[75] J.-M. Tarascon and M. Armand. Issues and challenges facing rechargeable lithium batteries. *Nature*, 414(6861):359–367, Nov 2001.

[76] Hong Li, Xuejie Huang, and Liquan Chen. Anodes based on oxide materials for lithium rechargeable batteries11paper presented at the 1997 hawaii solid state ionics meeting (a30). *Solid State Ionics*, 123(1):189–197, 1999.

[77] Toshiyuki Momma, Nobuhiro Shiraishi, Atsuhito Yoshizawa, Tetsuya Osaka, Aharon Gedanken, Junjie Zhu, and Lena Sominski. Sns2 anode for rechargeable lithium battery. *Journal of Power Sources*, 97-98:198–200, 2001. Proceedings of the 10th International Meeting on Lithium Batteries.

[78] T Brousse, S.M Lee, L Pasquereau, D Defives, and D.M Schleich. Composite negative electrodes for lithium ion cells. *Solid State Ionics*, 113-115:51–56, 1998.

[79] Tae-Joon Kim, Dongyeon Son, Jaephil Cho, Byungwoo Park, and Hoseok Yang. Enhanced electrochemical properties of sno2 anode by alpo4 coating. *Electrochimica Acta*, 49(25):4405–4410, 2004.

[80] Taeho Moon, Chunjoong Kim, Sun-Tae Hwang, and Byungwoo Park. Electrochemical properties of disordered-carbon-coated sno2 nanoparticles for li rechargeable batteries. *Electrochemical and Solid-State Letters*, 9(9):A408, jun 2006.

[81] Tae-Joon Kim, Chunjoong Kim, Dongyeon Son, Myungsuk Choi, and Byungwoo Park. Novel sns2-nanosheet anodes for lithium-ion batteries. *Journal of Power Sources*, 167(2):529 – 535, 2007.

[82] Jung-wook Seo, Jung-tak Jang, Seung-won Park, Chunjoong Kim, Byungwoo Park, and Jinwoo Cheon. Two-dimensional sns2 nanoplates with extraordinary high discharge capacity for lithium ion batteries. *Advanced Materials*, 20(22):4269–4273, 2008.

[83] Weidong Shi, Lihua Huo, Haishui Wang, Hongjie Zhang, Jianhui Yang, and Pinghui Wei. Hydrothermal growth and gas sensing property of flower-shaped SnS2 nanostructures. *Nanotechnology*, 17(12):2918–2924, may 2006.

[84] Haoxiang Zhong, Gongzheng Yang, Huawei Song, Qingyu Liao, Hao Cui, Peikang Shen, and Cheng-Xin Wang. Vertically aligned graphene-like sns2 ultrathin nanosheet arrays: Excellent energy storage, catalysis, photoconduction, and field-emitting performances. *The Journal of Physical Chemistry C*, 116(16):9319–9326, 2012.

[85] Debtanu De, John Manongdo, Sean See, Vincent Zhang, Arnold Guloy, and Haibing Peng. High on/off ratio field effect transistors based on exfoliated crystalline SnS2nano-membranes. *Nanotechnology*, 24(2):025202, dec 2012.

[86] H. S. Song, S. L. Li, L. Gao, Y. Xu, K. Ueno, J. Tang, Y. B. Cheng, and K. Tsukagoshi. High-performance top-gated monolayer sns2 field-effect transistors and their integrated logic circuits. *Nanoscale*, 5:9666–9670, 2013.

[87] Jiaxin Wang, Rundong Jia, Qianqian Huang, Chen Pan, Jiadi Zhu, Huimin Wang, Cheng Chen, Yawen Zhang, Yuchao Yang, Haisheng Song, Feng Miao, and Ru Huang. Vertical ws2/sns2 van der waals heterostructure for tunneling transistors. *Scientific Reports*, 8(1):17755, Dec 2018.

[88] Yua A Bychkov and É I Rashba. Properties of a 2d electron gas with lifted spectral degeneracy. *JETP lett*, 39(2):78, 1984.

[89] Martin Gmitra and Jaroslav Fabian. Graphene on transition-metal dichalcogenides: A platform for proximity spin-orbit physics and optospintronics. *Phys. Rev. B*, 92:155403, Oct 2015.

[90] Kyuhwan Lee, Won Seok Yun, and J. D. Lee. Giant rashba-type splitting in molybdenum-driven bands of $mos_2/Bi(111)$ heterostructure. *Phys. Rev. B*, 91:125420, Mar 2015.

[91] Qiming Shao, Guoqiang Yu, Yann-Wen Lan, Yumeng Shi, Ming-Yang Li, Cheng Zheng, Xiaodan Zhu, Lain-Jong Li, Pedram Khalili Amiri, and Kang L. Wang. Strong rashba-edelstein effect-induced spinorbit torques in monolayer transition metal dichalcogenide/ferromagnet bilayers. *Nano Letters*, 16(12):7514–7520, 2016.

[92] Sanfeng Wu, Jason S. Ross, Gui-Bin Liu, Grant Aivazian, Aaron Jones, Zaiyao Fei, Wenguang Zhu, Di Xiao, Wang Yao, David Cobden, and Xiaodong Xu. Electrical tuning of valley magnetic moment through symmetry control in bilayer mos2. *Nature Physics*, 9(3):149–153, Mar 2013.

[93] Hongtao Yuan, Mohammad Saeed Bahramy, Kazuhiro Morimoto, Sanfeng Wu, Kentaro Nomura, Bohm-Jung Yang, Hidekazu Shimotani, Ryuji Suzuki, Minglin Toh, Christian Kloc, Xiaodong Xu, Ryotaro Arita, Naoto Nagaosa,

and Yoshihiro Iwasa. Zeeman-type spin splitting controlled by an electric field. *Nature Physics*, 9(9):563–569, Sep 2013.

[94] Cai Cheng, Jia-Tao Sun, Xiang-Rong Chen, Hui-Xia Fu, and Sheng Meng. Nonlinear rashba spin splitting in transition metal dichalcogenide monolayers. *Nanoscale*, 8:17854–17860, 2016.

[95] Emilie Bruyer, Domenico Di Sante, Paolo Barone, Alessandro Stroppa, Myung-Hwan Whangbo, and Silvia Picozzi. Possibility of combining ferroelectricity and rashba-like spin splitting in monolayers of the 1t-type transition-metal dichalcogenides $mX_2(m = \mathrm{Mo}, \mathrm{W}; x = \mathrm{S}, \mathrm{Se}, \mathrm{Te})$. *Phys. Rev. B*, 94:195402, Nov 2016.

[96] Ang-Yu Lu, Hanyu Zhu, Jun Xiao, Chih-Piao Chuu, Yimo Han, Ming-Hui Chiu, Chia-Chin Cheng, Chih-Wen Yang, Kung-Hwa Wei, Yiming Yang, Yuan Wang, Dimosthenis Sokaras, Dennis Nordlund, Peidong Yang, David A Muller, Mei-Yin Chou, Xiang Zhang, and Lain-Jong Li. Janus monolayers of transition metal dichalcogenides. *Nat. Nanotechnol.*, 12(8):744–749, aug 2017.

[97] Tao Hu, Fanhao Jia, Guodong Zhao, Jiongyao Wu, Alessandro Stroppa, and Wei Ren. Intrinsic and anisotropic rashba spin splitting in janus transition-metal dichalcogenide monolayers. *Phys. Rev. B*, 97:235404, Jun 2018.

[98] Shahid Sattar and J. Andreas Larsson. Tunable electronic properties and large rashba splittings found in few-layer bi2se3/ptse2 van der waals heterostructures. *ACS Applied Electronic Materials*, 2(11):3585–3592, 2020.

[99] Sunny Gupta and Boris I. Yakobson. What dictates rashba splitting in 2d van der waals heterobilayers. *Journal of the American Chemical Society*, 143(9):3503–3508, 2021. PMID: 33625213.

[100] Max Born and Robert Oppenheimer. Zur quantentheorie der molekeln. *Annalen der physik*, 389(20):457–484, 1927.

[101] Max Born, Kun Huang, and M Lax. Dynamical theory of crystal lattices. *American Journal of Physics*, 23(7):474–474, 1955.

[102] Douglas R Hartree. The wave mechanics of an atom with a non-coulomb central field. part i. theory and methods. In *Mathematical Proceedings of the Cambridge Philosophical Society*, volume 24, pages 89–110. Cambridge university press, 1928.

[103] John C Slater. A simplification of the hartree-fock method. *Physical review*, 81(3):385, 1951.

[104] Vladimir Fock. Näherungsmethode zur lösung des quantenmechanischen mehrkörperproblems. *Zeitschrift für Physik*, 61(1-2):126–148, 1930.

[105] Llewellyn H Thomas. The calculation of atomic fields. In *Mathematical proceedings of the Cambridge philosophical society*, volume 23, pages 542–548. Cambridge University Press, 1927.

[106] Enrico Fermi. Statistical method to determine some properties of atoms. *Rend. Accad. Naz. Lincei*, 6(602-607):5, 1927.

[107] P. Hohenberg and W. Kohn. Inhomogeneous electron gas. *Phys. Rev.*, 136:B864–B871, Nov 1964.

[108] W. Kohn. Nobel lecture: Electronic structure of matter—wave functions and density functionals. *Rev. Mod. Phys.*, 71:1253–1266, Oct 1999.

[109] John P. Perdew, Kieron Burke, and Matthias Ernzerhof. Generalized gradient approximation made simple. *Phys. Rev. Lett.*, 77:3865–3868, Oct 1996.

[110] Jochen Heyd, Juan E. Peralta, Gustavo E. Scuseria, and Richard L. Martin. Energy band gaps and lattice parameters evaluated with the heyd-scuseria-ernzerhof screened hybrid functional. *The Journal of Chemical Physics*, 123(17):174101, 2005.

[111] Thomas M. Henderson, Benjamin G. Janesko, and Gustavo E. Scuseria. Generalized gradient approximation model exchange holes for range-separated hybrids. *The Journal of Chemical Physics*, 128(19):194105, 2008.

[112] Jason K. Ellis, Melissa J. Lucero, and Gustavo E. Scuseria. The indirect to direct band gap transition in multilayered mos2 as predicted by screened hybrid density functional theory. *Applied Physics Letters*, 99(26):261908, 2011.

[113] John P. Perdew, Matthias Ernzerhof, and Kieron Burke. Rationale for mixing exact exchange with density functional approximations. *The Journal of Chemical Physics*, 105(22):9982–9985, 1996.

[114] Mark S. Hybertsen and Steven G. Louie. First-principles theory of quasiparticles: Calculation of band gaps in semiconductors and insulators. *Phys. Rev. Lett.*, 55:1418–1421, Sep 1985.

[115] Miguel A. L. Marques, Julien Vidal, Micael J. T. Oliveira, Lucia Reining, and Silvana Botti. Density-based mixing parameter for hybrid functionals. *Phys. Rev. B*, 83:035119, Jan 2011.

[116] Tomomi Shimazaki and Yoshihiro Asai. First principles band structure calculations based on self-consistent screened hartreefock exchange potential. *The Journal of Chemical Physics*, 130(16):164702, 2009.

[117] Stewart J. Clark and John Robertson. Screened exchange density functional applied to solids. *Phys. Rev. B*, 82:085208, Aug 2010.

[118] Tomomi Shimazaki and Takahito Nakajima. Theoretical study of a screened hartreefock exchange potential using position-dependent atomic dielectric constants. *The Journal of Chemical Physics*, 142(7):074109, 2015.

[119] Tomomi Shimazaki and Takahito Nakajima. Dielectric-dependent screened hartreefock exchange potential and slater-formula with coulomb-hole interaction for energy band structure calculations. *The Journal of Chemical Physics*, 141(11):114109, 2014.

[120] Tomomi Shimazaki and Takahito Nakajima. Application of the dielectric-dependent screened exchange potential approach to organic photocell materials. *Phys. Chem. Chem. Phys.*, 18:27554–27563, 2016.

[121] Jonathan H. Skone, Marco Govoni, and Giulia Galli. Self-consistent hybrid functional for condensed systems. *Phys. Rev. B*, 89:195112, May 2014.

[122] Sivan Refaely-Abramson, Sahar Sharifzadeh, Manish Jain, Roi Baer, Jeffrey B. Neaton, and Leeor Kronik. Gap renormalization of molecular crystals from density-functional theory. *Phys. Rev. B*, 88:081204, Aug 2013.

[123] Matteo Gerosa, Carlo Enrico Bottani, Lucia Caramella, Giovanni Onida, Cristiana Di Valentin, and Gianfranco Pacchioni. Electronic structure and phase stability of oxide semiconductors: Performance of dielectric-dependent hybrid functional dft, benchmarked against *gw* band structure calculations and experiments. *Phys. Rev. B*, 91:155201, Apr 2015.

[124] Bhagyashri Bhat. Dielectric-dependent hybrid functional calculations on the electronic band gap of 3*d* transition metal doped sns_2 and their optical properties. *Phys. Rev. B*, 105:195205, May 2022.

[125] K. S. Novoselov, A. K. Geim, S. V. Morozov, D. Jiang, Y. Zhang, S. V. Dubonos,

I. V. Grigorieva, and A. A. Firsov. Electric field effect in atomically thin carbon films. *science*, 306(5696):666–669, 2004.

[126] Hidetaka Kasai, Kasper Tolborg, Mattia Sist, Jiawei Zhang, Venkatesha R. Hathwar, Mette Ø. Filsø, Simone Cenedese, Kunihisa Sugimoto, Jacob Overgaard, Eiji Nishibori, and Bo B. Iversen. X-ray electron density investigation of chemical bonding in van der waals materials. *Nature Materials*, 17(3):249–252, Mar 2018.

[127] P. Chen, Woei Wu Pai, Y.-H. Chan, A. Takayama, C.-Z. Xu, A. Karn, S. Hasegawa, M. Y. Chou, S.-K. Mo, A.-V. Fedorov, and T.-C. Chiang. Emergence of charge density waves and a pseudogap in single-layer tite2. *Nature Communications*, 8(1):516, Sep 2017.

[128] M. N. Gjerding, R. Petersen, T. G. Pedersen, N. A. Mortensen, and K. S. Thygesen. Layered van der waals crystals with hyperbolic light dispersion. *Nature Communications*, 8(1):320, Aug 2017.

[129] Liping Yu, Qimin Yan, and Adrienn Ruzsinszky. Negative poisson's ratio in 1t-type crystalline two-dimensional transition metal dichalcogenides. *Nature Communications*, 8(1):15224, May 2017.

[130] Wenxu Zhang, Zhishuo Huang, Wanli Zhang, and Yanrong Li. Two-dimensional semiconductors with possible high room temperature mobility. *Nano Research*, 7(12):1731–1737, Dec 2014.

[131] Manish Chhowalla, Hyeon Suk Shin, Goki Eda, Lain-Jong Li, Kian Ping Loh, and Hua Zhang. The chemistry of two-dimensional layered transition metal dichalcogenide nanosheets. *Nature Chemistry*, 5(4):263–275, Apr 2013.

[132] Y. I. Joe, X. M. Chen, P. Ghaemi, K. D. Finkelstein, G. A. de la Peña, Y. Gan, J. C. T. Lee, S. Yuan, J. Geck, G. J. MacDougall, T. C. Chiang, S. L. Cooper,

E. Fradkin, and P. Abbamonte. Emergence of charge density wave domain walls above the superconducting dome in 1t-tise2. *Nature Physics*, 10(6):421–425, Jun 2014.

[133] Kai Xu, Zhenxing Wang, Feng Wang, Yun Huang, Fengmei Wang, Lei Yin, Chao Jiang, and Jun He. Ultrasensitive phototransistors based on few-layered hfs2. *Advanced Materials*, 27(47):7881–7887, 2015.

[134] S. Mathias, S. Eich, J. Urbancic, S. Michael, A. V. Carr, S. Emmerich, A. Stange, T. Popmintchev, T. Rohwer, M. Wiesenmayer, A. Ruffing, S. Jakobs, S. Hellmann, P. Matyba, C. Chen, L. Kipp, M. Bauer, H. C. Kapteyn, H. C. Schneider, K. Rossnagel, M. M. Murnane, and M. Aeschlimann. Self-amplified photo-induced gap quenching in a correlated electron material. *Nature Communications*, 7(1):12902, Oct 2016.

[135] Qiyi Zhao, Yaohui Guo, Keyu Si, Zhaoyu Ren, Jintao Bai, and Xinlong Xu. Elastic, electronic, and dielectric properties of bulk and monolayer zrs2, zrse2, hfs2, hfse2 from van der waals density-functional theory. *physica status solidi (b)*, 254(9):1700033, 2017.

[136] R. Prins, V. H. J. De Beer, and G. A. Somorjai. Structure and function of the catalyst and the promoter in como hydrodesulfurization catalysts. *Catalysis Reviews*, 31(1-2):1–41, 1989.

[137] M. Salmeron, G.A. Somorjai, A. Wold, R. Chianelli, and K.S. Liang. The adsorption and binding of thiophene, butene and h2s on the basal plane of mos2 single crystals. *Chemical Physics Letters*, 90(2):105–107, 1982.

[138] Thomas F. Jaramillo, Kristina P. Jørgensen, Jacob Bonde, Jane H. Nielsen, Sebastian Horch, and Ib Chorkendorff. Identification of active edge

sites for electrochemical h2 evolution from mos2 nanocatalysts. *Science*, 317(5834):100–102, 2007.

[139] Syed M. Ahmed and H. Gerischer. Influence of crystal surface orientation on redox reactions at semiconducting mos2. *Electrochimica Acta*, 24(6):705–711, 1979.

[140] Hui Fang, Steven Chuang, Ting Chia Chang, Kuniharu Takei, Toshitake Takahashi, and Ali Javey. High-performance single layered wse2 p-fets with chemically doped contacts. *Nano Letters*, 12(7):3788–3792, 2012.

[141] Weijie Zhao, Zohreh Ghorannevis, Leiqiang Chu, Minglin Toh, Christian Kloc, Ping-Heng Tan, and Goki Eda. Evolution of electronic structure in atomically thin sheets of ws2 and wse2. *ACS Nano*, 7(1):791–797, 2013.

[142] Keng-Ku Liu, Wenjing Zhang, Yi-Hsien Lee, Yu-Chuan Lin, Mu-Tung Chang, Ching-Yuan Su, Chia-Seng Chang, Hai Li, Yumeng Shi, Hua Zhang, Chao-Sung Lai, and Lain-Jong Li. Growth of large-area and highly crystalline mos2 thin layers on insulating substrates. *Nano Letters*, 12(3):1538–1544, 2012.

[143] G. L. Frey, R. Tenne, M. J. Matthews, M. S. Dresselhaus, and G. Dresselhaus. Optical properties of ms2 (m = mo, w) inorganic fullerenelike and nanotube material optical absorption and resonance raman measurements. *Journal of Materials Research*, 13(9):24122417, 1998.

[144] A R Beal, H P Hughes, and W Y Liang. The reflectivity spectra of some group VA transition metal dichalcogenides. *Journal of Physics C: Solid State Physics*, 8(24):4236–4234, dec 1975.

[145] D.L. Greenaway and R. Nitsche. Preparation and optical properties of group

ivvi2 chalcogenides having the cdi2 structure. *Journal of Physics and Chemistry of Solids*, 26(9):1445–1458, 1965.

[146] A Sanchez-Juarez and A Ort z. Effects of precursor concentration on the optical and electrical properties of SnXSYthin films prepared by plasma-enhanced chemical vapour deposition. *Semiconductor Science and Technology*, 17(9):931–937, jul 2002.

[147] Ahmad A. Ahmad, A.B. Migdadi, Ahmad M. Alsaad, I.A. Qattan, Qais M. Al-Bataineh, and Ahmad Telfah. Computational and experimental characterizations of annealed cu2znsns4 thin films. *Heliyon*, 8(1):e08683, 2022.

[148] Sven Rhle. Tabulated values of the shockleyqueisser limit for single junction solar cells. *Solar Energy*, 130:139–147, 2016.

[149] William Shockley and Hans J. Queisser. Detailed balance limit of efficiency of pn junction solar cells. *Journal of Applied Physics*, 32(3):510–519, 1961.

[150] Pei Yang, Li-Jie Shi, Jian-Min Zhang, Gui-Bin Liu, Shengyuan A Yang, Wei Guo, and Yugui Yao. Tuning to the band gap by complex defects engineering: insights from hybrid functional calculations in CuInS2. *Journal of Physics D: Applied Physics*, 51(2):025105, dec 2017.

[151] Mohammad Mansoob Khan, Sajid A. Ansari, D. Pradhan, M. Omaish Ansari, Do Hung Han, Jintae Lee, and Moo Hwan Cho. Band gap engineered tio2 nanoparticles for visible light induced photoelectrochemical and photocatalytic studies. *J. Mater. Chem. A*, 2:637–644, 2014.

[152] Janusz Nowotny, Mohammad Abdul Alim, Tadeusz Bak, Mohammad Asri Idris, Mihail Ionescu, Kathryn Prince, Mohd Zainizan Sahdan, Kamaruzzaman Sopian, Mohd Asri Mat Teridi, and Wolfgang Sigmund. Defect chem-

istry and defect engineering of tio2-based semiconductors for solar energy conversion. *Chem. Soc. Rev.*, 44:8424–8442, 2015.

[153] Shafeer Kalathil, Mohammad Mansoob Khan, Sajid Ali Ansari, Jintae Lee, and Moo Hwan Cho. Band gap narrowing of titanium dioxide (tio2) nanocrystals by electrochemically active biofilms and their visible light activity. *Nanoscale*, 5:6323–6326, 2013.

[154] Xu Zhao, Congxia Yang, Tianxing Wang, Xu Ma, Shuyi Wei, and Congxin Xia. 3d transition metal doping-induced electronic structures and magnetism in 1t-hfse2 monolayers. *RSC Adv.*, 7:52747–52754, 2017.

[155] Reiner M. Dreizler and Cora S. Lüdde. *A Safari Through Density Functional Theory*, pages 465–478. Springer International Publishing, Heidelberg, 2013.

[156] R. Asahi, W. Mannstadt, and A. J. Freeman. Optical properties and electronic structures of semiconductors with screened-exchange lda. *Phys. Rev. B*, 59:7486–7492, Mar 1999.

[157] Jochen Heyd, Gustavo E. Scuseria, and Matthias Ernzerhof. Hybrid functionals based on a screened coulomb potential. *The Journal of Chemical Physics*, 118(18):8207–8215, 2003.

[158] Axel D. Becke. A new mixing of hartreefock and local densityfunctional theories. *The Journal of Chemical Physics*, 98(2):1372–1377, 1993.

[159] Carlo Adamo and Vincenzo Barone. Toward reliable density functional methods without adjustable parameters: The pbe0 model. *The Journal of Chemical Physics*, 110(13):6158–6170, 1999.

[160] Mauricio A. Flores, Walter Orellana, and Eduardo Menéndez-Proupin. Accuracy of the heyd-scuseria-ernzerhof hybrid functional to describe many-

electron interactions and charge localization in semiconductors. *Phys. Rev. B*, 98:155131, Oct 2018.

[161] Neil Qiang Su, Zhenyu Zhu, and Xin Xu. Doubly hybrid density functionals that correctly describe both density and energy for atoms. *Proceedings of the National Academy of Sciences*, 115(10):2287–2292, 2018.

[162] A. Seidl, A. Görling, P. Vogl, J. A. Majewski, and M. Levy. Generalized kohn-sham schemes and the band-gap problem. *Phys. Rev. B*, 53:3764–3774, Feb 1996.

[163] Peitao Liu, Cesare Franchini, Martijn Marsman, and Georg Kresse. Assessing model-dielectric-dependent hybrid functionals on the antiferromagnetic transition-metal monoxides MnO, FeO, CoO, and NiO. *Journal of Physics: Condensed Matter*, 32(1):015502, oct 2019.

[164] Jonathan H. Skone, Marco Govoni, and Giulia Galli. Nonempirical range-separated hybrid functionals for solids and molecules. *Phys. Rev. B*, 93:235106, Jun 2016.

[165] Julien Toulouse, Fran çois Colonna, and Andreas Savin. Long-range–short-range separation of the electron-electron interaction in density-functional theory. *Phys. Rev. A*, 70:062505, Dec 2004.

[166] Takeshi Yanai, David P Tew, and Nicholas C Handy. A new hybrid exchangecorrelation functional using the coulomb-attenuating method (cam-b3lyp). *Chemical Physics Letters*, 393(1):51 – 57, 2004.

[167] Roland H. Hertwig and Wolfram Koch. On the parameterization of the local correlation functional. what is becke-3-lyp? *Chemical Physics Letters*, 268(5):345 – 351, 1997.

[168] Tomomi Shimazaki and Takahito Nakajima. Theoretical study of a screened hartreefock exchange potential using position-dependent atomic dielectric constants. *The Journal of Chemical Physics*, 142(7):074109, 2015.

[169] Tomomi Shimazaki and Takahito Nakajima. Dielectric-dependent screened hartreefock exchange potential and slater-formula with coulomb-hole interaction for energy band structure calculations. *The Journal of Chemical Physics*, 141(11):114109, 2014.

[170] Tomomi Shimazaki and Yoshihiro Asai. Band structure calculations based on screened fock exchange method. *Chemical Physics Letters*, 466(1):91 – 94, 2008.

[171] F. Bechstedt, R. Del Sole, G. Cappellini, and Lucia Reining. An efficient method for calculating quasiparticle energies in semiconductors. *Solid State Communications*, 84(7):765 – 770, 1992.

[172] Tomomi Shimazaki and Yoshihiro Asai. Energy band structure calculations based on screened hartreefock exchange method: Si, alp, alas, gap, and gaas. *The Journal of Chemical Physics*, 132(22):224105, 2010.

[173] David Koller, Peter Blaha, and Fabien Tran. Hybrid functionals for solids with an optimized hartree–fock mixing parameter. *Journal of Physics: Condensed Matter*, 25(43):435503, oct 2013.

[174] Zachary D. Pozun and Graeme Henkelman. Hybrid density functional theory band structure engineering in hematite. *The Journal of Chemical Physics*, 134(22):224706, 2011.

[175] Jos C. Conesa. Modeling with hybrid density functional theory the electronic band alignment at the zinc oxideanatase interface. *The Journal of Physical Chemistry C*, 116(35):18884–18890, 2012.

[176] Audrius Alkauskas, Peter Broqvist, Fabien Devynck, and Alfredo Pasquarello. Band offsets at semiconductor-oxide interfaces from hybrid density-functional calculations. *Phys. Rev. Lett.*, 101:106802, Sep 2008.

[177] Audrius Alkauskas, Peter Broqvist, and Alfredo Pasquarello. Defect levels through hybrid density functionals: Insights and applications. *physica status solidi (b)*, 248(4):775–789, 2011.

[178] Peter Broqvist, Audrius Alkauskas, and Alfredo Pasquarello. A hybrid functional scheme for defect levels and band alignments at semiconductoroxide interfaces. *physica status solidi (a)*, 207(2):270–276, 2010.

[179] W. Kohn and L. J. Sham. Self-consistent equations including exchange and correlation effects. *Phys. Rev.*, 140:A1133–A1138, Nov 1965.

[180] G. Kresse and J. Furthmller. Efficiency of ab-initio total energy calculations for metals and semiconductors using a plane-wave basis set. *Computational Materials Science*, 6(1):15 – 50, 1996.

[181] G. Kresse and J. Furthmüller. Efficient iterative schemes for ab initio total-energy calculations using a plane-wave basis set. *Phys. Rev. B*, 54:11169–11186, Oct 1996.

[182] P. E. Blöchl. Projector augmented-wave method. *Phys. Rev. B*, 50:17953–17979, Dec 1994.

[183] G. Kresse and D. Joubert. From ultrasoft pseudopotentials to the projector augmented-wave method. *Phys. Rev. B*, 59:1758–1775, Jan 1999.

[184] Stefan Grimme. Semiempirical gga-type density functional constructed with a long-range dispersion correction. *Journal of Computational Chemistry*, 27(15):1787–1799, 2006.

[185] M. Dion, H. Rydberg, E. Schröder, D. C. Langreth, and B. I. Lundqvist. Van der waals density functional for general geometries. *Phys. Rev. Lett.*, 92:246401, Jun 2004.

[186] Hendrik J. Monkhorst and James D. Pack. Special points for brillouin-zone integrations. *Phys. Rev. B*, 13:5188–5192, Jun 1976.

[187] Carlo Adamo and Vincenzo Barone. Toward reliable density functional methods without adjustable parameters: The pbe0 model. *The Journal of Chemical Physics*, 110(13):6158–6170, 1999.

[188] Akash Laturia, Maarten L. Van de Put, and William G. Vandenberghe. Dielectric properties of hexagonal boron nitride and transition metal dichalcogenides: from monolayer to bulk. *npj 2D Materials and Applications*, 2(1):6, Mar 2018.

[189] Xu Zhao, Tianxing Wang, Shuyi Wei, Xianqi Dai, and Lin Yang. Induced magnetism in transition metal-doped 1t-zrs2. *Journal of Alloys and Compounds*, 695:2048 – 2053, 2017.

[190] Lili Sun, Wei Zhou, Yanyu Liu, Dandan Yu, Yinghua Liang, and Ping Wu. Theoretical perspective on the electronic, magnetic and optical properties of zn-doped monolayer sns2. *Applied Surface Science*, 389:484 – 490, 2016.

[191] Dan Han, Wenmei Ming, Haixuan Xu, Shiyou Chen, Deyan Sun, and Mao-Hua Du. Chemical trend of transition-metal doping in wse_2. *Phys. Rev. Applied*, 12:034038, Sep 2019.

[192] Sayantika Chowdhury, P. Venkateswaran, and Divya Somvanshi. A systematic study on the electronic structure of 3d, 4d, and 5d transition metal-doped wse2 monolayer. *Superlattices and Microstructures*, 148:106746, 2020.

[193] Anubhav Jain, Shyue Ping Ong, Geoffroy Hautier, Wei Chen, William Davidson Richards, Stephen Dacek, Shreyas Cholia, Dan Gunter, David Skinner, Gerbrand Ceder, and Kristin A. Persson. Commentary: The materials project: A materials genome approach to accelerating materials innovation. *APL Materials*, 1(1):011002, 2013.

[194] G. Domingo, R. S. Itoga, and C. R. Kannewurf. Fundamental optical absorption in sns_2 and $snse_2$. *Phys. Rev.*, 143:536–541, Mar 1966.

[195] Yu Kumagai, Lee A. Burton, Aron Walsh, and Fumiyasu Oba. Electronic structure and defect physics of tin sulfides: Sns, sn_2s_3, and Sns_2. *Phys. Rev. Applied*, 6:014009, Jul 2016.

[196] C. Bacaksiz, S. Cahangirov, A. Rubio, R. T. Senger, F. M. Peeters, and H. Sahin. Bilayer sns_2: Tunable stacking sequence by charging and loading pressure. *Phys. Rev. B*, 93:125403, Mar 2016.

[197] M.L. Toh, K.J. Tan, F.X. Wei, K.K. Zhang, H. Jiang, and C. Kloc. Intercalation of organic molecules into sns2 single crystals. *Journal of Solid State Chemistry*, 198:224 – 230, 2013.

[198] J. E. Padilha, H. Peelaers, A. Janotti, and C. G. Van de Walle. Nature and evolution of the band-edge states in mos_2: From monolayer to bulk. *Phys. Rev. B*, 90:205420, Nov 2014.

[199] C D Lokhande. A chemical method for tin disulphide thin film deposition. *Journal of Physics D: Applied Physics*, 23(12):1703–1705, Dec 1990.

[200] Yongfu Sun, Hao Cheng, Shan Gao, Zhihu Sun, Qinghua Liu, Qin Liu, Fengcai Lei, Tao Yao, Jingfu He, Shiqiang Wei, and Yi Xie. Freestanding tin disulfide single-layers realizing efficient visible-light water splitting. *Angewandte Chemie International Edition*, 51(35):8727–8731, 2012.

[201] C. H. Chen, W. Fabian, F. C. Brown, K. C. Woo, B. Davies, B. DeLong, and A. H. Thompson. Angle-resolved photoemission studies of the band structure of $tise_2$ and tis_2. *Phys. Rev. B*, 21:615–624, Jan 1980.

[202] D. R. Allan, A. A. Kelsey, S. J. Clark, R. J. Angel, and G. J. Ackland. High-pressure semiconductor-semimetal transition in tis_2. *Phys. Rev. B*, 57:5106–5110, Mar 1998.

[203] P C Klipstein and R H Friend. Semiconductor to semimetal transition in TiS2at 40 kbar. *Journal of Physics C: Solid State Physics*, 17(15):2713–2734, may 1984.

[204] J J Barry, H P Hughes, P C Klipstein, and R H Friend. Stoichiometry effects in angle -resolved photoemission and transport studies of tis2. *Journal of Physics C: Solid State Physics*, 16(2):393–402, jan 1983.

[205] F R Shepherd and P M Williams. Photoemission studies of the band structures of transition metal dichalcogenides. i. groups IVA and IVB. *Journal of Physics C: Solid State Physics*, 7(23):4416–4426, dec 1974.

[206] G A Benesh, A M Woolley, and C Umrigar. The pressure dependences of TiS2and TiSe2band structures. *Journal of Physics C: Solid State Physics*, 18(8):1595–1603, mar 1985.

[207] C. M. Fang, R. A. de Groot, and C. Haas. Bulk and surface electronic structure of $1t - tis_2$ and $1t - tise_2$. *Phys. Rev. B*, 56:4455–4463, Aug 1997.

[208] Z. Y. Wu, G. Ouvrard, S. Lemaux, P. Moreau, P. Gressier, F. Lemoigno, and J. Rouxel. Sulfur k-edge x-ray-absorption study of the charge transfer upon lithium intercalation into titanium disulfide. *Phys. Rev. Lett.*, 77:2101–2104, Sep 1996.

[209] Z. Y. Wu, F. Lemoigno, P. Gressier, G. Ouvrard, P. Moreau, J. Rouxel, and C. R. Natoli. Experimental and theoretical studies of the electronic structure of tis_2. *Phys. Rev. B*, 54:R11009–R11013, Oct 1996.

[210] Z. Y. Wu, G. Ouvrard, P. Moreau, and C. R. Natoli. Interpretation of preedge features in the ti and s k-edge x-ray-absorption near-edge spectrain the layered disulfides tis_2 and tas_2. *Phys. Rev. B*, 55:9508–9513, Apr 1997.

[211] Sangeeta Sharma, Tashi Nautiyal, G. S. Singh, S. Auluck, P. Blaha, and Claudia Ambrosch-Draxl. Electronic structure of $1t - tis_2$. *Phys. Rev. B*, 59:14833–14836, Jun 1999.

[212] Ali Hussain Reshak and S. Auluck. Electronic and optical properties of the $1t$ phases of tis_2, $tise_2$, and $tite_2$. *Phys. Rev. B*, 68:245113, Dec 2003.

[213] Edward E. Abbott, Joseph W. Kolis, Nathan D. Lowhorn, William Sams, and Terry M. Tritt. Thermoelectric properties of tis2 type materials. *MRS Online Proceedings Library*, 793(1):322–331, Dec 2003.

[214] Carl A. Kukkonen, W. J. Kaiser, E. M. Logothetis, B. J. Blumenstock, P. A. Schroeder, S. P. Faile, R. Colella, and J. Gambold. Transport and optical properties of $ti_{1+x}s_2$. *Phys. Rev. B*, 24:1691–1709, Aug 1981.

[215] Shigemasa Suga, Christian Tusche, Yu ichiro Matsushita, Martin Ellguth, Akinori Irizawa, and Jrgen Kirschner. Momentum microscopy of the layered semiconductor TiS2and ni intercalated ni1/3tis2. *New Journal of Physics*, 17(8):083010, aug 2015.

[216] Keyan Hu, Dong Wang, Wei Zhao, Yuhao Gu, Kejun Bu, Jie Pan, Peng Qin, Xian Zhang, and Fuqiang Huang. Intermediate band material of titanium-doped tin disulfide for wide spectrum solar absorption. *Inorganic Chemistry*, 57(7):3956–3962, 2018.

[217] Kang Min Kim, Byeong Sub Kwak, Sora Kang, and Misook Kang. Synthesis of submicron hexagonal plate-type sns¡sub¿2¡/sub¿ and band gap-tuned sn¡sub¿1¡i¿x¡/i¿¡/sub¿ti¡sub¿¡i¿x¡/i¿¡/sub¿s¡sub¿2¡/sub¿ materials and their hydrogen production abilities on methanol/water photosplitting. *International Journal of Photoenergy*, 2014:479508, Jul 2014.

[218] Congxin Xia, Jiao An, Tianxing Wang, Shuyi Wei, and Yu Jia. Sn1xtixs2 ternary alloys: A new visible optical material. *Acta Materialia*, 72:223–228, 2014.

[219] Perla Wahnn, Jos C. Conesa, Pablo Palacios, Raquel Lucena, Irene Aguilera, Yohanna Seminovski, and Fernando Fresno. V-doped sns2: a new intermediate band material for a better use of the solar spectrum. *Phys. Chem. Chem. Phys.*, 13:20401–20407, 2011.

[220] O.A. Yassin, A.A. Abdelaziz, and A.Y. Jaber. Structural and optical characterization of v- and w-doped sns2 thin films prepared by spray pyrolysis. *Materials Science in Semiconductor Processing*, 38:81–86, 2015.

[221] Long Lin, Yujin Chen, Hualong Tao, Linwei Yao, Jingtao Huang, Linghao Zhu, Mengsi Lou, Ruixin Chen, Longbin Yan, and Zhanying Zhang. Ferromagnetism and optical properties of sns2 doped with two impurities: first-principles calculations. *Phys. Chem. Chem. Phys.*, 23:6574–6582, 2021.

[222] Mina Taleblou, Ehsan Borhani, Benyamin Yarmand, and Ali Reza Kolahi. Modification of the structural and optical properties of fe-doped SnS2 thin film. *Materials Research Express*, 6(2):025908, nov 2018.

[223] Lili Sun, Wei Zhou, Yanyu Liu, Dandan Yu, Yinghua Liang, and Ping Wu. Electronic structure and optical properties of fe-doped sns2 from first-principle calculations. *RSC Adv.*, 6:3480–3486, 2016.

[224] Lili Sun, Wei Zhou, Yinghua Liang, Li Liu, and Ping Wu. Magnetic properties in fe-doped sns2: Density functional calculations. *Computational Materials Science*, 117:489–495, 2016.

[225] Areej S. Alqarni, B.O. Alsobhi, A.A. Elabbar, and O.A. Yassin. Impedance and dielectric analysis of polycrystalline undoped and fe doped sns2. *Materials Science in Semiconductor Processing*, 59:18–22, 2017.

[226] Meiwen Jiang, Yue Huang, Wei Sun, and Xiaojun Zhang. Co-doped sns2 nanosheet array for efficient oxygen evolution reaction electrocatalyst. *Journal of Materials Science*, 54(21):13715–13723, Nov 2019.

[227] G. Kiruthigaa, C. Manoharan, C. Raju, S. Dhanapandian, and V. Thanikachalam. Synthesis and spectroscopic analysis of undoped and zn doped sns2 nanostructure by solid state reaction method. *Materials Science in Semiconductor Processing*, 26:533–539, 2014.

[228] Hamid Ullah, Mohammad Noor-A-Alam, and Young-Han Shin. Vacancy- and doping-dependent electronic and magnetic properties of monolayer sns2. *Journal of the American Ceramic Society*, 103(1):391–402, 2020.

[229] Wenhua Zhao, Zhiqiang Wei, Li Zhang, Xiaojuan Wu, and Xuan Wang. Cr doped sns2 nanoflowers: Preparation, characterization and photocatalytic decolorization. *Materials Science in Semiconductor Processing*, 88:173–180, 2018.

[230] Houcine Bouzid, Ramchandra Sahoo, Seok Joon Yun, Kirandeep Singh, Youngjo Jin, Jinbao Jiang, Duhee Yoon, Hyun Yong Song, Giheon Kim, Wooseon Choi, Young-Min Kim, and Young Hee Lee. Multiple magnetic phases in van der waals mn-doped sns2 semiconductor. *Advanced Functional Materials*, 31(29):2102560, 2021.

[231] Bo Li, Tao Xing, Mianzeng Zhong, Le Huang, Na Lei, Jun Zhang, Jingbo Li, and Zhongming Wei. A two-dimensional fe-doped sns2 magnetic semiconductor. *Nature Communications*, 8(1):1958, Dec 2017.

[232] Xu Ma, Xu Zhao, and Tianxing Wang. Effect of strain on the electronic and magnetic properties of an fe-doped wse2 monolayer. *RSC Adv.*, 6:69758–69763, 2016.

[233] Anwar Ali, Jian-Min Zhang, Iltaf Muhammad, Ismail Shahid, Iftikhar Ahmad, Majeed Ur Rehman, Iqtidar Ahmad, and Fazal Kabir. First-principles investigation on electronic structure, magnetic states and optical properties of mn-doped sns2 monolayer via strain engineering. *Physica E: Low-dimensional Systems and Nanostructures*, 134:114842, 2021.

[234] Yongji Gong, Hongtao Yuan, Chun-Lan Wu, Peizhe Tang, Shi-Ze Yang, Ankun Yang, Guodong Li, Bofei Liu, Jorik van de Groep, Mark L. Brongersma, Matthew F. Chisholm, Shou-Cheng Zhang, Wu Zhou, and Yi Cui. Spatially controlled doping of two-dimensional sns2 through intercalation for electronics. *Nature Nanotechnology*, 13(4):294–299, Apr 2018.

[235] G. Mohan Kumar, Fu Xiao, P. Ilanchezhiyan, Sh. Yuldashev, A. Madhan Kumar, H.D. Cho, D.J. Lee, and T.W. Kang. High performance photodiodes based on chemically processed cu doped sns2 nanoflakes. *Applied Surface Science*, 455:446–454, 2018.

[236] Ganesan Mohan Kumar, Pugazhendi Ilanchezhiyan, Hak Dong Cho, Shavkat Yuldashev, Hee Chang Jeon, Deuk Young Kim, and Tae Won Kang. Effective modulation of optical and photoelectrical properties of sns2 hexagonal nanoflakes via zn incorporation. *Nanomaterials*, 9(7), 2019.

[237] C M I Okoye. Theoretical study of the electronic structure, chemical bonding

and optical properties of KNbO3in the paraelectric cubic phase. *Journal of Physics: Condensed Matter*, 15(35):5945–5958, aug 2003.

[238] Luyan Li, Qiaoya Lv, Yafang Li, Longlong Li, Yanjie Zhao, Jinhua Mao, Dawei Shao, Ruishan Tan, Shuhua Shi, and Ting Chen. The photocatalytic properties of vzn–n co-doped zno: A first-principles investigation. *Catalysis Letters*, 150(10):2792–2797, Oct 2020.

[239] Sonali Saha, T. P. Sinha, and Abhijit Mookerjee. Electronic structure, chemical bonding, and optical properties of paraelectric batio$_3$. *Phys. Rev. B*, 62:8828–8834, Oct 2000.

[240] Xian Zhang, Wenchuang Wang, Qingfeng Zeng, and Hui Li. First-principles study of the dielectric properties and infrared reflectance spectrum of y2o3. *Solid State Communications*, 150(7):360–363, 2010.

[241] Pierluigi Cudazzo, Ilya V. Tokatly, and Angel Rubio. Dielectric screening in two-dimensional insulators: Implications for excitonic and impurity states in graphane. *Phys. Rev. B*, 84:085406, Aug 2011.

[242] L. V. Keldysh. Coulomb interaction in thin semiconductor and semimetal films. *JETP Lett.*, 29:658, 1979.

[243] Elsa Prada, J. V. Alvarez, K. L. Narasimha-Acharya, F. J. Bailen, and J. J. Palacios. Effective-mass theory for the anisotropic exciton in two-dimensional crystals: Application to phosphorene. *Phys. Rev. B*, 91:245421, Jun 2015.

[244] Arno Schindlmayr. Excitons with anisotropic effective mass. *European Journal of Physics*, 18(5):374–376, sep 1997.

[245] Srilatha Arra, Rohit Babar, and Mukul Kabir. Exciton in phosphorene: Strain, impurity, thickness, and heterostructure. *Phys. Rev. B*, 99:045432, Jan 2019.

[246] Inc. Wolfram Research. Mathematica 10.2, 2015.

[247] Vei Wang, Nan Xu, Jin-Cheng Liu, Gang Tang, and Wen-Tong Geng. Vaspkit: A user-friendly interface facilitating high-throughput computing and analysis using vasp code. *Computer Physics Communications*, 267:108033, 2021.

[248] Kirill A. Velizhanin and Avadh Saxena. Excitonic effects in two-dimensional semiconductors: Path integral monte carlo approach. *Phys. Rev. B*, 92:195305, Nov 2015.

[249] Jian Zhen Ou, Wanyin Ge, Benjamin Carey, Torben Daeneke, Asaf Rotbart, Wei Shan, Yichao Wang, Zhengqian Fu, Adam F. Chrimes, Wojtek Wlodarski, Salvy P. Russo, Yong Xiang Li, and Kourosh Kalantar-zadeh. Physisorption-based charge transfer in two-dimensional sns2 for selective and reversible no2 gas sensing. *ACS Nano*, 9(10):10313–10323, 2015.

[250] Bhagyashri Devaru Bhat. Tuning the magnetic and electronic properties of monolayer sns2 by 3d transition metal doping: A dft study. *Materials Today Communications*, 33:104626, 2022.

[251] Arunima K. Singh and Richard G. Hennig. Computational prediction of two-dimensional group-iv mono-chalcogenides. *Applied Physics Letters*, 105(4):042103, 2014.

[252] Oleg V. Yazyev and Lothar Helm. Defect-induced magnetism in graphene. *Phys. Rev. B*, 75:125408, Mar 2007.

[253] A. M. Valencia and M. J. Caldas. Single vacancy defect in graphene: Insights into its magnetic properties from theoretical modeling. *Phys. Rev. B*, 96:125431, Sep 2017.

[254] eljko ljivananin, Richard Balog, and Liv Hornekr. Magnetism in graphene induced by hydrogen adsorbates. *Chemical Physics Letters*, 541:70–74, 2012.

[255] Pankaj Kumar, Vinit Sharma, Fernando A. Reboredo, Li-Ming Yang, and Raghani Pushpa. Tunable magnetism in metal adsorbed fluorinated nanoporous graphene. *Scientific Reports*, 6(1):31841, Aug 2016.

[256] H. Sahin, M. Topsakal, and S. Ciraci. Structures of fluorinated graphene and their signatures. *Phys. Rev. B*, 83:115432, Mar 2011.

[257] Bao Zhu Wang, Sheng Tang, Tong Wei, Jie Ren, and Min Wang. First-principles study of 3d transition metal doped single-layer graphene. In *Seminar on Advances in Materials Science and Engineering*, volume 984 of *Materials Science Forum*, pages 82–87. Trans Tech Publications Ltd, 5 2020.

[258] Wei Hu and Jinlong Yang. Defects in phosphorene. *The Journal of Physical Chemistry C*, 119(35):20474–20480, 2015.

[259] Arqum Hashmi and Jisang Hong. Transition metal doped phosphorene: First-principles study. *The Journal of Physical Chemistry C*, 119(17):9198–9204, 2015.

[260] Aleksander A. Tedstone, David J. Lewis, and Paul OBrien. Synthesis, properties, and applications of transition metal-doped layered transition metal dichalcogenides. *Chemistry of Materials*, 28(7):1965–1974, 2016.

[261] Yi Tian, Zhipeng Zhu, Zhizhong Ge, An Sun, Quan Zhang, Songlei Huang, Hongping Li, and Jian Meng. Electronic and magnetic properties of 3d transition metal doped mose2 monolayer. *Physica E: Low-dimensional Systems and Nanostructures*, 116:113745, 2020.

[262] Ling-Yun Xie and Jian-Min Zhang. Electronic structures and magnetic properties of the transition-metal atoms (mn, fe, co and ni) doped ws2: A first-principles study. *Superlattices and Microstructures*, 98:148–157, 2016.

[263] Carmen J Gil, Anh Pham, Aibing Yu, and Sean Li. An ab initio study of transition metals doped with wse2 for long-range room temperature ferromagnetism in two-dimensional transition metal dichalcogenide. *Journal of Physics: Condensed Matter*, 26(30):306004, jul 2014.

[264] Xuming Wu, Jiangchao Han, Yulin Feng, Guanpeng Li, Cong Wang, Guangqian Ding, and Guoying Gao. Half-metals and half-semiconductors in a transition metal doped snse2 monolayer: a first-principles study. *RSC Adv.*, 7:44499–44504, 2017.

[265] Xu Zhao, Tianxing Wang, Congxin Xia, Xianqi Dai, Shuyi Wei, and Lin Yang. Magnetic doping in two-dimensional transition-metal dichalcogenide zirconium diselenide. *Journal of Alloys and Compounds*, 698:611–616, 2017.

[266] Jochen Heyd, Juan E. Peralta, Gustavo E. Scuseria, and Richard L. Martin. Energy band gaps and lattice parameters evaluated with the heyd-scuseria-ernzerhof screened hybrid functional. *The Journal of Chemical Physics*, 123(17):174101, 2005.

[267] Thomas M. Henderson, Benjamin G. Janesko, and Gustavo E. Scuseria. Generalized gradient approximation model exchange holes for range-separated hybrids. *The Journal of Chemical Physics*, 128(19):194105, 2008.

[268] Charles Sun and Xuan Luo. Tuning the magnetic and electronic properties of monolayer vi3 by 3d transition metal doping: A first-principles study. *Applied Surface Science*, 571:151208, 2022.

[269] S. A. Shevlin and Z. X. Guo. Transition-metal-doping-enhanced hydrogen storage in boron nitride systems. *Applied Physics Letters*, 89(15):153104, 2006.

[270] Arqum Hashmi and Jisang Hong. Transition metal doped phosphorene: First-principles study. *The Journal of Physical Chemistry C*, 119(17):9198–9204, 2015.

[271] Rohit Babar and Mukul Kabir. Transition metal and vacancy defect complexes in phosphorene: A spintronic perspective. *The Journal of Physical Chemistry C*, 120(27):14991–15000, 2016.

[272] A. V. Krasheninnikov, P. O. Lehtinen, A. S. Foster, P. Pyykkö, and R. M. Nieminen. Embedding transition-metal atoms in graphene: Structure, bonding, and magnetism. *Phys. Rev. Lett.*, 102:126807, Mar 2009.

[273] Daniel I. Khomskii. *Transition Metal Compounds*. Cambridge University Press, 2014.

[274] Di Xiao, Gui-Bin Liu, Wanxiang Feng, Xiaodong Xu, and Wang Yao. Coupled spin and valley physics in monolayers of mos_2 and other group-vi dichalcogenides. *Phys. Rev. Lett.*, 108:196802, May 2012.

[275] Z. Y. Zhu, Y. C. Cheng, and U. Schwingenschlögl. Giant spin-orbit-induced spin splitting in two-dimensional transition-metal dichalcogenide semiconductors. *Phys. Rev. B*, 84:153402, Oct 2011.

[276] Ang-Yu Lu, Hanyu Zhu, Jun Xiao, Chih-Piao Chuu, Yimo Han, Ming-Hui Chiu, Chia-Chin Cheng, Chih-Wen Yang, Kung-Hwa Wei, Yiming Yang, Yuan Wang, Dimosthenis Sokaras, Dennis Nordlund, Peidong Yang, David A. Muller, Mei-Yin Chou, Xiang Zhang, and Lain-Jong Li. Janus monolayers of transition metal dichalcogenides. *Nature Nanotechnology*, 12(8):744–749, Aug 2017.

[277] Shubham Patel, Urmimala Dey, Narayan Prasad Adhikari, and A. Taraphder. Electric field and strain-induced band-gap engineering and manipulation of the rashba spin splitting in janus van der waals heterostructures. *Phys. Rev. B*, 106:035125, Jul 2022.

[278] Wenwu Shi and Zhiguo Wang. Mechanical and electronic properties of janus monolayer transition metal dichalcogenides. *Journal of Physics: Condensed Matter*, 30(21):215301, May 2018.

[279] Anders C. Riis-Jensen, Thorsten Deilmann, Thomas Olsen, and Kristian S. Thygesen. Classifying the electronic and optical properties of janus monolayers. *ACS Nano*, 13(11):13354–13364, 2019. PMID: 31613091.

[280] Jiaren Yuan, Yumeng Yang, Yongqing Cai, Yihong Wu, Yuanping Chen, Xiaohong Yan, and Lei Shen. Intrinsic skyrmions in monolayer janus magnets. *Phys. Rev. B*, 101:094420, Mar 2020.

[281] Z. Kahraman, A. Kandemir, M. Yagmurcukardes, and H. Sahin. Single-layer janus-type platinum dichalcogenides and their heterostructures. *The Journal of Physical Chemistry C*, 123(7):4549–4557, 2019.

[282] Wen-Zhi Xiao, Liang Xu, Gang Xiao, Ling-Ling Wang, and Xiong-Ying Dai. Two-dimensional hexagonal chromium chalco-halides with large vertical piezoelectricity, high-temperature ferromagnetism, and high magnetic anisotropy. *Phys. Chem. Chem. Phys.*, 22:14503–14513, 2020.

[283] Yi-Feng Zhao, Yu-Hao Shen, He Hu, Wen-Yi Tong, and Chun-Gang Duan. Combined piezoelectricity and ferrovalley properties in janus monolayer vclbr. *Phys. Rev. B*, 103:115124, Mar 2021.

[284] Vuong Van Thanh, Nguyen Thuy Dung, Le Xuan Bach, Do Van Truong, and Nguyen Tuan Hung. Turning electronic and optical properties of mono-

layer janus sn-dichalcogenides by biaxial strain. In Nguyen Tien Khiem, Tran Van Lien, and Nguyen Xuan Hung, editors, *Modern Mechanics and Applications*, pages 981–989, Singapore, 2022. Springer Singapore.

[285] Hong T. T. Nguyen, Vu V. Tuan, Chuong V. Nguyen, Huynh V. Phuc, Hien D. Tong, Son-Tung Nguyen, and Nguyen N. Hieu. Electronic and optical properties of a janus snsse monolayer: effects of strain and electric field. *Phys. Chem. Chem. Phys.*, 22:11637–11643, 2020.

[286] San-Dong Guo, Xiao-Shu Guo, Ru-Yue Han, and Ye Deng. Predicted janus snsse monolayer: a comprehensive first-principles study. *Phys. Chem. Chem. Phys.*, 21:24620–24628, 2019.

[287] Xiaoli Zhang, Yu Cui, Liping Sun, Mengyuan Li, Jinyan Du, and Yucheng Huang. Stabilities, and electronic and piezoelectric properties of two-dimensional tin dichalcogenide derived janus monolayers. *J. Mater. Chem. C*, 7:13203–13210, 2019.

[288] Marwan Alam, Hafiza Sumaira Waheed, Hamid Ullah, M. Waqas Iqbal, Young-Han Shin, Muhammad Junaid Iqbal Khan, H.I. Elsaeedy, and R. Neffati. Optoelectronics properties of janus snsse monolayer for solar cells applications. *Physica B: Condensed Matter*, 625:413487, 2022.

[289] Yee H. Robin Chang, Tiem L. Yoon, Keat H. Yeoh, and Thong L. Lim. Integrated snsse bulk and monolayer as industrial waste heat thermoelectric materials. *International Journal of Energy Research*, 45(2):2085–2099, 2020.

[290] Yufeng Luo, Shihao Han, Rui Hu, Hongmei Yuan, Wenyan Jiao, and Huijun Liu. The thermal stability of janus monolayers SnXY (x, Y = o, s, se): Ab-initio molecular dynamics and beyond. *Nanomaterials (Basel)*, 12(1):101, December 2021.

[291] Bhagyashri Devaru Bhat. Dielectric-dependent hybrid functional calculations on the electronic band gap of 3*d* transition metal doped sns_2 and their optical properties. *Phys. Rev. B*, 105:195205, May 2022.

[292] Abeera Rahman, Hye Jung Kim, Mohammad Noor-A-Alam, and Young-Han Shin. A theoretical study on tuning band gaps of monolayer and bilayer sns2 and snse2 under external stimuli. *Current Applied Physics*, 19(6):709–714, 2019.

[293] Yi Wang, Zhibin Gao, and Jun Zhou. Ultralow lattice thermal conductivity and electronic properties of monolayer 1t phase semimetal site2 and snte2. *Physica E: Low-dimensional Systems and Nanostructures*, 108:53–59, 2019.

[294] Abhishek Patel, Deobrat Singh, Yogesh Sonvane, P. B. Thakor, and Rajeev Ahuja. High thermoelectric performance in two-dimensional janus monolayer material ws-x (x = se and te). *ACS Applied Materials & Interfaces*, 12(41):46212–46219, 2020.

[295] Lin Ju, Mei Bie, Xiao Tang, Jing Shang, and Liangzhi Kou. Janus wsse monolayer: An excellent photocatalyst for overall water splitting. *ACS Applied Materials & Interfaces*, 12(26):29335–29343, 2020.

[296] Congxin Xia, Wenqi Xiong, Juan Du, Tianxing Wang, Yuting Peng, and Jingbo Li. Universality of electronic characteristics and photocatalyst applications in the two-dimensional janus transition metal dichalcogenides. *Phys. Rev. B*, 98:165424, Oct 2018.

[297] Moh. Adhib Ulil Absor, Hiroki Kotaka, Fumiyuki Ishii, and Mineo Saito. Tunable spin splitting and spin lifetime in polar WSTe monolayer. *Japanese Journal of Applied Physics*, 57(4S):04FP01, feb 2018.

[298] Stefan Grimme. Semiempirical gga-type density functional constructed with a long-range dispersion correction. *Journal of Computational Chemistry*, 27(15):1787–1799, 2006.

[299] Supriyo Datta and Biswajit Das. Electronic analog of the electrooptic modulator. *Applied Physics Letters*, 56(7):665–667, 1990.

[300] Youn Ho Park, Jun Woo Choi, Hyung-jun Kim, Joonyeon Chang, Suk Hee Han, Heon-Jin Choi, and Hyun Cheol Koo. Complementary spin transistor using a quantum well channel. *Scientific Reports*, 7(1):46671, Apr 2017.

[301] Ya Feng, Qi Jiang, Baojie Feng, Meng Yang, Tao Xu, Wenjing Liu, Xiufu Yang, Masashi Arita, Eike F. Schwier, Kenya Shimada, Harald O. Jeschke, Ronny Thomale, Youguo Shi, Xianxin Wu, Shaozhu Xiao, Shan Qiao, and Shaolong He. Rashba-like spin splitting along three momentum directions in trigonal layered ptbi2. *Nature Communications*, 10(1):4765, Oct 2019.

[302] Imran Khan, Brahim Marfoua, and Jisang Hong. Electric field induced giant valley polarization in two dimensional ferromagnetic wse2/crsnse3 heterostructure. *npj 2D Materials and Applications*, 5(1):10, Jan 2021.

[303] Haijun Zhang, Lu Liu, and Zhen Zhou. First-principles studies on facet-dependent photocatalytic properties of bismuth oxyhalides (bioxs). *RSC Adv.*, 2:9224–9229, 2012.

[304] Arunima Singh, Manjari Jain, and Saswata Bhattacharya. Mos2 and janus (mosse) based 2d van der waals heterostructures: emerging direct z-scheme photocatalysts. *Nanoscale Adv.*, 3:2837–2845, 2021.

[305] Fan Zheng, Liang Z. Tan, Shi Liu, and Andrew M. Rappe. Rashba spinorbit coupling enhanced carrier lifetime in ch3nh3pbi3. *Nano Letters*, 15(12):7794–7800, 2015.

[306] Di Xiao, Gui-Bin Liu, Wanxiang Feng, Xiaodong Xu, and Wang Yao. Coupled spin and valley physics in monolayers of mos_2 and other group-vi dichalcogenides. *Phys. Rev. Lett.*, 108:196802, May 2012.

[307] Amirhossein Rezavand and Nayereh Ghobadi. Tuning the rashba spin splitting in janus mosete and wsete van der waals heterostructures by vertical strain. *Journal of Magnetism and Magnetic Materials*, 544:168721, 2022.

LIST OF PUBLICATIONS

1. *Dielectric-dependent hybrid functional calculations on the electronic bandgap of 3d transition metal-doped SnS_2 and their optical properties*

   Bhagyashri Devaru Bhat

   Physical Review B 105, 195205 (2022)

2. *Tuning the magnetic and electronic properties of monolayer SnS_2 by 3d transition metal doping: A DFT study*

   Bhagyashri Devaru Bhat

   Materials Today Communications 33, 104626 (2022)

3. *Rashba spin-splitiing in SnXY/WXY (X, Y = S, Se, Te with $X \neq Y$) heterostructures*

   Bhagyashri Devaru Bhat

   Manuscript under preparation